DISSERTATION

Modeling Spintronic Effects
in Silicon

ausgeführt zum Zwecke der Erlangung des akademischen
Grades
eines Doktors der technischen Wissenschaften

eingereicht an der Technischen Universität Wien
Fakultät für Elektrotechnik und Informationstechnik
von

Dmitry Osintsev

Wien, im 28 Mai 2014 _____

Kurzfassung

Der Elektronenspin als Freiheitsgrad zieht die Aufmerksamkeit vieler Forscher auf sich, da der Elektronenspin zwei unterscheidbare Zustände in Form der Spinrichtungen entlang einer gewählten Achse bereitstellt, die in guter Analogie zu den beiden Zuständen eines digitalen Bits stehen. Obwohl Überlegungen zu spinbasierten Logikschaltkreisen bis in die 1960er zurückreichen, sind diese erst vor Kurzem realisiert worden, als elektrische und optische Manipulationen des Spins ohne der Notwendigkeit eines magnetischen Feldes eingeführt worden sind. Heute ist spinbasierte Elektronik ("Spintronik") ein sich rasch entwickelndes Forschungs- und Entwicklungsfeld, welches neue Bauteile ermöglicht, deren Charakteristiken nicht nur vergleichbar, sondern sogar jenen aktueller ladungsbasierter Bauteile überlegen sind.

Um spinbasierte Bauteile herstellen zu können, müssen die Transporteigenschaften des Spins in Halbleitern genau untersucht werden. Da Silizium das weitverbreitetste Material in der modernen Mikroelektronik darstellt, sind insbesondere Spinrelaxierungdetails in Siliziumkanälen von höchstem Interesse. Außerdem wird häufig mechanische Spannung zur Steigerung der Ladungsträgerbeweglichkeit in modernen MOSFETs verwendet. In der vorliegenden Doktorarbeit wird die $\mathbf{k \cdot p}$ -Methode zur Untersuchung der Subbandstruktur und der Wellenfunktionen in den eingeschränkten Elektronensystemen von Siliziumschichten unter Berücksichtigung von Scherdehnung und der Kopplung von Spinorbitalen verwendet. Analytische Ausdrücke für den vierbandigen $\mathbf{k \cdot p}$ -Hamilton-Operator werden für den Fall eines quadratischen Potentialtopfs abgeleitet. Aus den Wellenfunktionen werden die zugehörigen Matrixelemente zur Beschreibung der Spinrelaxation berechnet. Eine Analyse der Spinlebensdauer zeigt sowohl Beiträge der Oberflächenrauheit, als auch von Elektron-Phonon-Interaktionen herbeigeführte Spinrelaxiation. Da die Entartung der ungestrichenen Subbänder durch Scherdehnung aufgehoben wird, wodurch die elastischen Zwischentalstreuungen als Hauptbeitrag zur Spinrelaxation unterdrückt werden, wird eine Erhöhung der Spinlebenszeit um eine Größenordnung in verspannten Siliziumschichten vorhergesagt.

Die Verwendung von Silizium in spinbasierten Feldeffekttransistoren ("SpinFETs") ist von großem Interesse, da es die Herstellung von spinbasierten Bauteilen mittels bereits hochentwickelter Prozessierungschritte für Silizium verspricht. Durch den durch die Grenzfläche verursachten Bruch der Symmetrie der Inversion wird die vom elektrischen Feld abhängige Spin-Orbit-Interaktion in Schichten und Finnen aus Silizium verstärkt. Es wird gezeigt, dass im Falle geeignet ausgelegter Schottkybarrieren eine verstärkte Modulation des Kanalmagnetwiderstands zwischen Source bzw. Drain und

dem Kanal auch bei Raumtemperatur bestehen bleibt. Um die Kanallänge reduzieren zu können, muss die Transportmasse entlang des Kanals groß sein. Basierend auf dem zweibandigen $\mathbf{k \cdot p}$ -Modell wird eine stärkere Abhängigkeit des Wertes für die effektive Spin-Orbit-Interaktion in siliziumbasierten SpinFETs mit in [100]-Richtung orientieren Finnen vorhergesagt, womit diese für eine praktische Realisierung bevorzugt werden sollten.

Abstract

The spin degree of freedom attracts the attention of many researchers, because the electron spin offers two distinguishable states with spin up and down along a chosen axis in a good analogy to the two states of a digital bit. Although the idea of spin-based logic was already formulated in the 60ies of the last century, however, it has not been realized until recently, when electrical and optical spin manipulation without any need of a magnetic field was introduced. Nowadays, spin electronics - spintronics - is a rapidly developing research and development area which offers novel devices with characteristics not only comparable but even superior to those of the state-of-the-art charge-based devices.

In order to build a spin-based device the spin transport properties in semiconducting materials must be closely examined. Because silicon is the most widely used material of modern microelectronics, the details of spin relaxation in silicon channels are of paramount interest. Also, strain is routinely used to achieve a charge carrier mobility enhancement in modern MOSFETs. In this thesis the $\mathbf{k \cdot p}$ method is used to examine the subband structure and the wave functions in confined electron systems of silicon films in the presence of shear strain and spin-orbit coupling. Analytical expressions for the four-band $\mathbf{k \cdot p}$ Hamiltonian are found in case of a square well potential. The wave functions are used to evaluate the corresponding spin relaxation matrix elements. The analysis of the spin lifetime comprises contributions from surface roughness and electron-phonon mediated spin relaxation. Because the unprimed subband degeneracy is lifted by shear strain, thus suppressing the most important elastic intervalley contribution to spin relaxation, the spin lifetime enhancement by an order of magnitude in strained silicon films is predicted.

Utilizing silicon in spin-based field-effect transistors (SpinFETs) is of a great interest, since it promises to build spin devices using the well developed silicon processing. Due to the interface induced inversion symmetry breaking the strength of the electric field dependent spin-orbit interaction is enhanced in thin silicon films and fins. It is shown that in case of properly designed Schottky barriers between the source/drain and the channel a pronounced modulation of the channel magnetoresistance persists at room temperature. In order to reduce the channel length, the transport mass along the channel must be large. Based on the two-band $\mathbf{k \cdot p}$ model for the conduction band, a stronger dependence on the value of the effective spin-orbit interaction in silicon SpinFETs with a [100]-oriented silicon fins is predicted, making them preferable for practical realization.

iv

Аннотация

Спиновые степени свободы привлекают внимание многих исследователей по причине того, что ориентация спина электрона вдоль выбранной оси может иметь два хорошо определённых состояния - спин вверх и спин вниз, что является хорошим аналогом бита информации. Хотя идея создания спиновой логики была сформулирована ещё в шестидесятые годы прошлого столетия, до последнего времени она не была реализована на практике, пока не была показана возможность управлять спином посредством электрического тока или света, без магнитного поля.

В настоящее время спиновая электроника - спинтроника - быстроразвивающаяся область исследований и разработок, которая предлагает компоненты не только сравнимые, но зачастую и превосходящие по своим характеристикам самые современные компоненты, построенные на основе использования электронного заряда.

Для того, чтобы создать компонент, действующий на основе спина, необходимо последовательно внимательно изучить свойства переноса спина в полупроводниках. Так как кремний является наиболее широко применяемым материалом в современной микроэлектронике, изучение спиновой релаксации в кремниевых каналах представляет первостепенный интерес. Механическое напряжение широко используется для увеличения подвижности носителей в современных МОП-структурах. В диссертации $\mathbf{k}\cdot\mathbf{p}$ метод используется для изучения зонной структуры и волновых функций в низкоразмерных электронных системах кремниевых плёнок в присутствии деформации сдвига и спин-орбитального взаимодействия. Аналитические выражения для волновых функций, полученных с помощью четырёхзонного $\mathbf{k}\cdot\mathbf{p}$ гамильтониана построены для прямоугольной потенциальной ямы. Волновые функции используются для вычисления соответствующих матричных элементов спиновой релаксации. Учитываются вклады от шероховатости поверхности и электрон-фононного взаимодействия во время жизни спина. Вырождение двух нижних подзон снимается под действием сдвиговой деформации, что приводит к уменьшению доминирующего вклада от упругого междолинного спинового рассеяния. Таким образом, предсказывается увеличение времени жизни спина более чем на порядок в плёнках кремния, подвергнутых деформации.

Применение кремния в спиновом полевом транзисторе представляет значительный интерес, так как это обещает создать спиновые устройства, используя хорошо развитую технологию обработки кремния. Из-за нарушения симметрии, вызванного анизотропией химических связей на интерфейсах (интерфейсно-инверсионная

асимметрия), эффективное спин-орбитальное взаимодействие, определяемое электрическим полем, оказывается сильнее в тонких кремниевых плёнках и пластинах. Показано, что в случае искуственно созданных барьеров Шоттки между истоком/стоком и каналом, модуляция магнетосопротивления остаётся достаточно выраженной даже при комнатной температуре. Для уменьшения длины канала, эффективная масса вдоль него должна быть большой. На основе двухзонной $\mathbf{k}\cdot\mathbf{p}$ модели для зоны проводимости показано что зависимость магнетосопротивления от величины эффективного спин-орбитального взаимодействия в спиновых транзисторах с кремниевым каналом будет сильнее вдоль направления [100]. Это делает их практическое применение более предпочтительным.

Acknowledgement

First I want to thank *Prof. Siegfried Selberherr* who provided me his full support, that made it finally possible to finish this thesis. Also I thank *Prof. Selberherr* for the working environment that surrounded me and the possibility to participate in international conferences which enriched this research.

My deepest gratitude goes to my advisor, *Privatdoz. Viktor Sverdlov*, without whom it would be impossible to do this work. He introduced me to spin physics, strained silicon, the **k·p** method, and showed me how to apply it.

I also thank *Privatdoz. Dr. Dieter Suess* for serving on my examination committee.

I would like to thank *Prof. Erasmus Langer*, the head of the Institute for Microelectronics, for taking care of all the bureaucracy and providing me with numerous support letters for different visas.

I would like to thank *Dr. Thomas Windbacher* who helped me a lot in solving different problems from sending CO_2 capsules across the border to proofreading this thesis.

During my work at the institute I had the pleasure to collaborate on different levels with many other colleagues I have a high regard for: *Dr. Alexander Makarov, Dr. Stanislav Tyaginov, Dr. Lado Filipovic, Dr. Ivan Starkov, Dr. Mihail Nedjalkov, Dr. Josef Weinbub, Paul Ellinghaus, Dr. Roberto Orio, Dr. Wolfgang Gös, Dr. Karl Rupp, Zlatan Stanojevic, Oskar Baumgartner, Dr. Neophytos Neophytou, Yury Illarionov, Dr. Vassil Palankovski.*

Besides the Institute I was fortunate to meet *Georg Franschitz* who showed me all beauties of Austria that are reachable by bike: from Vienna to the top of the Großglockner. The Bike-Wochenende and the Österreich-Radrundfahrt 2013 together with *Günther Teubersen, Rudolf Paul, Paul Ellinghaus* and all other cycling partners made my past years brilliant.

I would like to thank *Dmitry Kryzhanovsky* without whose support and assistance, I would never have started working in this institute.

Finally, but not least, I want to thank my parents *Irina* and *Sergey* and my brother *Konstantin* for the endless support and faith in me. My gratitude to them is hard to describe by words.

Contents

List of Figures

List of Symbols

T	temperature
m_0	electron rest mass
a	lattice constant
c	speed of light
U	confinement potential
V	bulk crystal potential
$\mathcal{H}$	Hamiltonian
$\sigma_x, \sigma_y, \sigma_z$	Pauli matrices
t	film thickness
$\mathbf{K}$	wave vector
E_F	Fermi energy
$T_{\uparrow(\downarrow)}$	spin-up (spin-down) transmission probability
G	conductance
P	spin polarization
B	magnetic field
g	Landé factor
z	strength of the Schottky barriers
h_0	exchange splitting energy
α_R	strength of the spin-orbit interaction (Rashba-like)
β	strength of the spin-orbit interaction (Dresselhaus-like)
μ_B	Bohr magneton
δE_C	subband mismatch between ferromagnetic region and channel
m_f^*	effective mass for the ferromagnetic region
m_s^*	effective mass for the semiconductor region
τ	momentum (spin) lifetime
ε_{xy}	shear strain component
m_t	transversal silicon effective mass
m_l	longitudinal silicon effective mass
θ	polar angle defining the orientation of the injected spin
φ	azimuth angle defining the orientation of the injected spin
ϵ	dielectric permittivity
L	autocorrelation length
Δ	mean square value of the surface roughness fluctuations
E	electron energy
ρ	density

ΔE_C	conduction band offset
Δ_Γ	splitting at the Γ-point
Δ_{SO}	spin-orbit splitting
k_0	position of the valley minimum relative to the X-point in unstrained silicon
$k_{0\Gamma}$	position of the valley minimum relative to the Γ-point in unstrained silicon
ω_{op}	frequency of the optical phonons
D	shear strain deformation potential
Ξ	acoustic deformation potential
D_{op}	optic deformation potential

List of Constants

$$
\begin{aligned}
k_B &= 8.617332478 \cdot 10^{-5} & &\text{eV/K} \\
\mu_B &= 5.7883818066 \cdot 10^{-5} & &\text{eV/T} \\
\hbar &= 1.05457172647 \cdot 10^{-34} & &\text{Js} \\
m_0 &= 9.1093829140 \cdot 10^{-31} & &\text{kg} \\
e &= 1.60217656535 \cdot 10^{-19} & &\text{C} \\
c &= 299792458 & &\text{m/s} \\
m_t &= 0.19 m_0 \\
m_l &= 0.91 m_0 \\
M &= \left(m_t^{-1} - m_0^{-1} \right)^{-1} \\
L &= 15 \cdot 10^{-10} & &\text{m} \\
\Delta &= 3 \cdot 10^{-10} & &\text{m} \\
\rho &= 2329 & &\text{kg/m}^3 \\
\upsilon_{TA} &= 5300 & &\text{m/s} \\
\upsilon_{LA} &= 8700 & &\text{m/s} \\
a &= 5.431 \cdot 10^{-10} & &\text{m} \\
k_0 &= 0.15 \cdot 2\pi/a \\
k_{0\Gamma} &= 0.85 \cdot 2\pi/a \\
D &= 14 & &\text{eV} \\
\Xi &= 12 & &\text{eV} \\
D_{SO} &= 15 & &\text{meV}/k_0 \\
D_{op} &= 6.5 & &\text{meV} \cdot 2\pi/a \\
\Delta_{SO} &= 1.27 & &\text{meVnm} \\
\omega_{op} &= 9.29791719\text{e}13 & &\text{Hz} \\
g &= 2
\end{aligned}
$$

1 Introduction

Spin-dependent effects attract a great attention since 1922 when the German physicists Otto Stern and Walther Gerlach performed an experiment that confirmed that atoms have an intrinsic angular momentum, whose projection on a chosen axis is quantized. [40]. Thereafter the spin hypothesis was introduced in 1925 by Samuel Goudsmit and George Uhlenbeck. The spin concept had been accepted since it helped to describe thin spectral lines in Zeeman spectra [126]. During the following couple of decades the concept of spin had been used by Werner Heisenberg to explain ferromagnetism [18], then Wolfgang Pauli introduced particle statistics (fermions – particles that obey Fermi-Dirac statistics and are characterized by half-integer spin, and bosons – particles that obey Bose-Einstein statistics and are characterized by integer spin) [127], and nuclear magnetic resonance (NMR) spectroscopy was invented. Since the 1950s magnetic effects are widely used to store data. The first devices were quite large and were only able to store several tens of kilobytes of data. Advances in technologies made it possible to increase the storage data density significantly [120].

In 1971 Mikhail D'yakonov and Vladimir Perel' predicted a spin Hall effect - a spin flow in the direction perpendicular to the current [25]. The first experimental confirmation of the prediction has been made by Vorob'ev [119]. Vorob'ev et al. observed a change in the rotation rate of the plane of the polarization of light propagated in a Te crystal. The same effect was demonstrated by Yuichiro Kato in 2004 [63]. Kato used $GaAs$ to demonstrate electrically induced electron-spin polarization near the edges of a semiconductor channel. In 1976 Arkady Aronov and Gregory Pikus proposed an idea that spin-polarized current can be injected into a semiconductor when a current is passed through a ferromagnet/semiconductor junction [6]. Santos F. Alvarado and Philippe Renaud in 1992 observed the experimental evidence for the tunneling of polarized electrons from the apex of a ferromagnetic Ni tip into $GaAs$(110) [4].

The most impressive result of spin electronics is the giant magnetoresistant (GMR) effect used in hard drives and magnetic random access memory. The giant magnetoresistance is the quantum-mechanical effect observed in thin ferromagnetic films that are connected by a thin metallic film. The effect causes a considerable change of resistance in such structure if the orientation of ferromagnetic layers changes from parallel to antiparallel. This effect is based on the scattering of electrons depending on their spin orientation relative to the magnetization direction. The direction of the magnetization of the ferromagnetic layer can be controlled by an external magnetic field. The Physics Nobel Prize in 2007 was given to Peter Grimberg and Albert Fert

for the discovery of the giant magnetoresistance [3]. The resistance change between spin parallel and spin antiparallel arrangements can also be observed in magnetic tunnel junctions. Studies on the tunneling magnetoresistance (TMR) effect have been advanced recently resulting further improvement of recording heads was achieved by using TMR [93, 105, 132].

The last decades success in digital electronics has been provided by the advances in silicon chip developments and its core idea that the information in microelectronic devices can be stored and manipulated by controlling the electron charge. According to the well-known Moore's law the number of transistors on a chip doubles approximately every two years [78, 79]. However, the International Technology Roadmap for Semiconductors (ITRS) in 2010 predicted that the trend will slow down to a three-year cycle [1]. The increase of the number of transistors leads to an increase of the power consumption and speed of the chip. Since 1965 when this trend was described by Gordon E. Moore the progress has followed this exponential trend. This trend in silicon–based computing will come to an end in the next decades. When the capabilities of miniaturization become limited by an atom size. The size reduction leads to large leakages currents that can be reduced by strain techniques, the use of high-K dielectric materials, and tri-gate FET. The classic scaling ended at 130nm [66] but these new boosters keep the trend up. Although an atomic size is an ultimate limit. The real stopper of scaling happen earlier due to high costs and is likely to economical-based motivation [98, 99].

In 1990 a device that does not use charge to process information but spin orientation was proposed by Supriyo Datta and Biswajit Das. This device is commonly called Datta-Das transistor or spin field-effect transistor (SpinFET). The potential advantages of such a device are to go beyond conventional silicon-based transistors. The physical principles behind the SpinFET are similar as for the tunneling magnetoresistance effect.

Electrical and optical spin manipulation is possible due to spin-orbit coupling, that makes the spin degree of freedom respond to its orbital environment [125]. In semiconductor nanostructures the strength of the spin-orbit coupling depends on the symmetry of the system, its geometric and energy parameters, which can vary over a wide range of values [125]. Current research is governed by the fact that utilizing spin properties of electrons for future microelectronic devices opens great opportunities to reduce the device power consumption. In recent years spintronic devices, where the spin of the electron is used as an additional degree of freedom to tune their properties, have received much attention [31, 128, 136].

2 Motivation

In order to achieve significant advances in future microelectronic devices in comparison to present technology, their operation principles will have to be enhanced or even modified. Spintronics is a rapidly developing technology promising to benefit from the spin properties of electrons. Utilizing spin opens great opportunities to reduce the device power consumption in future electronic circuits. A number of potential spintronic devices have already been proposed [22, 109]. Significant efforts are focused on developing models to study the properties of future devices through simulations [26].

Silicon is the primary material for microelectronics. The long spin life time in silicon is a consequence of the weak intrinsic spin-orbit coupling in the conduction band and the spatial inversion symmetry of the lattice resulting in an absence of the Dresselhaus effective spin-orbit interaction [56, 70]. In addition, silicon is composed of nuclei with predominantly zero magnetic moment. A long spin transport distance of conduction electrons in silicon has already been demonstrated experimentally [48]. Spin propagation at such distances combined with a possibility of injecting spin at room temperature [21] or even elevated temperature [69] in silicon makes the fabrication of spin-based switching devices quite plausible in the upcoming future [49, 52]. However, the relatively large spin relaxation experimentally observed in electrically-gated lateral-channel silicon structures [56] might become an obstacle for realizing spin driven devices [70], and a deeper understanding of the fundamental spin relaxation mechanisms in silicon MOSFETs is urgently needed [107].

In this work the influence of the intrinsic spin-orbit interaction on the subband structure, subband wave functions, and spin relaxation matrix elements due to the surface roughness scattering in thin silicon films is investigated. An efficient approach allowing to analyze surface roughness and phonon induced spin and momentum relaxation in thin silicon films is developed.

A $\mathbf{k \cdot p}$ based method [9, 111] suitable to describe the electron subband structure in the presence of strain is generalized to include the spin degree of freedom [70]. In contrast to [70], the effective 4×4 Hamiltonian considers only the relevant [001] oriented valleys with spin degree included, which produces the low-energy unprimed subband ladder. Within this model the unprimed subbands in the unstrained (001) film are degenerate, without spin-orbit effects included. An accurate inclusion of the spin-orbit interaction results in a large mixing between the spin-up and spin-down states, resulting in spin hot spots along the [100] and [010] axes characterized by strong spin relaxation. These hot spots should be contrasted with the spin hot spots appearing in the bulk system

along the same directions at the edge of the Brillouin zone [17, 70]. The origin of the hot spots in thin films lies in the unprimed subband degeneracy which effectively projects the bulk spin hot spots from the edge of the Brillouin zone to the center of the 2D Brillouin zone.

Shear strain lifts the degeneracy between the unprimed subbands [111]. The energy splitting between the otherwise equivalent unprimed subbands removes the origin of the spin hot spots in a confined electron system in silicon, which substantially improves the spin lifetime in gated silicon systems. Thus, shear strain applying to thin silicon films reduces the spin relaxation.

Spin field-effect transistors (SpinFETs) are promising candidates for future integrated microelectronic circuits. A SpinFET is composed of two ferromagnetic contacts (source and drain), which sandwich a semiconductor channel. Current modulation is achieved by electrically tuning the gate voltage dependent strength of the spin-orbit interaction in the semiconductor region. A study of the transport properties of the Datta–Das spin field-effect transistor is needed to make more reliable predictions on operation regime for such devices.

3 Outline of the Thesis

Following the introduction and motivation described above, the concrete structure of the thesis is outlined as follows.

Chapter 4 provides an introduction to the band structure calculations. Principles of the cellular and the variational methods are described. Then the $\mathbf{k \cdot p}$ method and the mechanisms of the spin relaxation in semiconductors are presented.

Chapter 5 starts from the two-band $\mathbf{k \cdot p}$ Hamiltonian with shear strain and spin properly included. The presented Hamiltonian is then rotated and a semi-analytical wave function calculation procedure is shown. The analytical solution is compared against numerically calculated results. The wave functions and the valley splitting is then investigated for different film thicknesses, values of the in-plane wave vector, and shear strain.

Chapter 6 presents a surface roughness matrix elements calculation procedure and investigates intrasubband and intersubband matrix elements. Then the model for momentum relaxation time for surface roughness limited and phonon induced momentum scattering rates is described. Afterwards the results for mobility and momentum relaxation time are provided.

Chapter 7 starts from the surface roughness limited spin relaxation matrix elements calculation and the origin of hot spots are disclosed. Then spin lifetime due to intravalley, intervalley scattering between equivalent and non-equivalent valleys, and surface roughness spin relaxation is calculated. The inclusion of zero-strain valley splitting is performed by considering the valley coupling through the Γ-point.

Chapter 8 shows the three-layer Datta-Das spin field effect transistor (SpinFET) model and presents the results of tunneling magnetoresistance oscillations for the SpinFET with silicon and InAs channels.

4 Band Structure Calculations

The electron's transport peculiarities determine the performance of most modern devices. In order to describe these peculiarities the band structure must be known. In other words the dependence of electron energy on wave vector $\mathbf{k}$ in different electron bands n, $E_n(\mathbf{k})$ and relative positions of one band to another are decisive. Current level of technologies makes it possible to change the band structure of a material purposefully to achieve certain characteristics.

The energy spectrum of an electron in a crystal is determined by the Schrödinger equation

$$\left(-\frac{\hbar^2}{m_0}\nabla^2 + U(\mathbf{r})\right)\Psi(\mathbf{r}) = E\Psi(\mathbf{r}), \tag{4.1}$$

where $U(\mathbf{r})$ is the periodic crystal potential and m_0 is the electron rest mass.

To find the eigenfunctions and the eigenvalues of Equation 4.1 the two following task should be solved – determine the periodic potential and solve Equation 4.1 for the determined potential. Unfortunately the exact solution requires significant calculation recourses, thus approximate methods come into play. The task of finding the right kind of periodic potential for a given problem, is the most important part to obtain the correct solution. The second part of the solution is much more investigated. There are several methods available that allow to calculate the energy spectrum in metals and semiconductors with sufficient accuracy to reproduce experimental results.

The general idea behind most of the developed methods to solve Equation 4.1 is that every solution can be expanded in an infinite series by using a complete basis satisfying the same boundary conditions as the solution.

$$\Psi(\mathbf{r}) = \sum_{i=1}^{\infty} c_i \Psi_i(\mathbf{r}). \tag{4.2}$$

The approximate solution can be obtained by taking a finite number of terms in the expansion. Functions Ψ_1, Ψ_2, $\Psi_3, \cdots, \Psi_n$ are chosen to satisfy the boundary conditions. The following linear combination is taken for approximation

$$\Psi(\mathbf{r}) \approx \sum_{i=1}^{n} c_i \Psi_i(\mathbf{r}). \tag{4.3}$$
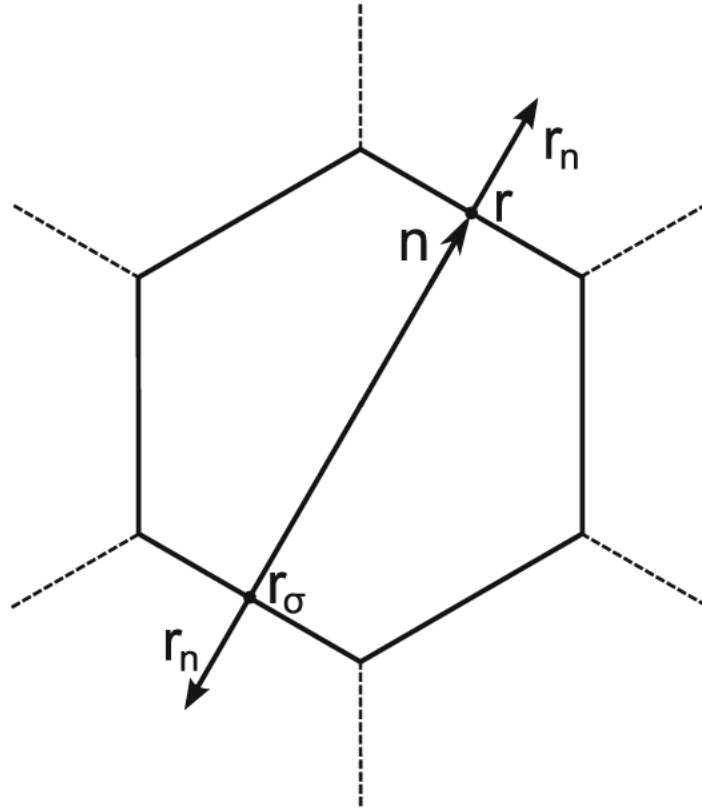
Figure 4.1: Conjugate points on the boundary of Wigner-Seitz polyhedron.

In order to understand how to choose proper functions $\Psi_i(\mathbf{r})$ consider the following Bloch function

$$\Psi_{n\mathbf{k}}(\mathbf{r}) = u_{n\mathbf{k}}(\mathbf{r})e^{i\mathbf{k}\mathbf{r}}. \tag{4.4}$$

This function has a plane wave factor. The plane wave is additionally modulated by factor $u_{n\mathbf{k}}(\mathbf{r})$. The factor $u_{n\mathbf{k}}(\mathbf{r})$ has the same period as the lattice. Close to atomic lattice sites the wave functions behave like the wave function for atoms, i.e. changes the Bloch amplitude fast. While far away from the atomic lattice sites the wavefunctions behave like plane waves and like atomic functions close to the sites.

The behavior of wave functions near the lattice sites and between the sites leads to the idea that either plane or spherical functions can be used in the linear combination (4.3). Based on this all methods that are used for band structure calculation are divided into two categories: variational methods and cellular methods.

4.1 The Cellular Method

The cellular method was developed by Wigner and Seitz in 1933 [122]. The method utilizes the periodicity of the eigenfunctions of Equation 4.1, due to the periodic poten-

tial $U(\mathbf{r})$. This periodicity makes it possible to restrict the task of finding eigenvalues and eigenfunctions to one primitive cell – the Wigner-Seitz cell. The Wigner-Seitz cell has a polyhedron shape that is limited by planes perpendicular to and passing through the midpoint of a line connected to an lattice point in the middle of the cell and its neighbors. Thus, the Wigner-Seitz cell built for an atom covers a region of space that is closer to the current atom than to the others. Such cells fill all the area (for two dimensional) or the volume (for 3D) of a crystal therefore it is enough to find a solution of Equation 4.1 in such a cell. The boundary conditions are the following

$$\Psi_{\mathbf{k}}(\mathbf{r}_\sigma) = \mathrm{e}^{i\mathbf{k}\mathbf{n}}\Psi_{\mathbf{k}}(\mathbf{r}), \tag{4.5}$$

$$\frac{\partial \Psi_{\mathbf{k}}(\mathbf{r}_\sigma)}{\partial \mathbf{r}_n} = -\mathrm{e}^{i\mathbf{k}\mathbf{n}}\frac{\Psi_{\mathbf{k}}(\mathbf{r})}{\partial \mathbf{r}_n}, \tag{4.6}$$

where $\mathbf{r}$ and $\mathbf{r}_\sigma$ are location vectors of conjugate points on the surface of the Wigner-Seitz's polyhedron, $\mathbf{n}$ is the translation vector connecting these points or cell's centers, $\dfrac{\partial \Psi_{\mathbf{k}}(\mathbf{r}_\sigma)}{\partial \mathbf{r}_n}$ and $\dfrac{\Psi_{\mathbf{k}}(\mathbf{r})}{\partial \mathbf{r}_n}$ are normal derivatives at the point $\mathbf{r}_\sigma$ and $\mathbf{r}$, respectively, $\mathbf{r}_n$ is the outer normal for the surface of polyhedron.

Equation 4.5 is the condition for periodicity. The Solution on the edge of the cell can be found by multiplying the solution at the opposite edge by the factor $\mathrm{e}^{i\mathbf{k}n}$. Equation 4.6 ensures solutions continuity and smoothness at the boundary of a cell.

The solution of the Schrödinger equation is sought in the form of a linear superposition of self-consistent atomic wave functions and radial functions. Such a representation of a wave function is valid under the assumption that the crystal potential in the small area around an atom inside each cell is symmetric. Wave function expansion coefficients are chosen in such a way that they meet the boundary conditions for the finite number of points at the surface of the cell. The described method has one considerable obstacle. Since the Wigner-Seitz cell usually has a complicated structure the use of boundary conditions in a direct way is almost impossible. Therefore, a simplified approach was developed. For this approach the boundary conditions are only being required to be satisfied in the middle of the edges. The results were not very precise, however, they were good qualitatively. Attempts to improve the results by including more points made the solution more complicated without significant improvement of the precision. To avoid the difficulties caused by the boundary conditions the simplest approximation can be applied. In this case a polyhedron is replaced by a sphere of the same volume

$$\Omega = \frac{4}{3}\pi r_s^3, \tag{4.7}$$

where r_s is the radius of Wigner-Seitz sphere.

The boundary conditions are then simplified to requirements for the wave function and its derivative continuity on the boundary of the sphere. Under these boundary conditions the solution is considerably simplified. However, such an approximation can not describe any state of a crystal. These conditions are only good enough for s-type states.

4.2 Variational Methods

Variational methods reduce the solution of the differential equation (4.1) to the variational problem of the minimization of the functional Λ

$$\delta\Lambda = 0. \tag{4.8}$$

By substituting Equation 4.3 into Equation 4.1 and then multiplying by the complex conjugate wave function and integrating over the crystal volume one can get the following system of algebraic equations

$$\sum_{i=1}^{n} \left(\mathcal{H}_{ji} - ES_{ji}\right) c_i = 0 \; j = 1, 2, \cdots, n, \tag{4.9}$$

where $\mathcal{H}_{ji}$ and S_{ji} are written as

$$\mathcal{H}_{ji} = \int \Psi_j^* H \Psi_i d\mathbf{r}, \tag{4.10}$$

$$S_{ji} = \int \Psi_j^* \Psi_i d\mathbf{r}. \tag{4.11}$$

Here $S_{ji} \neq \delta_{ji}$ since the functions Ψ_i and Ψ_j are not necessary orthonormal.

The system of equations (4.9) has a non-trivial solution only if determinant is equal to zero

$$\det |\mathcal{H}_{ji} - ES_{ji}| = 0. \tag{4.12}$$

The characteristic equation (4.12) allows to find the eigenvalues, and then the eigenfunctions can be found by using Equation 4.9. Equation 4.12 has n solutions on E. The smallest solution is approximately equal to the energy of the lowest state. The higher solutions give energies of excited states. In general the quality of the solution at higher energies is worse than the lowest solution. The task of finding the eigenvectors and the eigenfunctions for Equation 4.1 by taking into account the boundary conditions Equation 4.5 and Equation 4.6 then can be reduced to a variational task of minimizing of functional

$$\Lambda[\Psi, \Psi^*, E] = \int \Psi^* \left(\mathcal{H} - E\right) \Psi d\mathbf{r}, \tag{4.13}$$

where functions Ψ satisfy the boundary conditions.

A specific form of the characteristic equation (4.12) depends on the form of the functional (4.13), probe wave functions and boundary conditions. The order of the equation is determined by number of parameters c_i, which is determined by number of basis
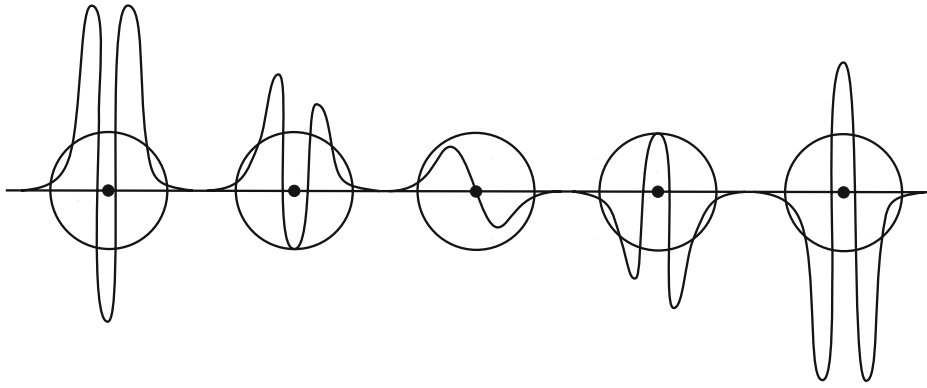
Figure 4.2: Atomic wave.
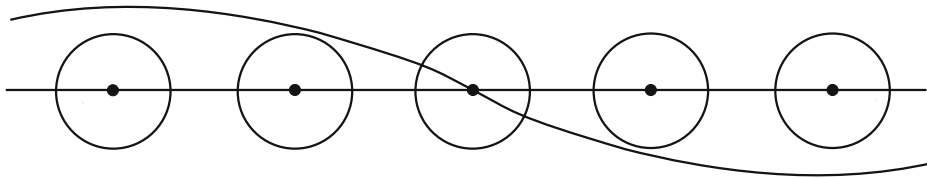
Figure 4.3: Plane wave.

functions Ψ_i that is used to get a good approximation of Ψ. Thus, the quality of the approximation depends on a good choice of probe functions Ψ_i.

The described approach is general and in order to solve the Schrödinger equation for a real crystal by a composition of wave functions consisting only of plane waves or only of atomic waves not quite satisfactory from a physical point of view.

Actually, low lying bands are fully filled and described by wave functions that oscillate near the atom (Figure 4.2), while valence bands are characterized by wave functions equally distributed over the crystal (Figure 4.3). For the first case methods based on atomic waves are suitable to find a good solution for the equation. For the second case an approximation based on plane waves for the practically free electrons is suitable. The most interesting area for practical tasks is the intermediate region of the electron's energy spectrum - for semiconductors it is the conduction and the valence bands.

A lot of efforts were taken to create a procedure for constructing basic wave functions that take into account both tendencies. An important point here is to build a procedure that allows to calculate wave functions in the most efficient (in the terms of numerical costs) way. The methods differ in the probe wave functions they are using.

All methods for the band structure calculation can be distinguished by the way the potential is built. Self-consistent methods use only atomic constants as parameters. Empirical methods use experimental data to get the best fit of the theoretical results in comparison to the experiments. Pure theoretical predictions of the band structure can be made only from self-consistent methods. The inconsistency of these predictions with regard to experimental results is a consequence of the approximations that are

used for the calculations. The weakness of the empirical methods is their dependence on the parameters that are determined from experimental data.

Currently, all methods show approximately equal accuracy for energies below 0.5eV. Thus, the band structures obtained for energies below 0.5eV may be considered as correctly reproduced.

4.3 The k·p Method

The method was first introduced by Seitz in 1935 [104], then it was extended by Luttinger [73], Kane [61] and Cardona [16]. As it was discussed earlier the eigenfunctions for one electron approximation for the Schrödinger equation

$$\mathcal{H}\Psi = \left(\frac{\mathbf{p}^2}{2m_0} + U(\mathbf{r})\right)\Psi = E\Psi,\tag{4.14}$$

are the Bloch functions

$$\Psi = e^{i\mathbf{k}\mathbf{r}}u_{n\mathbf{k}}(\mathbf{r}),\tag{4.15}$$

where $\mathbf{p} = -i\hbar\nabla$ is the operator of the electron momentum, n is the band index, m_0 is the electron rest mass, and the wave vector $\mathbf{k}$ is limited by the first Brillouin zone. By inserting Equation 4.15 to Equation 4.14 one gets

$$\mathcal{H}_\mathbf{k}u_{n\mathbf{k}}(\mathbf{r}) = \left(\frac{\mathbf{p}^2}{2m_0} + \frac{\hbar}{m_0}\mathbf{k}\mathbf{p} + U(\mathbf{r})\right)u_{n\mathbf{k}}(\mathbf{r}) = E_n(\mathbf{k})u_{n\mathbf{k}}(\mathbf{r}).\tag{4.16}$$

The term $\dfrac{\hbar}{m_0}\mathbf{k}\mathbf{p}$ of Equation 4.16 is absent in Equation 4.14. This term can be considered as a perturbation. Thus, the term is called **kp**-perturbation.

The solution of Equation 4.16 is sought as an expansion $u_{\mathbf{k}n}$ in a complete set of functions. For a fixed $\mathbf{k}$ the set of $u_{\mathbf{k}n}$ can be expanded as

$$u_{\mathbf{k}n}(\mathbf{r}) = \sum_{n'} A_{nn'}(\mathbf{k} - \mathbf{k_0})u_{n'\mathbf{k_0}}(\mathbf{r}).\tag{4.17}$$

By isolating some part $\mathcal{H}_{\mathbf{k_0}}$ from $\mathcal{H}_\mathbf{k}$, Equation 4.16 can be written in the following form

$$\left(\mathcal{H}_{\mathbf{k_0}} + \frac{\hbar}{m_0}(\mathbf{k} - \mathbf{k_0}, \mathbf{p}) + \frac{\hbar^2(k^2 - k_0^2)}{2m_0}\right)u_{n\mathbf{k}}(\mathbf{r}) = E_n(\mathbf{k})u_{n\mathbf{k}}(\mathbf{r}),\tag{4.18}$$

where

$$\mathcal{H}_{\mathbf{k_0}} = \frac{\mathbf{p}^2}{2m_0} + \frac{\hbar}{m_0}\mathbf{k_0}\mathbf{p} + \frac{\hbar^2 k_0^2}{2m_0} + U(\mathbf{r}).\tag{4.19}$$

By substituting Equation 4.17 into Equation 4.18, multiplying by $u_{n\mathbf{k_0}}^*$, and integrating over the elementary cell one can get the following system of equations

$$\sum_{n'} \left(\left(E_n(\mathbf{k_0}) + \frac{\hbar^2}{2m_0}(k^2 - k_0^2) \right) \delta_{nn'} + \frac{\hbar}{m_0}(\mathbf{k} - \mathbf{k_0}, \mathbf{p}_{nn'}(\mathbf{k_0})) \right) A_{nn'} = E_n(\mathbf{k})A_{nn'}, \tag{4.20}$$

where

$$\mathbf{p}_{nn'}(\mathbf{k_0}) = \langle u_{n\mathbf{k_0}}|\mathbf{p}|u_{n'\mathbf{k_0}}\rangle = \int_{\Omega_0} u_{n\mathbf{k_0}}^* \mathbf{p} u_{n'\mathbf{k_0}} d\mathbf{r} \tag{4.21}$$

is the matrix element of momentum operator for the point $\mathbf{k} = \mathbf{k_0}$. It is taken into account that functions u are orthogonal and normalized inside elementary cell

$$\int_{\Omega_0} u_{n\mathbf{k_0}}^* u_{n'\mathbf{k_0}} d\mathbf{r} = \delta_{nn'}. \tag{4.22}$$

The system of equations (4.20) is solvable if the following determinant is zero

$$\det \left| \left[E_n(\mathbf{k_0}) - E_n(\mathbf{k}) + \frac{\hbar^2}{2m_0}(k^2 - k_0^2) \right] \delta_{nn'} + \frac{\hbar}{m_0}(\mathbf{k} - \mathbf{k_0}, \mathbf{p}_{nn'}(\mathbf{k_0})) \right| = 0. \tag{4.23}$$

The secular equation (4.23) is used to find the eigenvalues $E_n(\mathbf{k})$. To find out the dependencies of $E_n(\mathbf{k})$, energies and matrix elements for all bands should be known for some $\mathbf{k} = \mathbf{k_0}$. These values are usually obtained from experimental data. Pollak and Cordona [16] calculated $E_n(\mathbf{k})$ by using the $\mathbf{k} \cdot \mathbf{p}$ method for a number of semiconductors (*Si, Ge, GaAs, GaP, InP*).

4.4 Perturbation Theory

Frequently an exact solution of the Schrödinger equation can not be found. For a Hamiltonian that can be divided into two parts in such way that one part is much bigger than the other part a perturbation theory can be applied in order to find a solution. Consider the following Hamiltonian

$$\mathcal{H} = \mathcal{H}_0 + V. \tag{4.24}$$

Here V is a small correction to the unperturbated Hamiltonian $\mathcal{H}_0$. The task that the perturbation theory fulfills is to find approximate solutions for the eigenenergies E and the eigenfunctions Ψ of the following equation

$$\mathcal{H}\Psi = (\mathcal{H}_0 + V)\Psi = E\Psi, \tag{4.25}$$

provided that the eigenvectors $E^{(0)}$ and the eigenfunctions $\Psi^{(0)}$ for the unperturbated Hamiltonian are known, the eigenfunctions Ψ_n in the second order of approximation can be determined as

$$\Psi_n = \Psi_n^{(0)} + \Psi_n^{(1)} + \Psi_n^{(2)}, \tag{4.26}$$

where $\Psi_n^{(1)}$ and $\Psi_n^{(2)}$ are the first and the second order correction of the eigenfunction written as [137]

$$\Psi_n^{(1)} = \sum_{m \neq n} \frac{V_{mn}}{E_n^{(0)} - E_m^{(0)}} \Psi_m^{(0)}, \tag{4.27}$$

$$\Psi_n^{(2)} = \sum_{m \neq n} \left[-\frac{V_{nn} V_{mn}}{\left(E_n^{(0)} - E_m^{(0)}\right)^2} + \sum_{k \neq n} \frac{V_{mk} V_{kn}}{\left(E_n^{(0)} - E_m^{(0)}\right)\left(E_n^{(0)} - E_k^{(0)}\right)} \right] \Psi_m^{(0)}, \tag{4.28}$$

with

$$V_{mn} = \int \Psi_n^{(0)} V \Psi_m^{(0)} dq, \tag{4.29}$$

where V defined as an perturbation operator.

The eigenenergies E_n in the second order of approximation are written as

$$E_n = E_n^{(0)} + E_n^{(1)} + E_n^{(2)}, \tag{4.30}$$

with the first $(E_n^{(1)})$ and the second $(E_n^{(1)})$ order corrections written as

$$E_n^{(1)} = V_{nn} = \int \Psi_n^{(0)} V \Psi_n^{(0)} dq. \tag{4.31}$$

$$E_n^{(2)} = \sum_{m \neq n} \frac{|V_{mn}|^2}{E_n^{(0)} - E_m^{(0)}}. \tag{4.32}$$

The condition under which the perturbation theory is applicable is

$$|V_{mn}| \ll \left| E_n^{(0)} - E_m^{(0)} \right|. \tag{4.33}$$

Namely matrix elements of the perturbation should be much smaller than the difference between the unperturbated energy levels.

However, even though the $\mathbf{k} \cdot \mathbf{p}$ method is valid for all values $\mathbf{k}$, this method is most useful for the calculation of the energy spectrum in the vicinity of the high symmetry

point $\mathbf{k_0}$. If $\mathbf{k} - \mathbf{k_0}$ is small enough then operator $\dfrac{\hbar}{m_0}(\mathbf{k} - \mathbf{k_0}, \mathbf{p}) + \dfrac{\hbar^2(k^2 - k_0^2)}{2m_0}$ in Equation 4.18 can be considered as a small perturbation to $\mathcal{H}_{\mathbf{k_0}}$ and

$$\frac{\hbar}{m_0}(\mathbf{k} - \mathbf{k_0}, \mathbf{p}_{nn'}) + \frac{\hbar^2(k^2 - k_0^2)}{2m_0} \tag{4.34}$$

are a small correction to the energy $E_n(\mathbf{k_0})$.

By applying the perturbation theory to the equation for the energy close to the $\mathbf{k_0}$ point it can be written

$$E_n(\mathbf{k}) = E_n(\mathbf{k_0}) + \frac{\hbar^2}{2}\sum_{\alpha,\beta=1}^{3}\left(\frac{1}{m_{\alpha,\beta}}\right)_n(\mathbf{k}_\alpha - \mathbf{k}_{0\alpha})(\mathbf{k}_\beta - \mathbf{k}_{0\beta}), \tag{4.35}$$

where $\dfrac{1}{m_{\alpha,\beta}}$ are the components of the inverse effective mass tensor.

4.5 Effective Mass

Consider a free electron that has rest mass m_0 in a uniform electric field $\vec{\mathcal{E}}$. The force acting on the electron is

$$\vec{F} = -|e|\vec{\mathcal{E}}. \tag{4.36}$$

The force is directed against the field $\vec{\mathcal{E}}$ and related to the electron acceleration by the following expression

$$\vec{a} = \frac{1}{m_0}\vec{F} = \frac{|e|\vec{\mathcal{E}}}{m_0}. \tag{4.37}$$

By taking into account the expressions for the velocity $\vec{v}$ and the impulse derivative over time $\dfrac{d\vec{p}}{dt}$ for an electron in a crystal in a uniform electric field

$$\vec{v} = \frac{dE}{d\vec{p}}, \tag{4.38}$$

$$\frac{d\vec{p}}{dt} = \vec{F}, \tag{4.39}$$

acceleration can be rewritten as

$$\vec{a} = \frac{d\vec{v}}{dt} = \frac{\partial\vec{v}}{\partial\vec{p}}\frac{\partial\vec{p}}{\partial t} = \frac{\partial^2 E}{\partial\vec{p}^2}\vec{F}. \tag{4.40}$$

By generalizing Equation 4.40 for the three-dimensional case one gets

$$a_x = \frac{\partial^2 E}{\partial p_x^2} F_x + \frac{\partial^2 E}{\partial p_x \partial p_y} F_y + \frac{\partial^2 E}{\partial p_x \partial p_z} F_z,$$

$$a_y = \frac{\partial^2 E}{\partial p_x \partial p_y} F_x + \frac{\partial^2 E}{\partial p_y^2} F_y + \frac{\partial^2 E}{\partial p_x \partial p_z} F_z, \qquad (4.41)$$

$$a_z = \frac{\partial^2 E}{\partial p_x \partial p_z} F_x + \frac{\partial^2 E}{\partial p_y \partial p_z} F_y + \frac{\partial^2 E}{\partial p_z^2} F_z.$$

The set of values $\dfrac{\partial^2 E}{\partial p_i \partial p_j} = \dfrac{1}{m_{ij}}$, that connected acceleration and force are the second rank tensor

$$m^{-1} = \begin{bmatrix} \dfrac{\partial^2 E}{\partial p_x^2} & \dfrac{\partial^2 E}{\partial p_x \partial p_y} & \dfrac{\partial^2 E}{\partial p_x \partial p_z} \\ \dfrac{\partial^2 E}{\partial p_x \partial p_y} & \dfrac{\partial^2 E}{\partial p_y^2} & \dfrac{\partial^2 E}{\partial p_x \partial p_z} \\ \dfrac{\partial^2 E}{\partial p_x \partial p_z} & \dfrac{\partial^2 E}{\partial p_y \partial p_z} & \dfrac{\partial^2 E}{\partial p_z^2} \end{bmatrix} = \begin{bmatrix} m_{xx}^{-1} & m_{xy}^{-1} & m_{xz}^{-1} \\ m_{yx}^{-1} & m_{yy}^{-1} & m_{yz}^{-1} \\ m_{zx}^{-1} & m_{zy}^{-1} & m_{zz}^{-1} \end{bmatrix}. \qquad (4.42)$$

The tensor in Equation 4.42 is called inverse effective mass tensor.

4.6 Spin-Orbit Interaction

4.6.1 Spin

Otto Stern and Walther Gerlach showed in 1922 that a beam of silver atoms directed through an inhomogeneous magnetic field would be forced into two beams [40]. This was consistent with the prediction of an intrinsic angular momentum and a magnetic moment by individual electrons. Classically this can be explained if the electron were a spinning ball of charge, and this property was called electron spin. This experiment confirmed the quantization of the electron spin into two orientations and made a major contribution to the development of the quantum theory of the atom.

The Schrödinger equation for a hydrogen atom is written as

$$\left(\frac{\mathbf{p}^2}{2m_0} + U(\mathbf{r}) \right) \Psi = E\Psi, \qquad (4.43)$$

where $\mathcal{H} = \dfrac{\mathbf{p}^2}{2m} + U$ is the Hamiltonian, $\mathbf{p} = -i\hbar\nabla$ is the momentum operator, $U(\mathbf{r}) = -|e|^2/r$ is the potential energy, m_0 is the electron mass, $|e|$ is the electron charge, $\Psi(\mathbf{r})$ is the wave function (the square of the wave function determines probability to find the

electron in the volume dV), E is the electron energy. The solution of Equation 4.43 leads to three integer quantum numbers appear - n, l, m_l. These numbers determine the eigenfunction for Equation 4.43 that describes the probability for an electron position on atom. By taking into account the spin properties of the electron the fourth quantum number m_s appears. The spin magnetic quantum number m_s characterizes the spin angular momentum of the electron projection. In experiments it was shown that the electrons' spin can have only two opposite projections on a fixed axis. For the electron, m_s can have only two values $+1/2$ and $-1/2$. Usually this axis is chosen as Z-axis. One of the spin orientations is parallel to the Z-axis and another is antiparallel to the chosen axis. Thus, the two spin states are postulated as $|\uparrow\rangle$ and $|\downarrow\rangle$. For the spin the following orthogonal eigenstates are introduced

$$|\uparrow\rangle \rightarrow \begin{pmatrix} 1 \\ 0 \end{pmatrix}, \tag{4.44}$$

$$|\downarrow\rangle \rightarrow \begin{pmatrix} 0 \\ 1 \end{pmatrix}. \tag{4.45}$$

The spin operator $\mathbf{s} = \dfrac{1}{2}\left(x\sigma_x + y\sigma_y + z\sigma_z\right)$ is described by the following Pauli matrices

$$\sigma_x = \begin{pmatrix} 0 & 1 \\ 1 & 0 \end{pmatrix}, \tag{4.46}$$

$$\sigma_y = \begin{pmatrix} 0 & -i \\ i & 0 \end{pmatrix}, \tag{4.47}$$

$$\sigma_z = \begin{pmatrix} 1 & 0 \\ 0 & -1 \end{pmatrix}. \tag{4.48}$$

4.6.2 Spin-Orbit Hamiltonian

An electron feels an atomic magnetic field while moving in a crystal. This field acts on the spin of the electron. The following Hamiltonian describes this impact

$$\mathcal{H}_{SO} = \frac{1}{4m^2c^2}\mathbf{p}\left[\vec{\sigma} \times (\nabla V(x))\right]. \tag{4.49}$$

Here m is the free electron mass, c is the speed of the light in vacuum, $\vec{\sigma} = (\sigma_x, \sigma_y, \sigma_z)$ is the Pauli matrices, $V(x)$ is the periodic potential, $\mathbf{p}$ is the momentum of the electron, and $\nabla V(x)/|e|$ is the electron felt electric field.
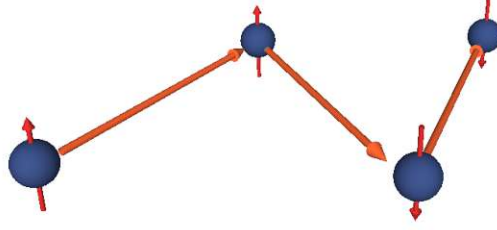
Figure 4.4: Sketch of Elliott-Yafet spin relaxation mechanism.

4.6.3 Spin Relaxation in Semiconductors

Spin relaxation is the process characterizing the non-equilibrium spin vanishing. There are different mechanisms responsible for the spin relaxation: spin-orbital (Elliot-Yafet, D'yakonov-Perel'), electron-hole exchange interaction(Bir-Aronov-Pikus), and hyperfine interaction.

The Elliott-Yafet mechanism was proposed by Elliott [27] and Yafet [130]. The mechanism is important for small gap semiconductors with large spin-orbit splitting [10]. In electronic band structures the spin-up and the spin-down states are mixed by spin-orbit interaction [27]

$$\Psi_{kn\uparrow}(r) = \left(a_{kn}(r)| \uparrow \rangle + b_{kn}(r)| \downarrow \rangle\right) e^{ikr}, \tag{4.50}$$

$$\Psi_{kn\downarrow}(r) = \left(a^*_{-kn}(r)| \downarrow \rangle - b^*_{-kn}(r)| \uparrow \rangle\right) e^{ikr}. \tag{4.51}$$

The spin-up state contains spin-down and the spin-down state also contains a contribution from spin-up. However, the spin mixing is usually very small thus $|b_{kn}| \ll |a_{kn|}$. In the presence of such mixing spin relaxation events can be caused by any spin-independent scattering. In the absence of scattering events the spin state is conserved. This process is called the Elliott process. The Yafet process is due to a spin-orbit interaction in which the spin-orbit coupling of the conduction electrons to the lattice potential can be modulated by lattice vibrations. This leads to an interaction in which the spin of the electron is coupled to the quantum of the lattice vibrations (phonon).

The D'yakonov-Perel' relaxation mechanism [25] is an important spin-flip mechanism for conduction electrons. In semiconductor nanostructures without inversion symmetry there exists an effective spin-orbit contribution equivalent to a **k**-dependent
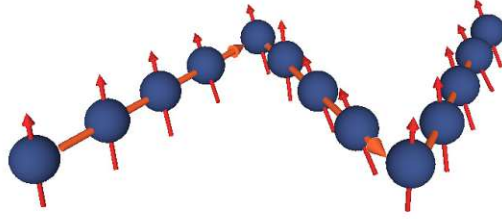
Figure 4.5: Sketch of D'yakonov-Perel' spin relaxation mechanism.

effective magnetic field

$$\mathcal{H}_{SO} = \frac{1}{2}\vec{\Omega}(\mathbf{k})\sigma, \tag{4.52}$$

where $\vec{\Omega}(\mathbf{k})$ is the spin precession frequency. The spin of moving electrons precess due to the effective magnetic field until scattering occurs. After the scattering event the precession starts again but with a different $\vec{\Omega}(\mathbf{k})$. At the scattering event the momentum $\mathbf{k}$ changes randomly, hence spin precesses randomly after the scattering event. This relaxation has a notable feature - stronger momentum scattering leads to a longer spin lifetime. The D'yakonov-Perel' mechanism was found to be dominated in Si quantum well structures but at low temperatures [31, 128].

The Bir-Aronov-Pikus mechanism [8] describes the electron-hole exchange scattering that can lead to the electron spin relaxation in p-type semiconductors. Fluctuations in the effective hole concentration, due to different effective mass, produce a fluctuating effective magnetic field generated by the total spin of holes. This induces a precession of the electron spin around an instantaneous axis, analogously to the D'yakonov-Perel' mechanism.

The forth mechanism responsible for the spin relaxation is hyperfine interaction. Hyperfine interaction is the magnetic interaction between the magnetic moments of electron and nuclei. This interaction is too small to cause effective spin relaxation of free electrons in bulk semiconductor [90, 136].

5 Effective k·p Hamiltonian

In this chapter the effective **k·p** Hamiltonian with shear strain and properly included spin-orbit interaction is introduced. The wave functions and the valley splitting is investigated for different parameters.

5.1 Relaxed Silicon Structure

Silicon has a diamond lattice structure (Figure 5.1). The diamond lattice is of a face centered cubic Bravais lattice which contains two identical atoms per unit cell. The distance between the two atoms is equals to one quarter of the diagonal of the cube. The first Brillouin zone is sketched in Figure 5.2. It has the shape of a truncated octahedron and can be visualized with eight hexagonal faces and six square faces (Figure 5.2). The following symmetry points are shown: Γ the point in the center of the zone (origin of k space), X - the point in the middle of square faces, L - the point in the middle of hexagonal faces, and K - the point in the middle of the edge shared by two adjacent hexagons. The directions are: Δ - the axis connecting the Γ and X
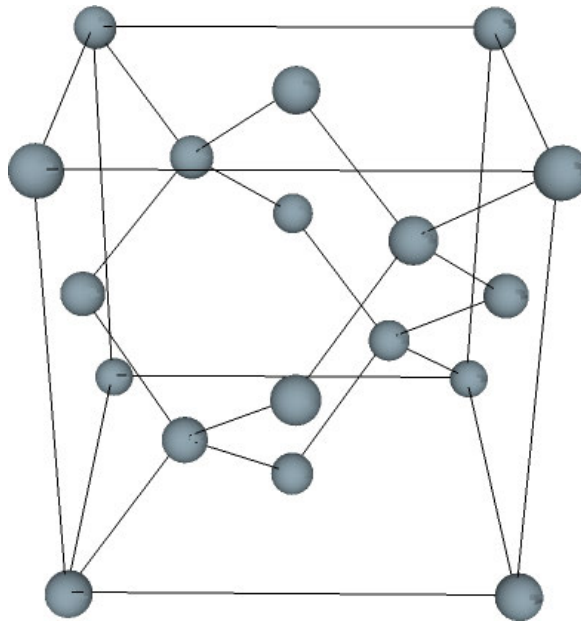
Figure 5.1: Sketch of the diamond crystal lattice.
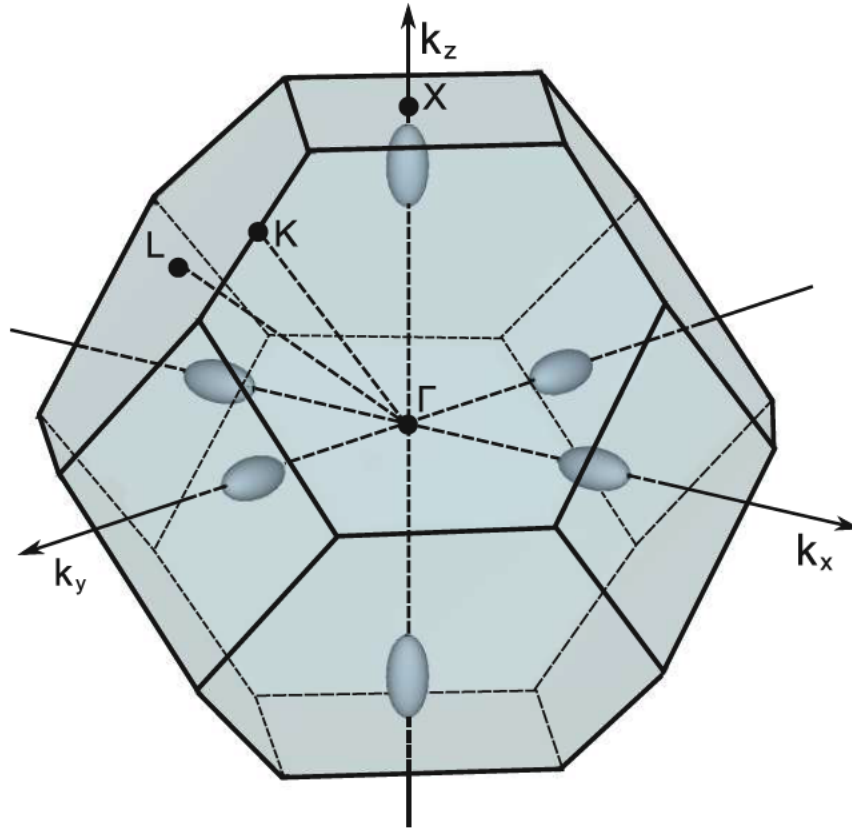
Figure 5.2: Sketch of the first Brillouin zone, the valleys positions and high symmetry points for silicon.

points, Λ - the axis connecting the Γ and L points, and Σ - the axis connecting the Γ and K points. The conduction band minima lie on the six equivalent Δ - lines and occur at about 85% of the way to the zone boundary.

5.2 Two-Band k·p Hamiltonian of [001] Valley at the X-Point Including Spin

For [001] oriented valleys in a (001) silicon film the Hamiltonian is written in the vicinity of the X point along the k_z-axis in the Brillouin zone. The basis is conveniently chosen as $[(X_1, \uparrow) , (X_1, \downarrow) , (X_{2'}, \uparrow) , (X_{2'}, \downarrow)]$, where $\uparrow$ and $\downarrow$ indicate the spin projection at the quantization z-axis, X_1 and $X_{2'}$ are the basis functions corresponding to the two valleys. The effective **k·p** Hamiltonian reads as [87, 106, 111]

$$\mathcal{H} = \begin{bmatrix} H_1 & H_3 \\ H_3^\dagger & H_2 \end{bmatrix},$$

(5.1)

where H_1, H_2, and H_3 are written as

$$H_1 = \begin{bmatrix} \dfrac{\hbar^2 k_z^2}{2m_l} + \dfrac{\hbar^2 \left(k_x^2 + k_y^2\right)}{2m_t} - \dfrac{\hbar^2 k_0 k_z}{m_l} + U(z) & 0 \\ 0 & \dfrac{\hbar^2 k_z^2}{2m_l} + \dfrac{\hbar^2 \left(k_x^2 + k_y^2\right)}{2m_t} - \dfrac{\hbar^2 k_0 k_z}{m_l} + U(z) \end{bmatrix}, \quad (5.2)$$

$$H_2 = \begin{bmatrix} \dfrac{\hbar^2 k_z^2}{2m_l} + \dfrac{\hbar^2 \left(k_x^2 + k_y^2\right)}{2m_t} + \dfrac{\hbar^2 k_0 k_z}{m_l} + U(z) & 0 \\ 0 & \dfrac{\hbar^2 k_z^2}{2m_l} + \dfrac{\hbar^2 \left(k_x^2 + k_y^2\right)}{2m_t} + \dfrac{\hbar^2 k_0 k_z}{m_l} + U(z) \end{bmatrix}, \quad (5.3)$$

$$H_3 = \begin{bmatrix} D\varepsilon_{xy} - \dfrac{\hbar^2 k_x k_y}{M} & (k_y - k_x \mathrm{i})\,\Delta_{SO} \\ (-k_y - k_x \mathrm{i})\,\Delta_{SO} & D\varepsilon_{xy} - \dfrac{\hbar^2 k_x k_y}{M} \end{bmatrix}. \quad (5.4)$$

Here, ε_{xy} denotes the shear strain component, $M^{-1} \approx m_t^{-1} - m_0^{-1}$, D=14eV is the shear strain deformation potential, m_t and m_l are the transversal and the longitudinal silicon effective masses, k_0=0.15×2π/a is the position of the valley minimum relative to the X point in unstrained silicon, and $U(z)$ is the confinement potential.

The spin-orbit term $\tau_y \otimes \Delta_{SO}(k_x \sigma_x - k_y \sigma_y)$ with [70]

$$\Delta_{SO} = \frac{\hbar^2}{2m_0^3 c^2} \left| \sum_n \frac{\langle X_1 | p_j | n \rangle \langle n | [\nabla V \times \mathbf{p}]_j | X_{2'} \rangle}{E_n - E_X} \right|, \quad (5.5)$$

couples the states with the opposite spin projections from the opposite valleys. In the perturbation theory expression for Δ_{SO} E_n is the energy of the n-th band at the X point, E_X is the energy of the two lowest conduction bands X_1 and $X_{2'}$ degenerate at the X point, $\mathbf{p}$ is the momentum operator, V is the bulk crystal potential, σ_x, σ_y, and σ_z are the spin Pauli matrices, τ_y is the y-Pauli matrix in the valley degree of freedom and c is the speed of light.

In the presence of strain and confinement the four-fold degeneracy of the n-th unprimed subband is partly lifted by forming an $n+$ and $n-$ subladder (the valley splitting), however, the degeneracy of the eigenstates with the opposite spin projections $n\pm \Uparrow\rangle$ and $n\pm \Downarrow\rangle$ within each subladder is preserved. $|\Uparrow\rangle$ is the superposition of the spin-up and the spin-down eigenstates, $|\Downarrow\rangle$ is the superposition of the spin-down and the spin-up eigenstates.

The degenerate states are chosen to satisfy

$$\langle \Uparrow n \pm |f| n\pm \Downarrow\rangle = 0, \quad (5.6)$$

with the operator defined as [137]

$$f = \cos(\theta)\,\sigma_z + \sin(\theta)\left(\cos(\varphi)\,\sigma_x + \sin(\varphi)\,\sigma_y\right), \quad (5.7)$$
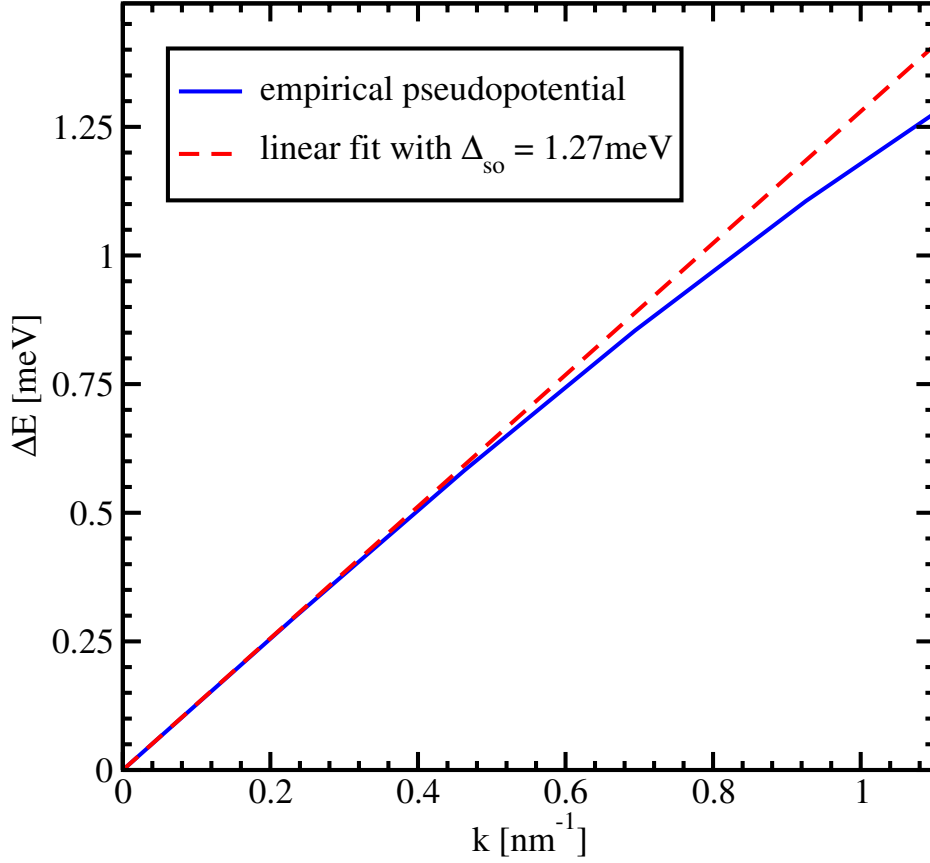
Figure 5.3: Empirical pseudopotential calculations of the spin-orbit interaction strength by evaluating the gap opening at the X-point between X_1 and $X_{2'}$ for finite k_x.

where θ is the polar φ and is the azimuth angle defining the orientation of the injected spin. In general, the expectation value of the operator f computed between the spin up and down states from different subladders is non-zero, when the effective magnetic field direction due to the spin-orbit interaction is different from the injected spin quantization axis

$$\bar{f} = \langle \Uparrow n \pm |f| n \mp \Downarrow \rangle \neq 0. \tag{5.8}$$

For a zero value of the confinement potential the energy dispersion of the lowest conduction bands is given by

$$E(k) = \frac{\hbar^2 k_z^2}{2m_l} + \frac{\hbar^2 \left(k_x^2 + k_y^2 \right)}{2m_t}$$
$$\pm \sqrt{\left(\frac{\hbar^2 k_z k_0}{m_l} \right)^2 + \left(D\varepsilon_{xy} - \frac{\hbar^2 k_x k_y}{M} \right)^2 + \Delta_{SO}^2 \left(k_x^2 + k_y^2 \right)}. \tag{5.9}$$

This expression generalizes the corresponding dispersion relation from [70] by including shear strain.

In order to evaluate the strength Δ_{SO} of the effective spin-orbit interaction Equation 5.9 is used. Close to the X point in the unstrained sample the gap between the X_1 and $X_{2'}$ conduction bands can be opened by Δ_{SO} alone if one evaluates the dispersion for $k_x \neq 0$ but $k_y = k_z = 0$. The band splitting along the x-axis is then equal to the $2\left|\Delta_{SO}k_x\right|$. The empirical pseudopotential method (EPM) [111], [117] is used to obtain the splitting numerically. The result is shown in Figure 5.3. The dependence on k_x is indeed linear at small values of k_x. By fitting this dependence with a linear function (shown in Figure 5.3) at small k_x the value $\Delta_{SO} = 1.27\mathrm{meVnm}$ is found which is close to the one reported in [70].

5.3 Analytical Wave Function Calculation

To find the wave functions in a analytical manner, the Hamiltonian (5.1) is rotated by means of the following unitary transformation. The four basis functions $X_{1\uparrow}, X_{1\downarrow}, X_{2'\uparrow}, X_{2'\downarrow}$ for the two [001] valleys with spin up, spin down are transformed by (5.10-5.17) with $\tan\left(\Theta\right) = \dfrac{\Delta_{SO}\sqrt{k_x^2 + k_y^2}}{D\varepsilon_{xy} - \dfrac{\hbar^2 k_x k_y}{M}}$. The transformation decouples the spins with opposite direction in different valleys.

$$\Psi_1 = \frac{1}{2}\left[\left(X_{1\uparrow} + X'_{2\uparrow}\right) + \left(X_{1\downarrow} + X'_{2\downarrow}\right)\frac{k_x - ik_y}{\sqrt{k_x^2 + k_y^2}}\right], \qquad (5.10)$$

$$\Psi_2 = \frac{1}{2}\left[\left(X_{1\uparrow} + X'_{2\uparrow}\right) - \left(X_{1\downarrow} + X'_{2\downarrow}\right)\frac{k_x - ik_y}{\sqrt{k_x^2 + k_y^2}}\right], \qquad (5.11)$$

$$\Psi_3 = \frac{1}{2}\left[\left(X_{1\uparrow} - X'_{2\uparrow}\right) + \left(X_{1\downarrow} - X'_{2\downarrow}\right)\frac{k_x - ik_y}{\sqrt{k_x^2 + k_y^2}}\right], \qquad (5.12)$$

$$\Psi_4 = \frac{1}{2}\left[\left(X_{1\uparrow} - X'_{2\uparrow}\right) - \left(X_{1\downarrow} - X'_{2\downarrow}\right)\frac{k_x - ik_y}{\sqrt{k_x^2 + k_y^2}}\right], \qquad (5.13)$$

$$X_1 = \Psi_1 \cos\left(\frac{\Theta}{2}\right) - i\Psi_3 \sin\left(\frac{\Theta}{2}\right), \qquad (5.14)$$

$$X_2 = \Psi_2 \cos\left(\frac{\Theta}{2}\right) + i\Psi_4 \sin\left(\frac{\Theta}{2}\right), \qquad (5.15)$$

$$X_3 = \Psi_3 \cos\left(\frac{\Theta}{2}\right) - i\Psi_1 \sin\left(\frac{\Theta}{2}\right), \tag{5.16}$$

$$X_4 = \Psi_4 \cos\left(\frac{\Theta}{2}\right) + i\Psi_2 \sin\left(\frac{\Theta}{2}\right). \tag{5.17}$$

The Hamiltonian (5.1) can now be cast into a form in which spins with opposite orientation in different valleys are independent

$$\mathcal{H} = \begin{bmatrix} \mathcal{H}_1 & \mathcal{H}_3 \\ \mathcal{H}_3 & \mathcal{H}_2 \end{bmatrix}, \tag{5.18}$$

$\mathcal{H}_1$, $\mathcal{H}_2$, and $\mathcal{H}_3$ are written as

$$\mathcal{H}_1 = \begin{bmatrix} \dfrac{\hbar^2 k_z}{2m_l} + \dfrac{\hbar^2 \left(k_x^2 + k_y^2\right)}{2m_t} - \delta + U(z) & 0 \\ 0 & \dfrac{\hbar^2 k_z}{2m_l} + \dfrac{\hbar^2 \left(k_x^2 + k_y^2\right)}{2m_t} - \delta + U(z) \end{bmatrix} \tag{5.19}$$

$$\mathcal{H}_2 = \begin{bmatrix} \dfrac{\hbar^2 k_z}{2m_l} + \dfrac{\hbar^2 \left(k_x^2 + k_y^2\right)}{2m_t} + \delta + U(z) & 0 \\ 0 & \dfrac{\hbar^2 k_z}{2m_l} + \dfrac{\hbar^2 \left(k_x^2 + k_y^2\right)}{2m_t} + \delta + U(z) \end{bmatrix} \tag{5.20}$$

$$\mathcal{H}_3 = \begin{bmatrix} \dfrac{\hbar^2 k_0 k_z}{m_l} & 0 \\ 0 & \dfrac{\hbar^2 k_0 k_z}{m_l} \end{bmatrix} \tag{5.21}$$

with $\delta = \sqrt{\left(D\varepsilon_{xy} - \dfrac{\hbar^2 k_x k_y}{M}\right)^2 + \Delta_{SO}^2 \left(k_x^2 + k_y^2\right)}$.

Following [111] the wave functions are found analytically in the same manner as for the two band **k·p** Hamiltonian written in the vicinity of the X-point of the Brillouin zone for silicon films under uniaxial strain.

5.4 Validation of the Analytical Solution

In order to validate the Hamiltonian the analytical results are compared to other approaches. For instance, Figure 5.4 shows the splitting between the lowest unprimed electron subbands as a function of the wave vector **k** taken along [110] and [-110] directions in a confined system. The results computed by the linear combination of
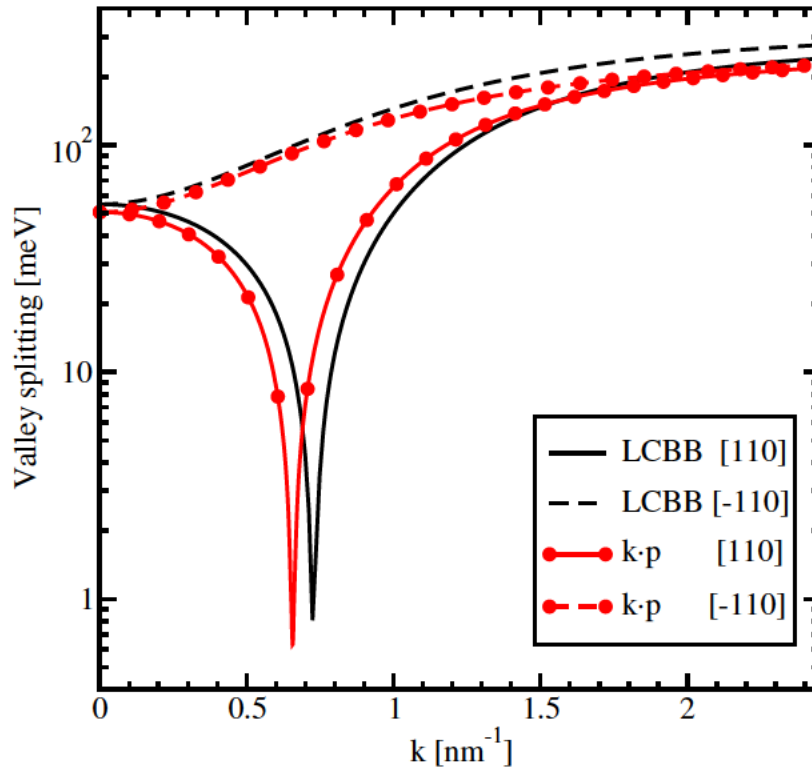
Figure 5.4: Dependence of the valley splitting on the wave vector **k**, for a film of 2nm thickness, and a shear strain value of 0.5%.
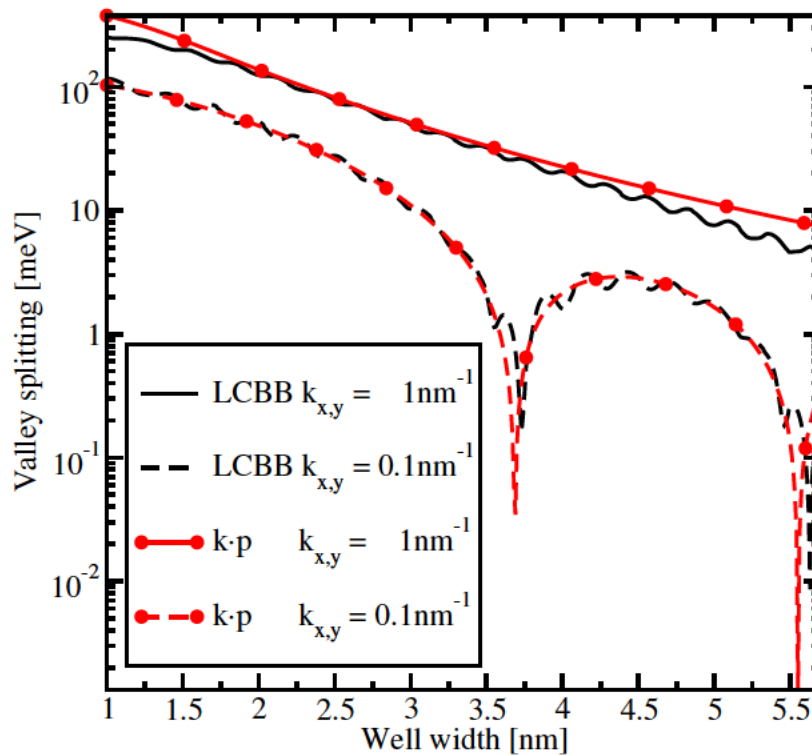
Figure 5.5: Splitting between the two lowest electron subbands as a function of well width and a shear strain value of 0.5%.
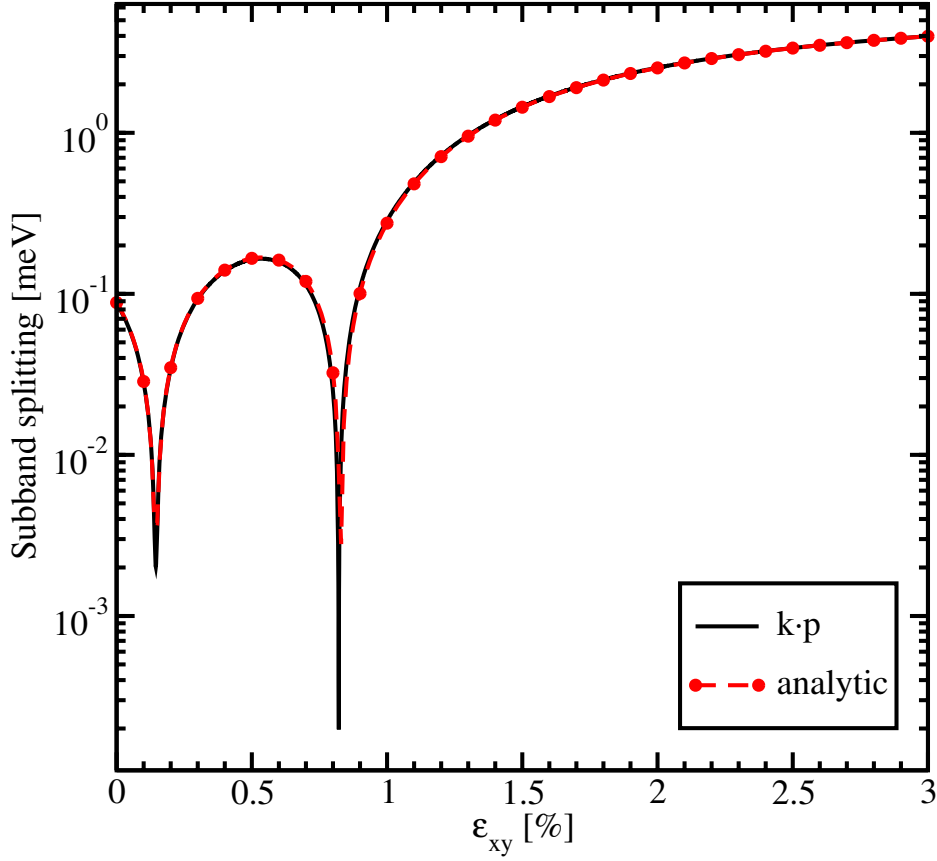
Figure 5.6: Subband splitting for a film thickness of 4nm for k_x=0.25nm^{-1} and k_y=0.25nm^{-1} as a function of shear strain.

bulk bands (LCBB) method [30] and the perturbative **k·p** approach are shown. For the [-110] direction the dependence is smooth without any sharp features. For the curves calculated along [110] direction a sharp decrease of the splitting is observed. Although the positions of the minima calculated by the **k·p** and by the LCBB methods do not match completely, the agreement is quite spectacular.

The valley splitting in a quantum well as a function of the well width is shown in Figure 5.5. The in-plane wave vector **k** along the [110] direction is chosen. The results for the wave vectors with the components k_x=0.1nm^{-1}, k_y=0.1nm^{-1} and k_x=1nm^{-1}, k_y=1nm^{-1} are shown for convenience. As predicted [38, 118], the valley splitting develops sharp minima for small values of **k**. For larger **k** the valley splitting computed with the **k·p** method decays monotonically when the film thickness is increased. The results obtained by the LCBB methods are in good agreement with those obtained by the **k·p** approach.

Finally, the analytical solution is compared to the numerical [7]. Figure 5.6 demonstrates an excellent agreement between the analytical and the numerically obtained results for a silicon film of 4nm thickness for k_x=0.25nm^{-1} and k_y=0.25nm^{-1}. For the
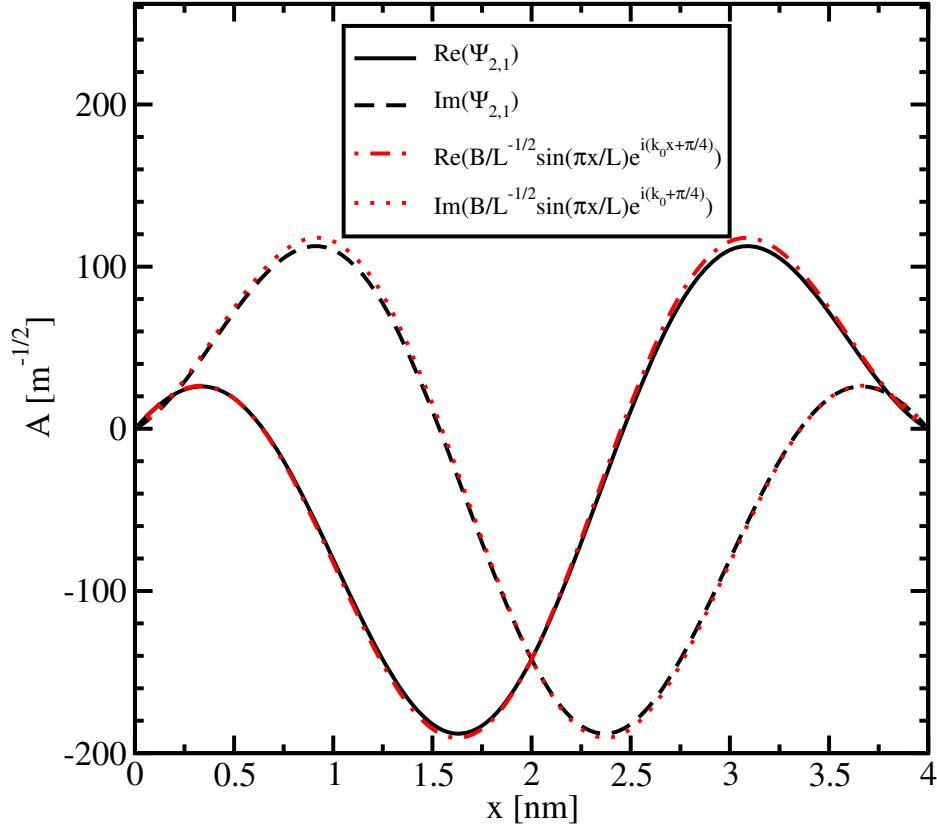
Figure 5.7: Compare calculated wave functions with envelope function.

numerical calculations a barrier of 10eV height has been assumed.

5.5 Numerical Wave Functions Calculation

The eigenvector for the Hamiltonian (Equation 5.18) for the lowest subband is a four-component vector. For $\mathbf{k} = 0$ spin-up and spin-down states are eigenstates, i.e. spin-up wave-function does not contain any spin-down states and vice versa. For $k_x \neq 0$ or $k_y \neq 0$ the spin-orbit term does not vanish, thus, two eigenstates are mixed. Therefore, the four-component wave function for spin-up electron contains a finite but small part of the spin-down state. Figure 5.7 shows the small spin-down component of the spin-up wave-function in a valley along [001] direction. The wave functions is quite accurately described by its envelope function times the phase factor $e^{ik_0z+\phi}$, where ϕ is the wave functions phase.

Figure 5.8 and Figure 5.9 show the majority and the minority components of the spin-up wave function for different shear strain values. The absolute value of the small part of the wave function shown in Figure 5.8 significantly decreases with strain applied. The derivative at the interface also becomes smaller for the strain value of 1%
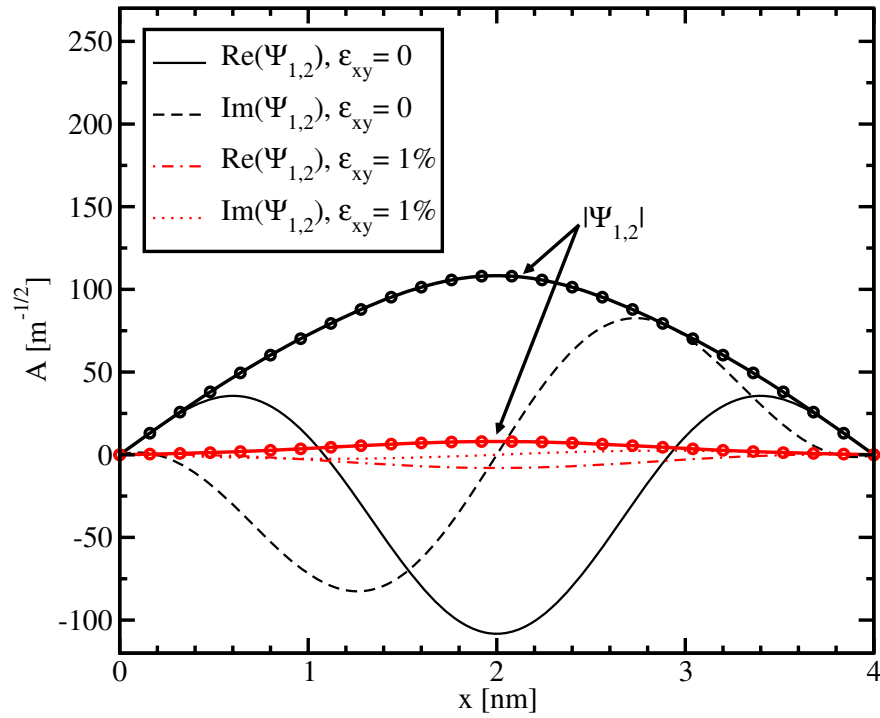
Figure 5.8: Wave functions for different shear strain values. The small part of the four-component wave function is shown.
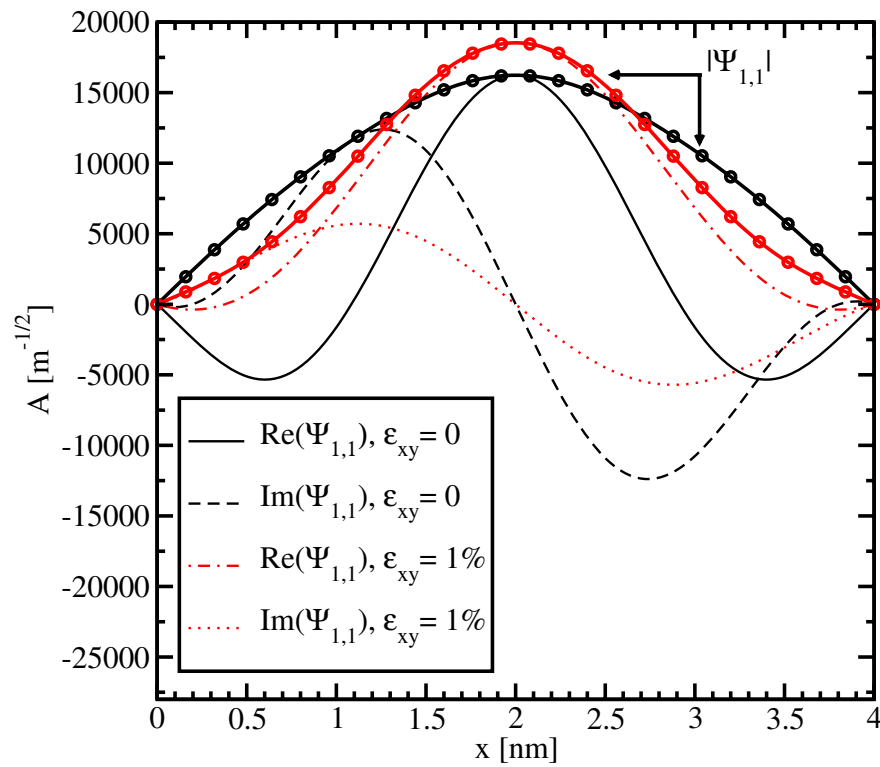
Figure 5.9: Wave functions for different shear strain values. The big part of the four-component wave function is shown.
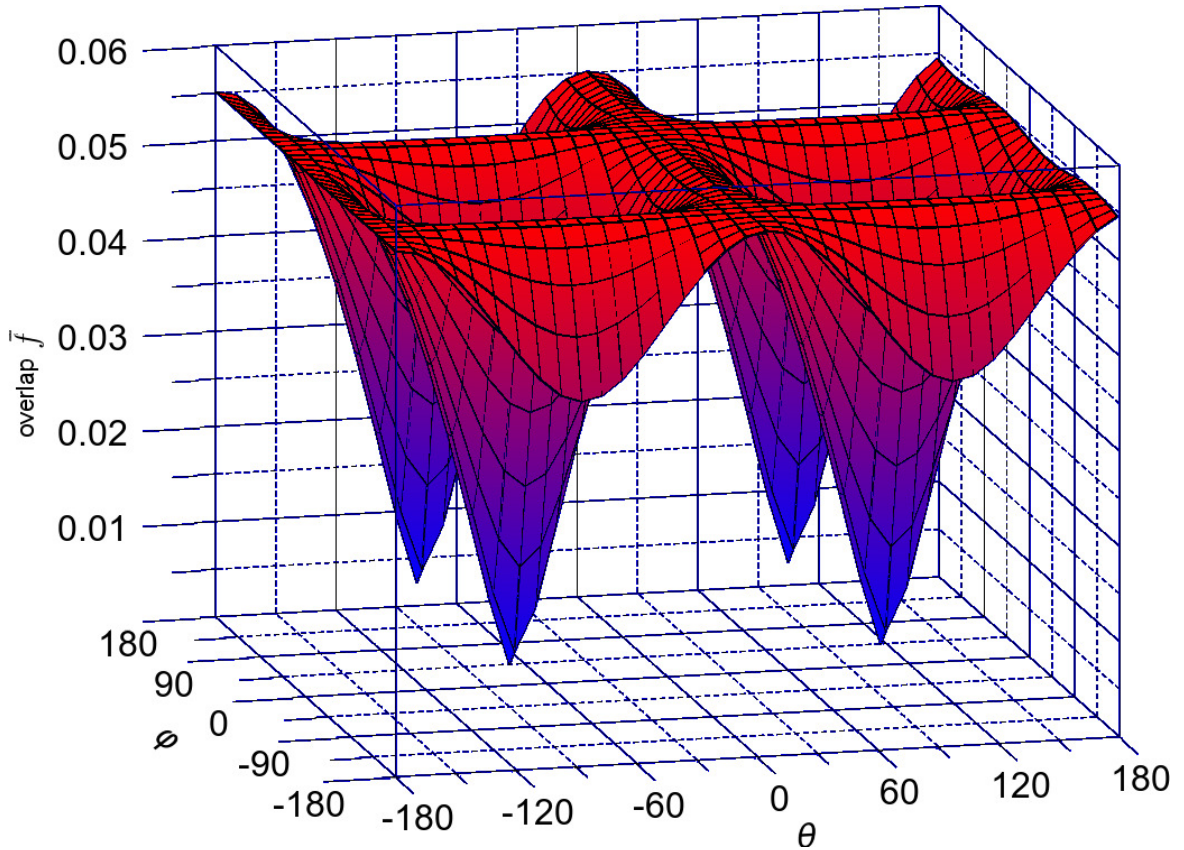
Figure 5.10: Dependence of the overlap of wave functions between the two lowest conduction subbands on the spin injection direction for k_x=0.1nm^{-1}, k_y=0.1nm^{-1}, the shear strain value is 0%.

compared to the unstrained wave function. The absolute value of the big component of the wave function shown in Figure 5.9 changes insignificantly.

The decrease of the spin-down component in the spin-up wave function leads to a decrease of the Elliott contribution (Equation 4.50) to the spin relaxation.

5.6 Overlap Calculation

Figure 5.10, Figure 5.11, and Figure 5.12 show the dependence of $\bar{f}$ (Equation 5.8) on the orientation of the injected spin for $k_x = 0.1$nm^{-1}, $k_y = 0.1$nm^{-1} for different values of shear strain. The absolute value of the overlap $\bar{f}$ characterizes the strength of the spin up/down states mixing caused by the spin-orbit interaction. The spin mixing significantly decreases with shear strain increased in the whole range of spin orientations.
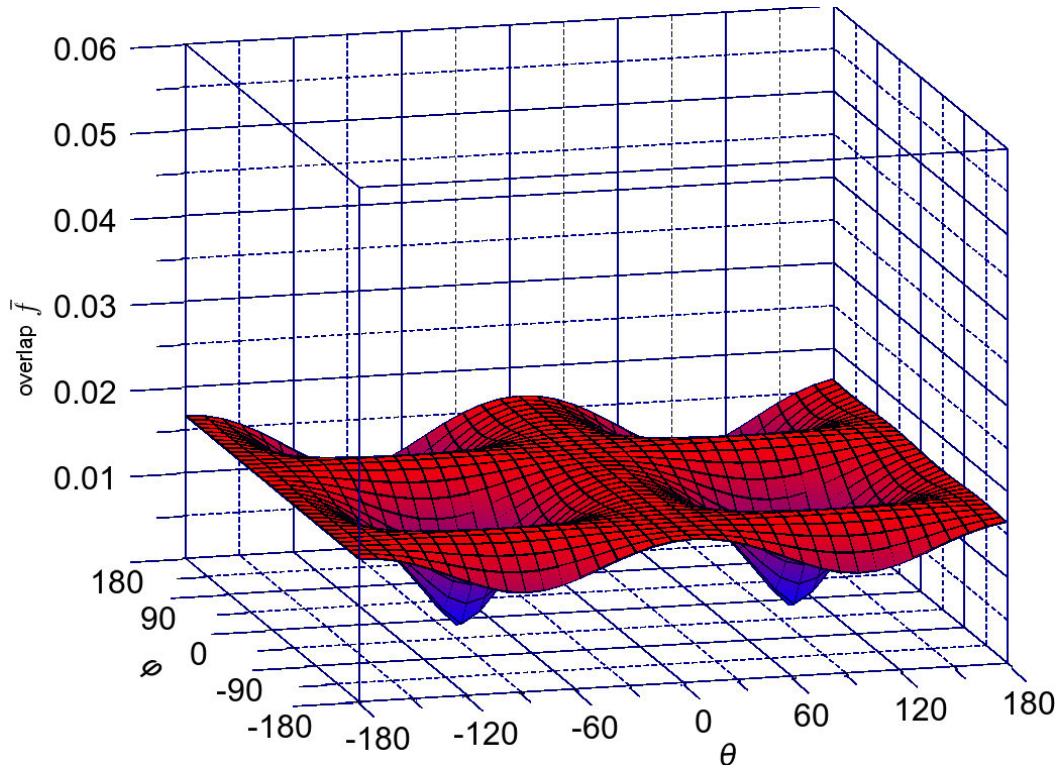
Figure 5.11: Same as Figure 5.10 for the shear strain 0.1%
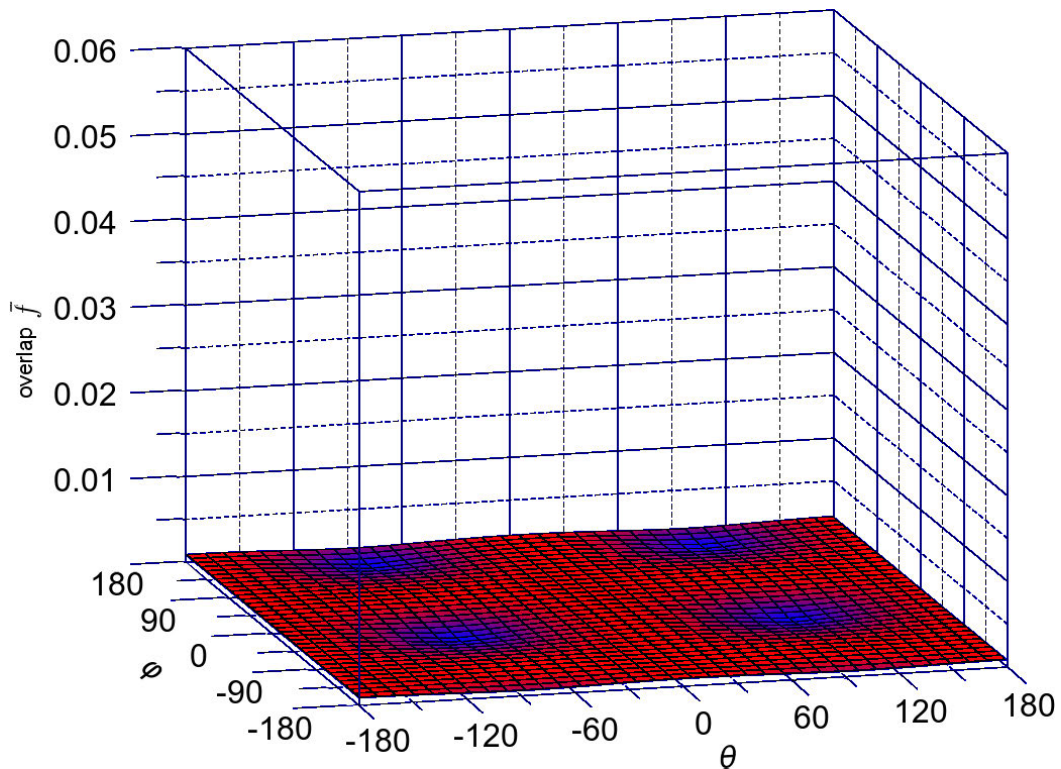
Figure 5.12: Same as Figure 5.10 for the shear strain 1%
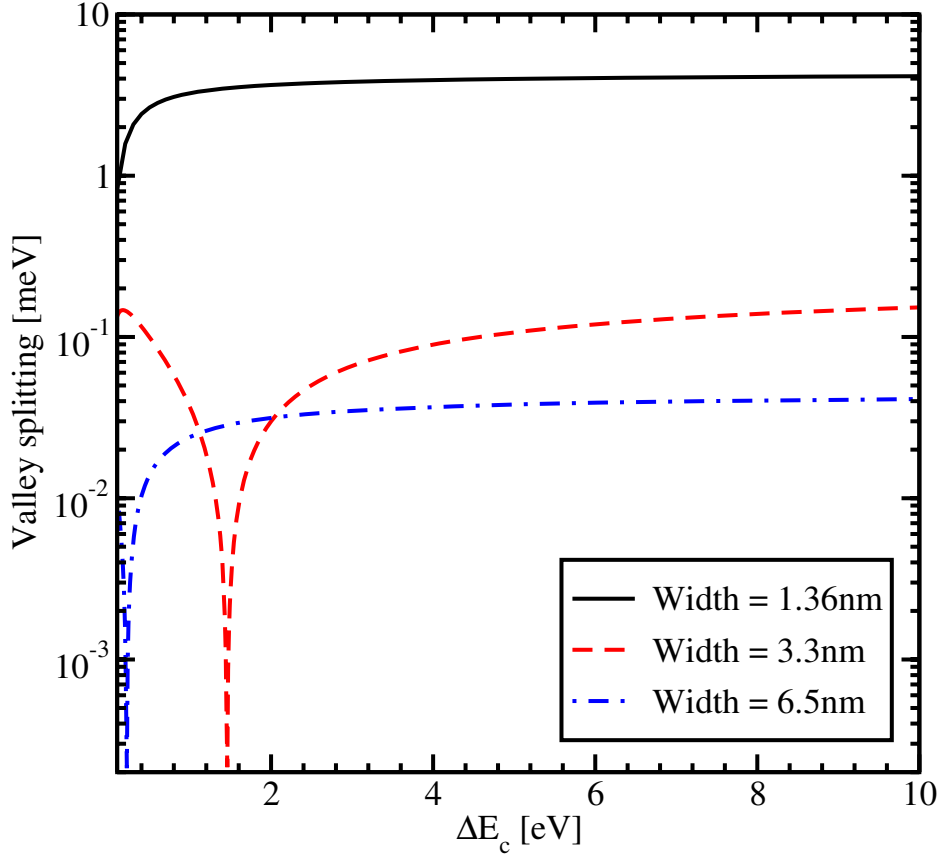
Figure 5.13: Splitting between the lowest unprimed electron subbands as a function of the conduction band offset at the interface for different thicknesses for $\varepsilon_{xy}=0$, $k_x=0.1\text{nm}^{-1}$ and $k_y=0.1\text{nm}^{-1}$.

5.7 Valley Splitting

In this section the value of the energy splitting between the subbands with the same quantum number n but from different subsets $n+$ and $n-$ as a function of the conduction band offset at the interface and for different values of the quantum well thickness is investigated. It is assumed that the spin is injected along the z-direction and the components of the wave vector **k** are $k_x=0.1\text{nm}^{-1}$ and $k_y=0.1\text{nm}^{-1}$. Figure 5.13 shows the subband splitting for three different values of the film width, namely 1.36nm, 3.3nm, and 6.5nm.

The Schrödinger differential equation, with the confinement potential appropriately added in the Hamiltonian (5.1), is solved using efficient numerical algorithms available through the Vienna Schrödinger-Poisson framework (VSP) [7, 62].

Figure 5.13 demonstrates a complicated behavior which strongly depends on the thickness value, in contrast to the valley splitting theory in SiGe/Si/SiGe quantum
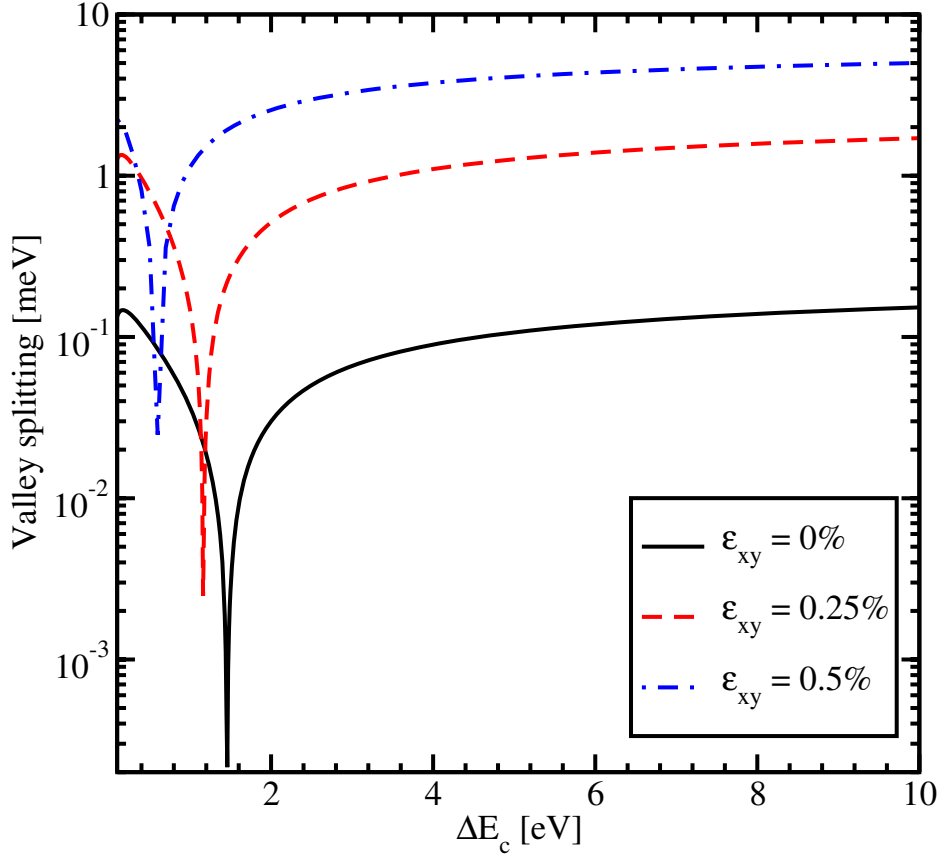
Figure 5.14: Valley splitting as a function of the conduction band offset for a film thickness of 3.3nm for k_x=0.1nm^{-1} and k_y=0.1nm^{-1} and different shear strain values.

wells [38], which predicts that in the case of a symmetric square well without an electric field the valley splitting is simply inversely proportional to the conduction band offset ΔE_C at the interfaces. Figure 5.13 shows that for the quantum well of 1.36nm width the splitting first increases but later saturates. For the quantum well of 3.3nm width a significant reduction of the valley splitting around the conduction band offset value 1.5eV is observed. A further increase of the conduction band offset leads to an increase of the subband splitting value. For the quantum well of 3.3nm thickness the valley splitting saturates at about 0.17meV.

For the quantum well of 6.5nm width a significant reduction of the valley splitting is observed around the conduction band offset value of 0.2eV. The subband splitting saturates at a value of 0.04meV. Although for the values of the conduction band offset smaller than 4eV the valley splitting depends on ΔE_C, for larger values of the conduction band offset it saturates.

The valley splitting dependence on strain as a function of the conduction band offset for the film of 3.3nm thickness is shown in Figure 5.14. Without shear strain the valley splitting is significantly reduced around the conduction band offset value of 1.5eV.
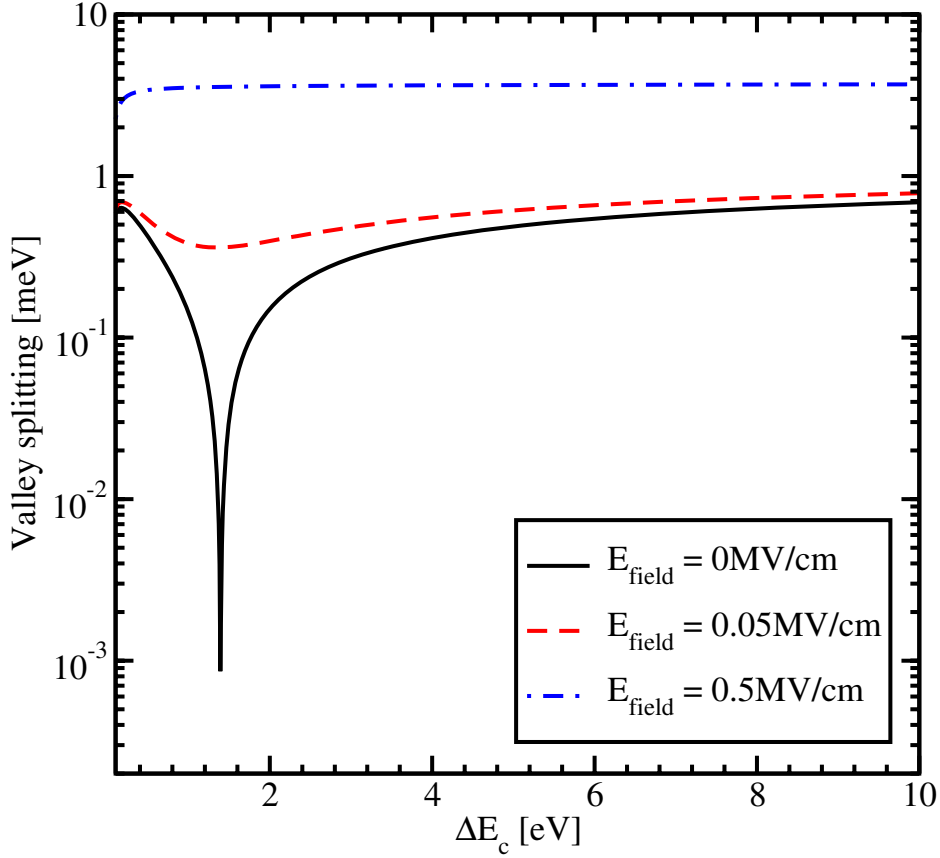
Figure 5.15: Dependence of the valley splitting on the conduction band offset at the inter-
face for different values of the electric field, the shear strain value is 0.125%,
and the quantum well width is 3.3nm.

For the shear strain value of 0.25% and 0.5% the sharp reduction of the conduction
subbands splitting shifts to a smaller value of ΔE_C. However, the region of significant
reduction is preserved even for the large shear strain value of 0.5%. The value of
the valley splitting at saturation for large shear strain is considerably enhanced as
compared to the unstrained case.

The influence of the effective electric field on the region of sharp splitting reduction is
demonstrated in Figure 5.15. With the electric field applied the reduction in the region
of interest around the conduction band offset value 1.5eV becomes smoother. However,
for values of the conduction band offset smaller than 1.5eV the reduction of the valley
splitting is still observed. For the values larger than 1.5eV the subband splitting
slightly increases and then saturates. For the electric field value of 0.05MV/cm the
saturation value of the valley splitting is almost equal to the saturated valley splitting
value without electric field. For the stronger electric field of 0.5MV/cm the valley
splitting reduction vanishes completely and the splitting becomes almost independent
of the conduction band offset.
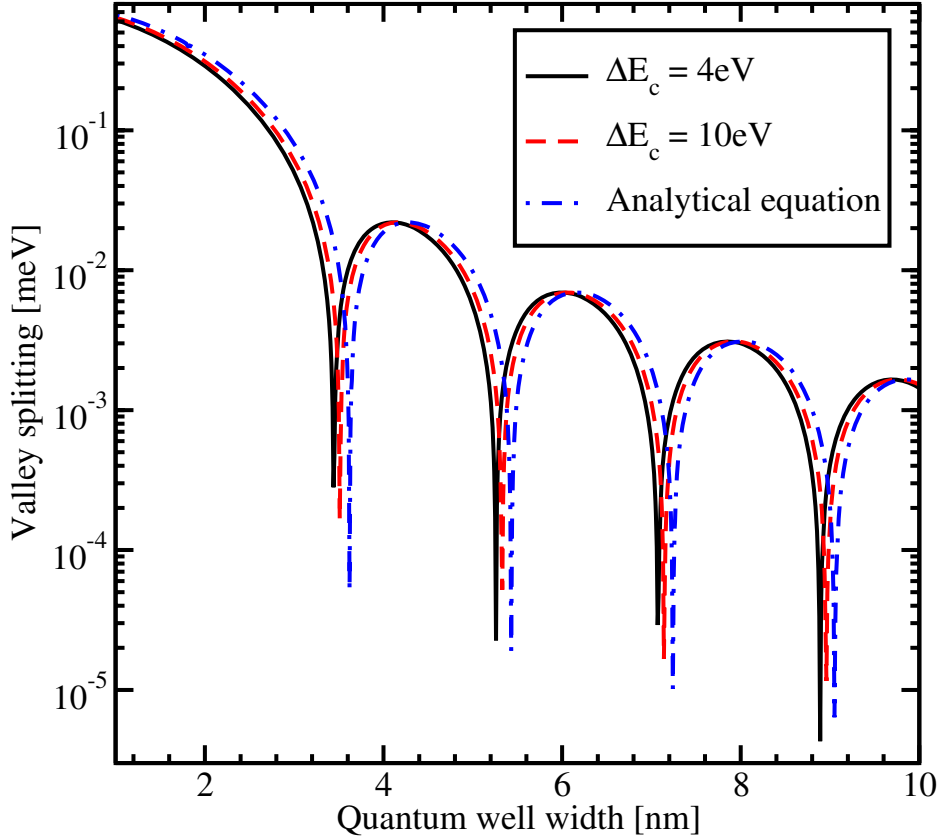
Figure 5.16: Splitting of the lowest unprimed electron subbands as a function of the silicon film thickness for several values of the band offset at the interface, the shear strain value is 0.05%, k_x=0.1nm^{-1}, k_y=0.2nm^{-1}.

The splitting of the lowest unprimed electron subbands as a function of the silicon film thickness for several values of the conduction band offset at the interfaces is shown in Figure 5.16. The valley splitting oscillates with increasing film thickness. According to the theory [9], the equation for the valley splitting in an infinite potential square well is generalized including the spin-orbit coupling as [111, 124]

$$\Delta E_C = \frac{2y_n^2 B}{k_0 t \sqrt{\left(1 - y_n^2 - \eta^2\right)\left(1 - y_n^2\right)}} \times \left| \sin\left(\sqrt{\frac{1 - y_n^2 - \eta^2}{1 - y_n^2}} k_0 t\right) \right|, \qquad (5.22)$$

with y_n, η, and B defined as

$$y_n = \frac{\pi n}{k_0 t}, \qquad (5.23)$$

$$\eta = \frac{m_l B}{k_0^2 \hbar^2} \qquad (5.24)$$

34
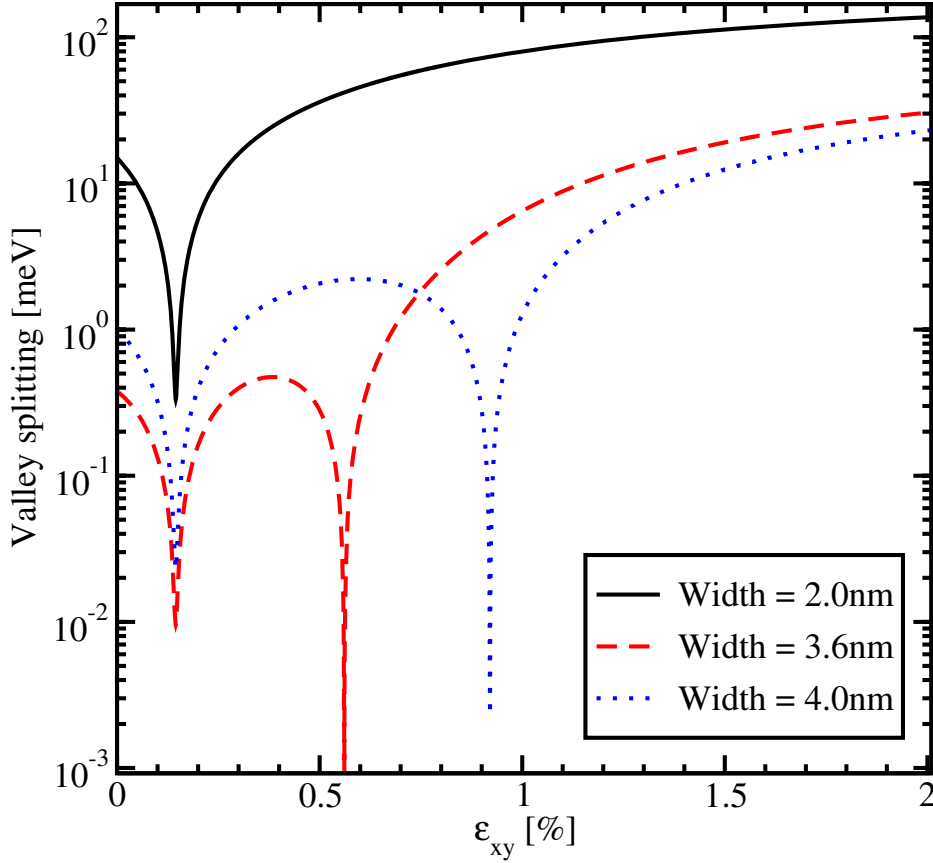
Figure 5.17: Intervalley splitting as a function of shear strain for different values of the well width for k_x=0.25nm^{-1} and k_y=0.25nm^{-1}.

$$B = \sqrt{\Delta_{SO}^2 \left(k_x^2 + k_y^2\right) + \left(D\varepsilon_{xy} - \frac{\hbar^2 k_x k_y}{M}\right)^2}. \tag{5.25}$$

Here t is the film thickness. As it was shown earlier the conduction band value of 4eV provides a subband splitting value close to the saturated one. Because (5.22) is written for an infinite potential square well, a slight discrepancy is observed between the theoretical curve and the numerically computed curve calculated for the conduction band offset value 4eV in Figure 5.16. A large value of the conduction band offset demonstrates a better agreement between the theory and numerically obtained results.

Following (5.22), the results shown in Figure 5.13 can be understood as a consequence of vanishing of the $\left|\sin\left(\sqrt{\dfrac{1-y_n^2-\eta^2}{1-y_n^2}}k_0 t\right)\right|$ term. Although the conduction band offset is not included explicitly in the equation for the valley splitting, it can be taken
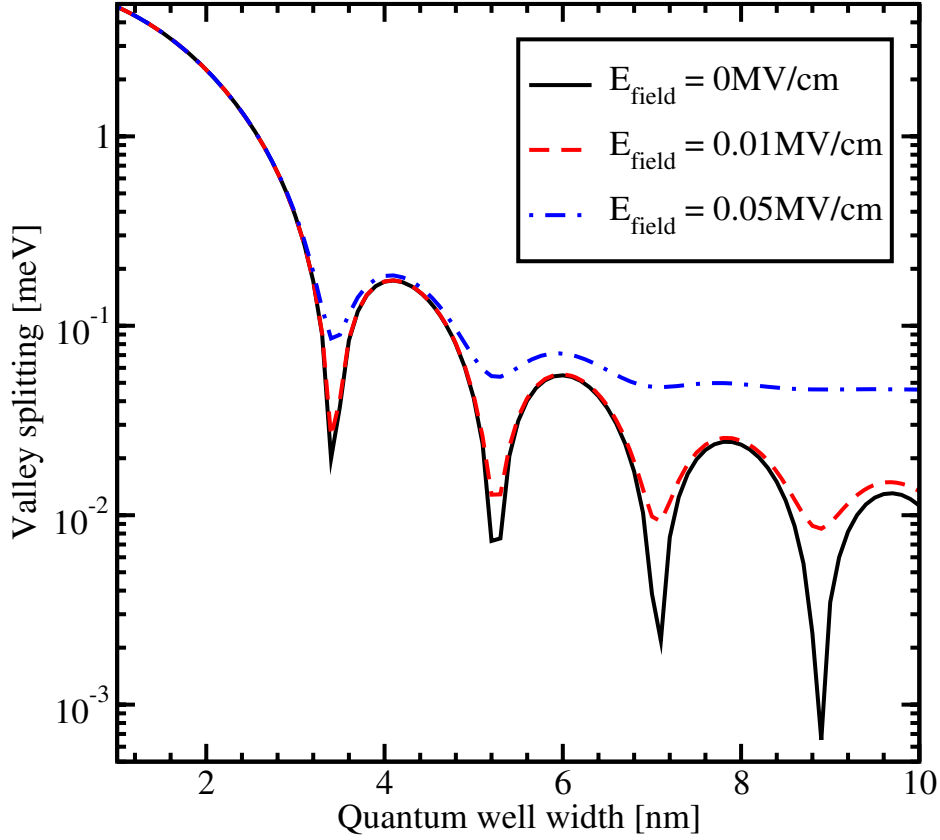
Figure 5.18: Intervalley splitting as a function of shear strain for different values of the well width for $k_x=0.25\text{nm}^{-1}$ and $k_y=0.25\text{nm}^{-1}$.

into account through an effective film width of a finite potential well as [38]

$$t_{eff} = t + \frac{2}{\alpha}, \tag{5.26}$$

$$\alpha = \sqrt{\frac{2m\left(\Delta E_C - E\right)}{\hbar^2}}, \tag{5.27}$$

where E is the subband energy. Thus, increasing the potential barrier height leads to a decrease of the effective film thickness, which then results in the energy splitting dependence shown in Figure 5.13.

The valley splitting reductions shown in Figure 5.14 are also the result of the oscillating sine term in (5.22). The small increase of the shear strain leads to a decrease of the $\sqrt{\dfrac{1-y_n^2-\eta^2}{1-y_n^2}}$ term. This means that in order to obtain zeros of the sine term for larger shear strain values the effective quantum well thickness must be larger. A decrease in the conduction band offset leads precisely to such an increase of the effective thickness. Thus, the results shown in Figure 5.14 are in very good agreement with theory.
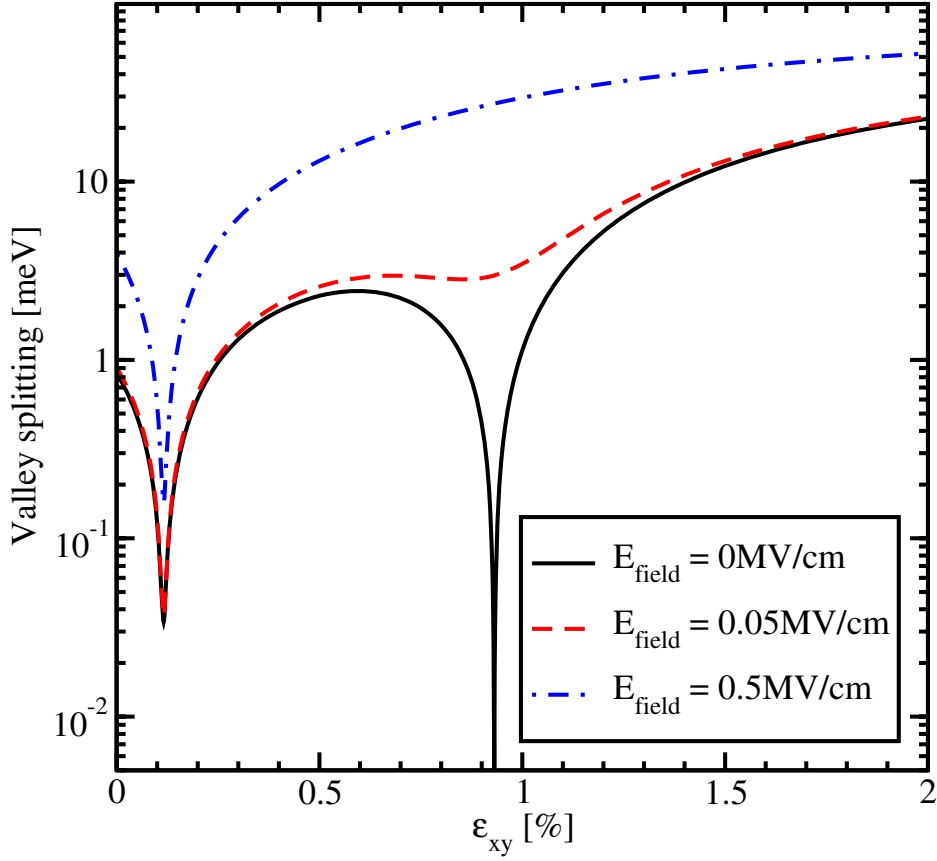
Figure 5.19: Splitting of the lowest conduction subbands as a function of shear strain for different values of the electric field, the quantum well thickness is 4nm, the conduction band offset is 4eV, k_x=0.5nm^{-1}, k_y=0.1nm^{-1}.

Figure 5.17 shows the dependence of the energy splitting on shear strain for the in-plane wave vector **k** components are k_x=0.25nm^{-1} and k_y=0.25nm^{-1}. The significant valley splitting reduction around the strain value 0.145% appears to be independent of the quantum well width. According to (5.22), the valley splitting is also proportional to B, and the valley splitting reduction around the shear strain value 0.145% is caused by vanishing of the $D\varepsilon_{xy} - \dfrac{\hbar^2 k_x k_y}{M}$ contribution. At this minimum the valley splitting is determined by the spin-orbit interaction term alone. The other valley splitting minima in Figure 5.17 depend on the film thickness and are caused by vanishing values of the $\left| \sin\left(\sqrt{\dfrac{1-y_n^2-\eta^2}{1-y_n^2}} k_0 t \right) \right|$ term.

The valley splitting as a function of the quantum well width for different values of the effective electric field is shown in Figure 5.18. Without electric field the valley splitting oscillates as shown in Figure 5.16. With electric field the oscillations are not observed in thicker films. This is due to the fact that in thick films the subband quantization is caused by the electric field. Indeed, for thin structures, when the quantization is

still caused by the second barrier of the quantum well, the shape of the oscillations is similar to that in the absence of an electric field. According to [38], the condition for the independence of the valley splitting from the quantum well width is

$$t^3 > \frac{2\pi^2\hbar^2}{m_l e E_{\text{field}}} \tag{5.28}$$

For an electric field of 0.05MV/cm the quantum well width must be larger than 6.9nm in order to observe the valley splitting independent on the quantum well width. This value is in good agreement with the simulation results shown in Figure 5.18.

Figure 5.19 shows the dependence of the valley splitting on strain. Without electric field the valley splitting reduces significantly around the strain values 0.116% and 0.931% as shown in Figure 5.19. With electric field applied the minimum around the strain value 0.931% becomes smoother, however, for a strain value around 0.116% the sharp reduction of the valley splitting is preserved. For a large electric field the valley splitting reduction around the value 0.931% vanishes completely.

For the strain value 0.116% the sharp reduction of the valley splitting is still preserved at a minimum value only slightly affected by the electric field. As follows from (5.22), for k_x=0.5nm^{-1}, k_y=0.1nm^{-1} the strain value 0.116% causes the term $D\varepsilon_{xy} - \frac{\hbar^2 k_x k_y}{M}$ to vanish and minimizes the valley splitting, in good agreement with the first sharp valley splitting reduction in Figure 5.19. Thus, the valley splitting at this strain value is solely determined by the spin-orbit interaction term. The second minimum in the valley splitting around the strain value 0.931% in Figure 5.19 is caused by vanishing of the $\left|\sin\left(\sqrt{\frac{1-y_n^2-\eta^2}{1-y_n^2}}k_0 t\right)\right|$ term. The effective electric field alters the confinement in the well and is therefore able to completely wash out the minimum in valley splitting due to the sine term. However, in agreement with (5.22), it can only slightly affect the first minimum due to the shear strain dependent contribution, in agreement with Figure 5.19.

6 Momentum Relaxation and Mobility Calculations

6.1 Surface Roughness Limited Scattering Matrix Elements

The interface between Si and SiO_2 plays an important role in determining transport in MOSFETs. Because of non-ideality small perturbations at the interface appear, that lead to field fluctuations and contribute to the scattering. These fluctuations are of several atomic layers size due to processing. Surface roughness scattering is an important relaxation mechanism that is be accounted in MOSFETs simulations. Ultrathin sandwiched structures, where a thin silicon film is placed between two silicon oxides, are more sensitive to surface roughness scattering. Thus, the importance of the surface roughness scattering increases.

Since devices sizes become smaller and the limit of 5nm [39] film thickness after which the surface roughness starts dominating over all other scattering mechanisms achieved in near future, understanding the details of that mechanism is needed.

If one assumes a non-degenerate parabolic band dispersion and an infinite barrier at the silicon-oxide interface the surface roughness scattering matrix elements are proportional to the product of the subband eigenfunction derivatives at the interface [55]

$$M_{i,j}(\mathbf{q}) = \left[\frac{\hbar^2}{2m_l} \frac{d\Psi_i(z)}{dz} \frac{d\Psi_j(z)}{dz} \right]\Bigg|_{z = \pm\frac{t}{2}} \Delta(\mathbf{q}), \tag{6.1}$$

Here, $\Delta(\mathbf{q})$ is the Fourier transform of the random variation of the interface position with respect to the in-plane $\mathbf{r}$ coordinate, $\mathbf{q}$ is the wavevector change due to scattering, $\Psi_{i,j}$ are the subband eigenfunctions in a silicon film, and t is the film thickness. The generalization of this expression to the $\mathbf{k \cdot p}$ theory when the subband functions consist of several components is required. An additional difficulty appears in strained films
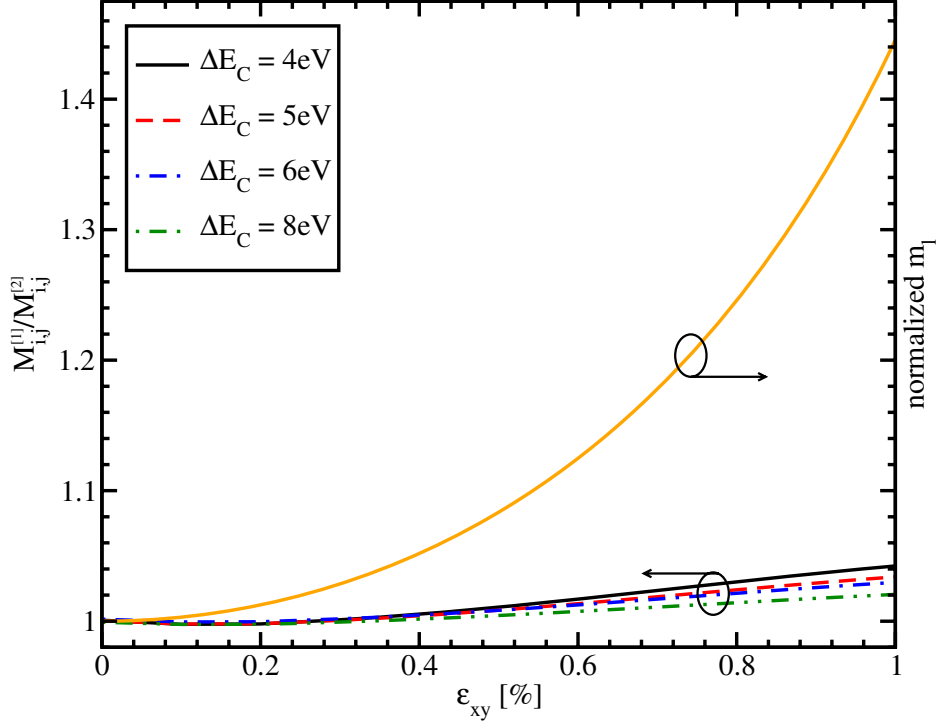
Figure 6.1: Dependence of the ratio of the surface scattering elements calculated by Equation 6.1 $(M_{i,j}^{[1]})$ to the surface scattering elements calculated by Equation 6.3 $(M_{i,j}^{[2]})$ and longitudinal effective mass normalized to its value at zero strain value for the film thickness 2.48nm, for k_x=0.25nm^{-1}, and k_y=0.25nm^{-1}.

where the longitudinal mass is the function of shear strain

$$m_l(\varepsilon_{xy}) = \frac{m_l(\varepsilon_{xy} = 0)}{1 - \left(\dfrac{\dfrac{D\varepsilon_{xy}}{\hbar^2 k_0^2}}{m_l(\varepsilon_{xy} = 0)}\right)^2}. \tag{6.2}$$

In order to resolve the question which mass to use, an alternative approach by Esseni [29] is being followed, where the surface roughness intrasubband scattering matrix elements are

$$M_{i,j}(\mathbf{q}) = [\Delta E_C \left(\Psi_i(z), \Psi_j(z)\right)]\Big|_{z = \pm \frac{t}{2}} \Delta(\mathbf{q}). \tag{6.3}$$

In the limit of $\Delta E_C \to \infty$ Equation 6.1 and Equation 6.3 must produce the same result [29, 55].

Figure 6.1 shows the dependence of the longitudinal effective mass obtained from the ratio of the surface scattering elements calculated with Equation 6.1 and Equation 6.3,
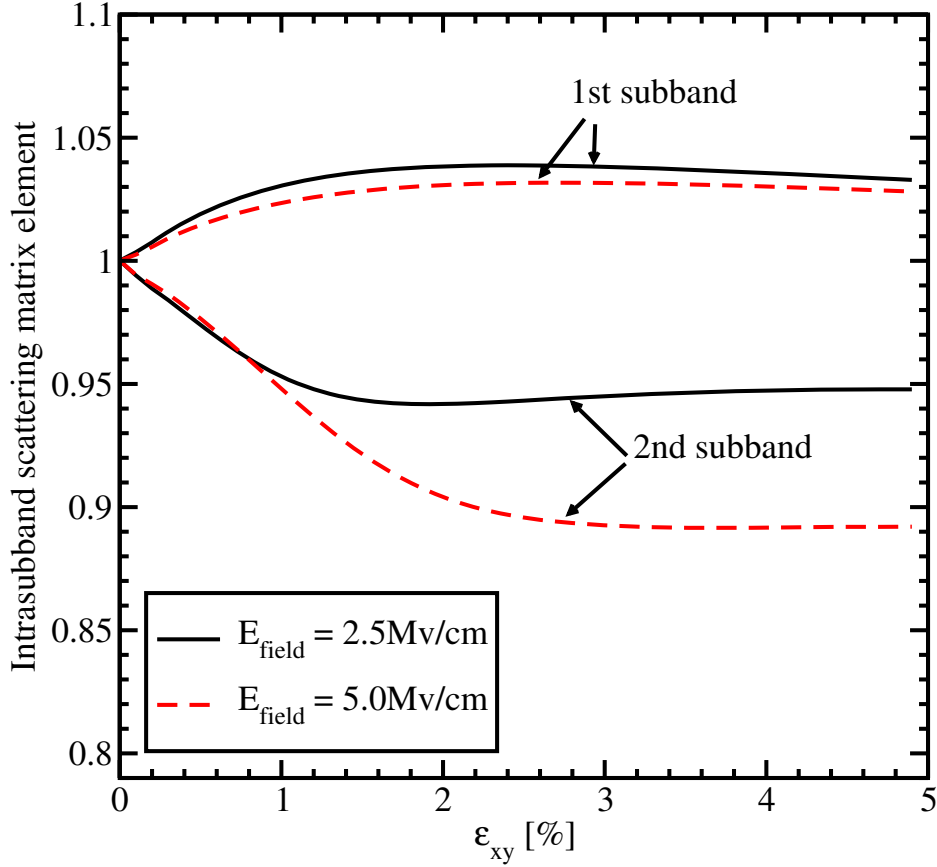
Figure 6.2: Intrasubband scattering matrix elements normalized by their values for zero strain as function of shear strain for different electric field for k_x=0.95nm^{-1}, k_y=0, t=4nm, ΔE_C=10eV.

for several values of ΔE_C, as a function of shear strain. Also the dependence of the longitudinal effective mass normalized to the m_l at zero strain on the shear strain according to Equation 6.2 is shown.

The observed effective mass obtained from the ratio of the matrix elements calculated with two different methods changes only a little with strain. These changes are becoming smaller as the conduction band offset increased. It means that the longitudinal effective mass in Equation 6.1 must not depend on shear strain. Therefore, within the **k·p** method the surface roughness scattering matrix elements are generalized as

$$M_{i,j}(\mathbf{q}) = \left[\frac{\hbar^2}{2m_l(\varepsilon_{xy}=0)} \left(\frac{d\Psi_i(z)}{dz}, \frac{d\Psi_j(z)}{dz} \right) \right] \Bigg|_{z=\pm\frac{t}{2}} \Delta(\mathbf{q}). \tag{6.4}$$

Here, (a, b) is the scalar product between the two multi-component subband functions a and b. An expression similar to Equation 6.4 has been employed in the six-band **k·p** calculations [35].
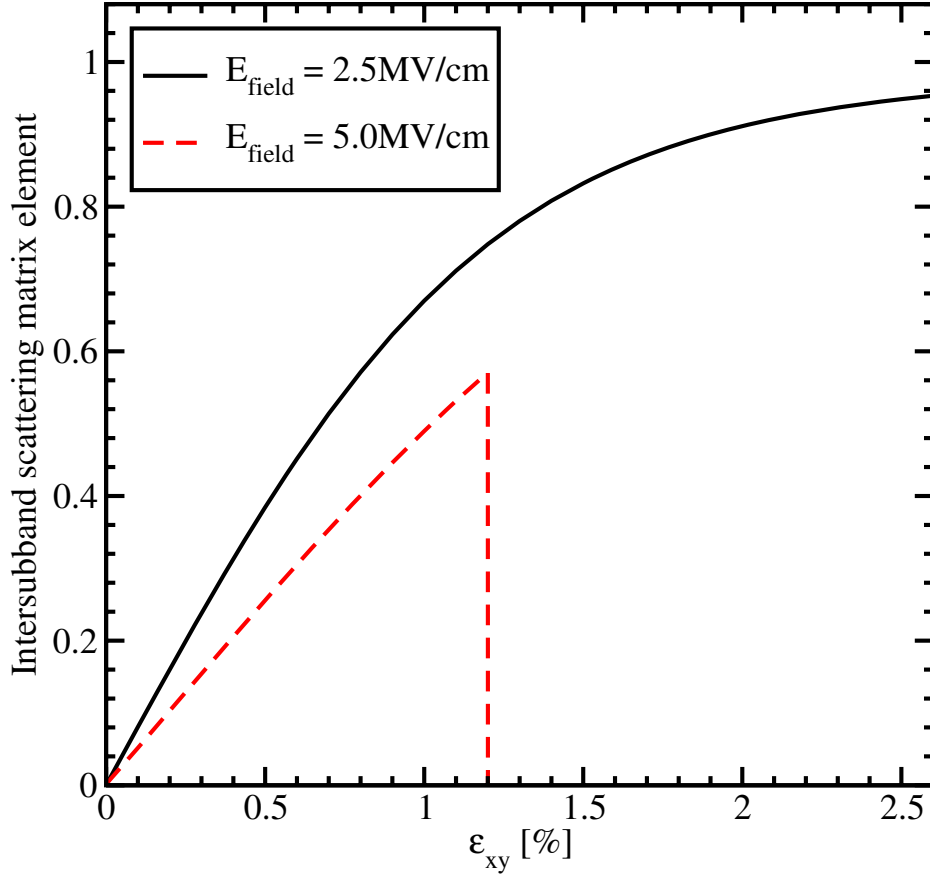
Figure 6.3: Intersubband scattering matrix elements normalized to the value of the intra-subband scattering at zero strain as a function of strain for different electric field. Parameters are the same as for Figure 6.2. Scattering between subbands is limited by kinetic energy, thus the intersubband scattering matrix elements for E_{field}=5MV/cm drop off after shear strain value 1.3%.

The surface roughness induced momentum relaxation matrix elements normalized to the value of the intrasubband scattering at zero strain are then calculated as

$$M_{i,j} = \frac{\frac{d\Psi_{i\sigma}(z)}{dz}\frac{d\Psi_{j\sigma}(z)}{dz}}{\left(\frac{d\Psi_{i\sigma}(z)}{dz}\frac{d\Psi_{i\sigma}(z)}{dz}\right)\Big|_{\varepsilon_{xy}=0}}\Bigg|_{z=\pm\frac{t}{2}}, \tag{6.5}$$

where $\sigma = \pm 1$ is the spin projection to the [001] axis.

The surface roughness at the two interfaces is assumed to be equal and statistically independent. It is described by a mean and a correlation length [35]. Figure 6.2 and Figure 6.3 show the dependences on strain of the matrix elements for intrasubband and intersubband scattering normalized to the value of the intrasubband scattering at zero strain, for two values of the effective electric field. The intrasubband scattering matrix element within the lowest unprimed subband only marginally depends on shear

strain. Indeed, it shows a few percent increase which becomes smaller at high shear strain, where it starts approaching unity again. This is expected in the limit of high stress. In this limit both valleys merge at the common minimum in the X point and the band dispersion is well described by a parabolic approximation [111]. Thus the lowest subband energy and the intrasubband scattering matrix element must approach their respective values in unstrained film where the dispersion is also parabolic.

The intrasubband scattering matrix element in the second subband displays a slight decrease with strain increased, which saturates at high strain. In the high strain limit the second subband, which was equivalent to the first unprimed subbands in the unstrained film, transforms into the second subband of the triangular well potential. Thus the carriers are located effectively further away from the interface. This reduces the value of the intrasubband scattering matrix elements as compared to the unstrained case, in agreement with Figure 6.2. The dependence on the electric field is explained by a slight reduction of the derivative of the wave function at the interface due to its stronger penetration under the potential barrier for higher effective fields.

As shown in Figure 6.3, the intersubband matrix scattering element is zero in an unstrained film, in agreement with the general rule that elastic scattering does not produce transitions between the equivalent subbands originating from the opposite equivalent valleys [55]. Shear strain lifts the subband degeneracy and thus results in a sensible intersubband scattering. Because of the subband splitting, the intersubband scattering depends strongly on the kinetic energy within the lowest subband: if the kinetic energy becomes lower than the subband splitting, the scattering vanishes. The intersubband splitting is larger at stronger effective electric fields, therefore, the intersubband scattering is suppressed already at weaker strain provided the kinetic energy within the subband is the same, in agreement with Figure 6.3.

6.2 Surface Roughness Limited Momentum Relaxation Rates

The surface roughness momentum relaxation rate is calculated in the following way [29, 117]

$$
\begin{aligned}
\frac{1}{\tau_i^{SR}(\mathbf{K}_i)} = & \frac{2\pi}{\hbar(2\pi)^2} \sum_j \int_0^{2\pi} \pi\Delta^2 L^2 \frac{1}{\epsilon_{ij}^2(\mathbf{K}_i - \mathbf{K}_j)} \frac{\hbar^4}{4m_l^2} \frac{|\mathbf{K}_j|}{\left|\dfrac{\partial E(\mathbf{K}_j)}{\partial \mathbf{K}_j}\right|} \cdot \\
& \cdot \left[\left(\frac{d\Psi_{i\mathbf{K}_i\sigma}}{dz}\right)^* \left(\frac{d\Psi_{j\mathbf{K}_j\sigma}}{dz}\right)\right]_{z=\pm\frac{t}{2}}^2 \exp\left(\frac{-(\mathbf{K}_j - \mathbf{K}_i)L^2}{4}\right) d\varphi.
\end{aligned}
\tag{6.6}
$$

$\mathbf{K}_i, \mathbf{K}_j$ are the in-plane wave vectors before and after scattering, φ is the angle between $\mathbf{K}_i$ and $\mathbf{K}_j$, ϵ is the dielectric permittivity, L is the autocorrelation length, Δ is the

mean square value of the surface roughness fluctuations, $\Psi_{i\mathbf{K}_i}$ and $\Psi_{j\mathbf{K}_j}$ are the wave functions, and $\sigma = \pm 1$ is the spin projection to the [001] axis.

6.3 Phonon Induced Momentum Scattering Rates

The momentum scattering relaxation rate is calculated as

$$
\begin{aligned}
\frac{1}{\tau_i^{PH}(\mathbf{K}_i)} =& \frac{2\pi k_B T}{\hbar \rho \upsilon_{PH}^2} \sum_j \int_0^{2\pi} \frac{d\phi}{2\pi} \frac{1}{(2\pi)^2} \frac{\mathbf{K}_j}{\left|\frac{\partial E_j}{\partial \mathbf{K}_j}\right|} \left[1 - \frac{\left|\frac{\partial E(\mathbf{K}_j)}{\partial \mathbf{K}_j}\right| f(E(\mathbf{K}_j))}{\left|\frac{\partial E(\mathbf{K}_i)}{\partial \mathbf{K}_i}\right| f(E(\mathbf{K}_i))}\right] \cdot \\
& \cdot 2\pi \int_0^t \left[\Psi_{j\mathbf{K}_{j\sigma}}^\dagger(z) M^{PH} \Psi_{i\mathbf{K}_{i\sigma}}(z)\right] \left[\Psi_{j\mathbf{K}_{j\sigma}}^\dagger(z) M^{PH} \Psi_{i\mathbf{K}_{i\sigma}}(z)\right] dz \cdot \\
& \cdot \theta(E_i - E_j),
\end{aligned}
\tag{6.7}
$$

where $\upsilon_{PH} = \dfrac{2\upsilon_{TA} + \upsilon_{LA}}{3}$ [51], and M^{PH} is defined as

$$
M^{PH} = \begin{bmatrix} \Xi & 0 & 0 & 0 \\ 0 & \Xi & 0 & 0 \\ 0 & 0 & \Xi & 0 \\ 0 & 0 & 0 & \Xi \end{bmatrix},
\tag{6.8}
$$

with $\Xi = 12\text{eV}$ [34, 36].

6.4 Momentum Relaxation Time Calculation

The momentum relaxation times are calculated by thermal averaging [35, 70, 107] as

$$
\frac{1}{\tau} = \frac{\sum_i \int \frac{1}{\tau_i(\mathbf{K}_i)} f(E_i)(1 - f(E_i)) \, d\mathbf{K}_i}{\sum_i \int f(E_i) \, d\mathbf{K}_i},
\tag{6.9}
$$

$$
f(E) = \frac{1}{1 + \exp\left(\dfrac{E - E_F}{k_B T}\right)},
\tag{6.10}
$$

$$
\int d\mathbf{K}_i = \int_0^{2\pi} \int_{E_i^{(0)}}^\infty \frac{\mathbf{K}_i}{\left|\frac{\partial E_i}{\partial \mathbf{K}_i}\right|} \, d\varphi \, dE,
\tag{6.11}
$$
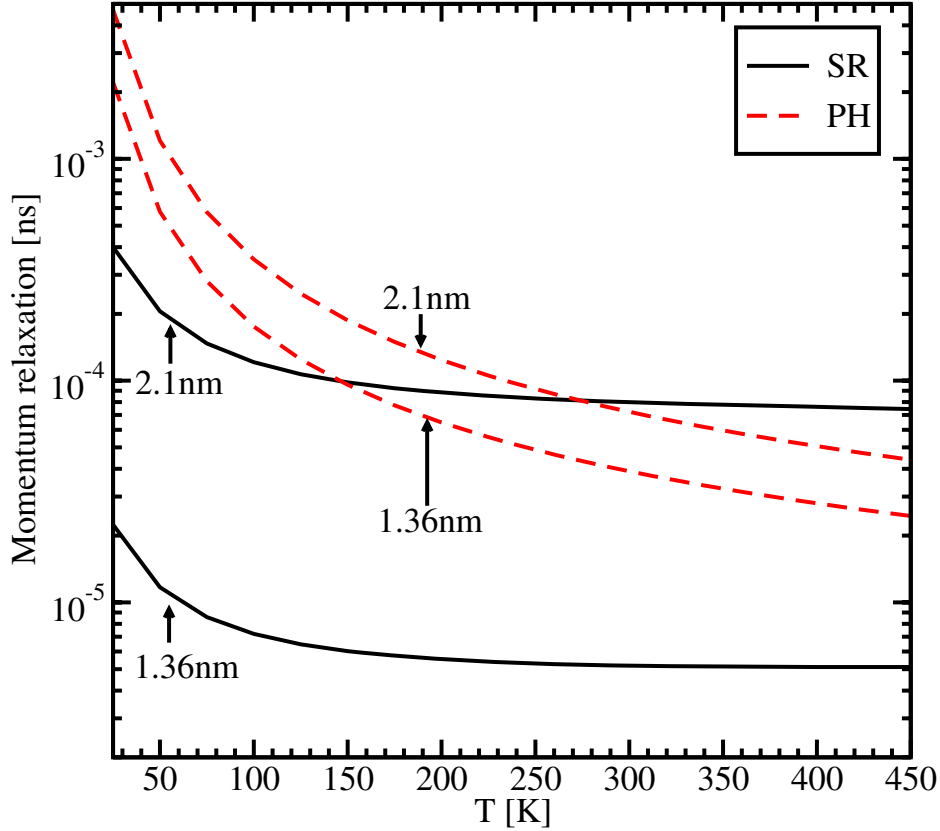
Figure 6.4: Dependence of the momentum relaxation time induced by surface roughness (SR) and acoustic phonons (PH) on temperature for two different thicknesses, $\varepsilon_{xy}=0$, and electron concentration of $1.29 \cdot 10^{12} \text{cm}^{-2}$.

where k_B is the Boltzmann constant, T is the temperature, E_F is the Fermi energy, $E = E_i^{(0)} + E_i(\mathbf{K}_i)$, $E_i^{(0)} = E_i(\mathbf{K}_i = 0)$ is the energy of the bottom of the subband i, and

$$\left| \frac{\partial E_i}{\partial \mathbf{K}_i} \right| = \left| \frac{\partial E (\mathbf{K}_i)}{\partial \mathbf{K}_i} \right|_{\varphi,E}, \tag{6.12}$$

is the derivative of the subband dispersion along $\mathbf{K}_i$ at the angle φ defining the $\mathbf{K}_i$ direction.

Figure 6.4 shows the dependence of the momentum relaxation time on temperature for surface roughness and acoustic phonons. For the film thicknesses 2.1nm and 1.36nm the contribution from the surface roughness is dominant at low temperatures. However, for a temperature around 280K the contributions from the surface roughness and from the acoustic phonons for the film of thickness 2.1nm are equal. Any further increase of temperature leads to higher values of the momentum relaxation time caused by acoustic phonons. Figure 6.4 illustrates that the dominant relaxation mechanism strongly depends on film thickness. The phonons limited momentum relaxation is
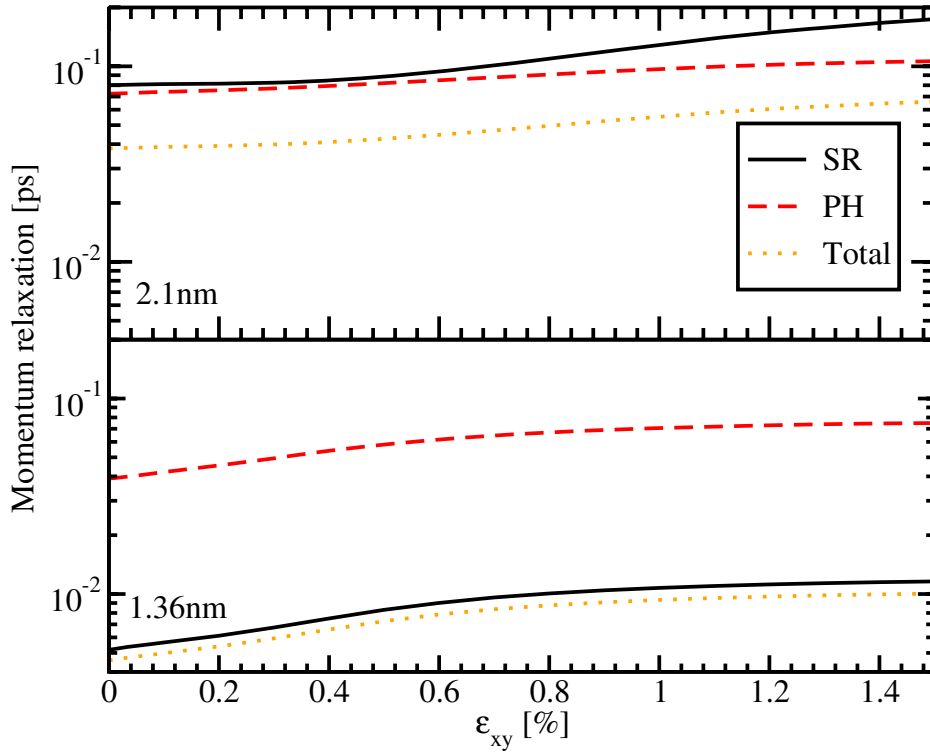
Figure 6.5: Dependence of the momentum relaxation time induced by surface roughness
(SR) and acoustic phonons (PH) on shear strain for 1.36nm and 2.1nm film
thickness, for T=300K, and electron concentration $1.29 \cdot 10^{12} \mathrm{cm}^{-2}$.

characterized by a much weaker thickness dependence and does not change signifi-
cantly when the thickness decreases from 2.1nm to 1.36nm. The surface roughness
limited momentum relaxation decreases by more than an order of magnitude as ex-
pected [35, 55]. Thus, for the thickness of 1.36nm the surface roughness induced spin
relaxation is the dominant mechanism for the whole range of considered tempera-
tures.

Figure 6.5 shows the dependence of the different mechanisms of the momentum relax-
ation together, including the total momentum relaxation time, as a function of shear
strain. The improvement of the momentum relaxation time due to the shear strain is
around 82% for the film thickness of 2.1nm and around 120% for the film thicknesses
1.36nm. The acoustic phonons limited momentum relaxation improves around 45% for
2.1nm and around 92% for 1.36nm. The surface roughness limited momentum relax-
ation time increases around 110% for 2.1nm and around 120% for 1.36nm. Due to the
dominant surface roughness mechanism for the film thickness of 1.36nm, the increase
of the total momentum relaxation time is higher for 1.36nm than for 2.1nm. The in-
crease of the momentum relaxation time is due to the corresponding scattering matrix
elements dependence on strain. Combined with the strain induced transport effective
mass decrease it should result in an even better mobility improvement supporting the
use of uniaxial tensile strain as the mobility booster in fully depleted ultra-thin SOI
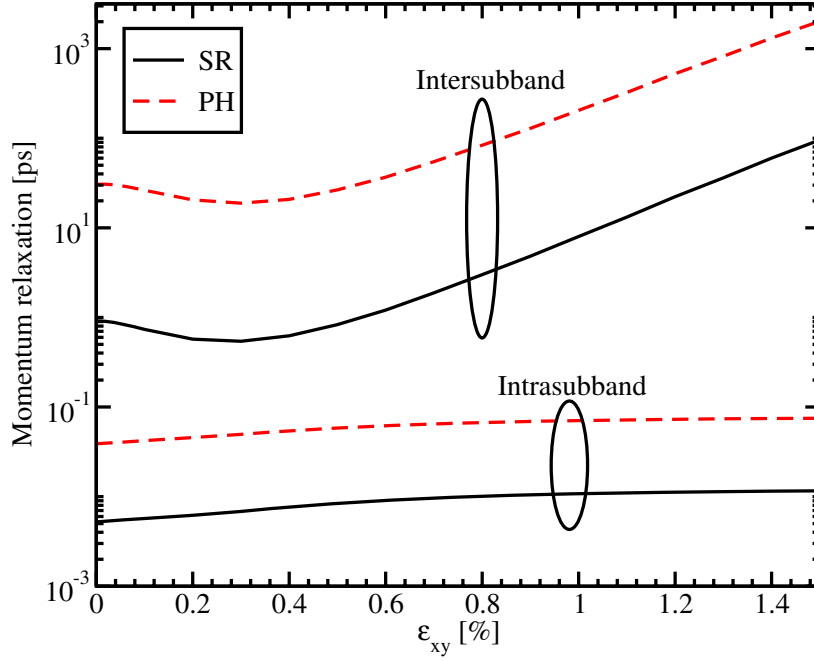
Figure 6.6: Dependence of the intersubband and intrasubband components of the momentum relaxation time induced by surface roughness (SR) and acoustic phonons (PH) on shear strain for the film thickness 1.36nm, T=300K, and electron concentration $1.29 \cdot 10^{12}$cm^{-2}.

FETs.

Figure 6.6 demonstrates the contribution of the inter- and intrasubband processes to the acoustic phonon and surface roughness limited momentum relaxation. The domination of the intrasubband relaxation processes for both mechanisms of the momentum relaxation is shown, in agreement with the selection rule that the elastic processes result in strong intrasubband relaxation. The dominance of the surface roughness mechanism for the film thickness 1.36nm shown in Figure 6.4 and Figure 6.5 is the consequence of the high intrasubband relaxation rate.

6.5 Mobility Calculation

The electron mobility in the inversion layer in the [110] direction is calculated as [35]

$$
\begin{aligned}
\mu_{110} =& \frac{e}{4\pi^2 \hbar^2 k_B T n_s} \sum_i \int_0^{2\pi} d\phi \int_{E_i^{(0)}}^{\infty} dE \frac{|\mathbf{K}_i|}{\left| \frac{\partial E(\mathbf{K}_i)}{\partial \mathbf{K}_i} \right|} \cdot \\
& \cdot \left(\frac{\partial E(\mathbf{K}_i)}{\partial \mathbf{K}_i} \right)^2_{\varphi=\pi/4, E} \tau_{110}^{(i)} f(E) \left(1 - f(E) \right),
\end{aligned}
\tag{6.13}
$$

47
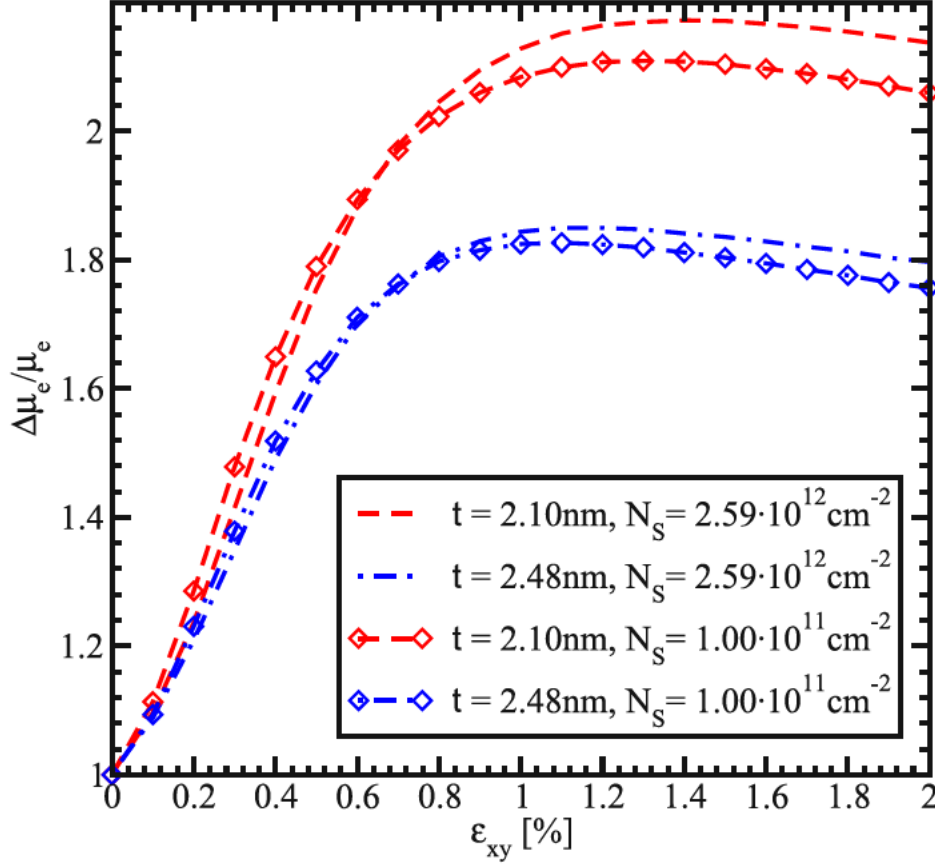
Figure 6.7: Electron mobility enhancement, $\Delta\mu_e/\mu_e$, induced by shear strain as a function of strain for different thicknesses and electron concentration values of a temperature of 300K.

where $n_s = \sum_i n_i$, n_i is the population of subband i, and $\tau_{110}^{(i)}$ is the momentum relaxation time in subband i for [110] direction.

When more than one scattering process is considered, for example surface roughness and electron-phonon, the total mobility is calculated by Matthiessen's rule [64, 65]

$$\frac{1}{\mu} = \frac{1}{\mu^{SR}} + \frac{1}{\mu^{PH}}, \tag{6.14}$$

where μ is the total mobility, μ^{SR} is the mobility due to surface roughness, and μ^{PH} is the mobility due to lattice phonons.

Figure 6.7 shows the electron mobility enhancement in [110] direction along tensile stress as a function of shear strain. The simulations show that the mobility in thin silicon films increases by a factor of two. The increase depends on the electron concentration and the film thickness. For the thicknesses considered a strong mobility enhancement is observed up to a shear strain value around 0.5%. When the shear
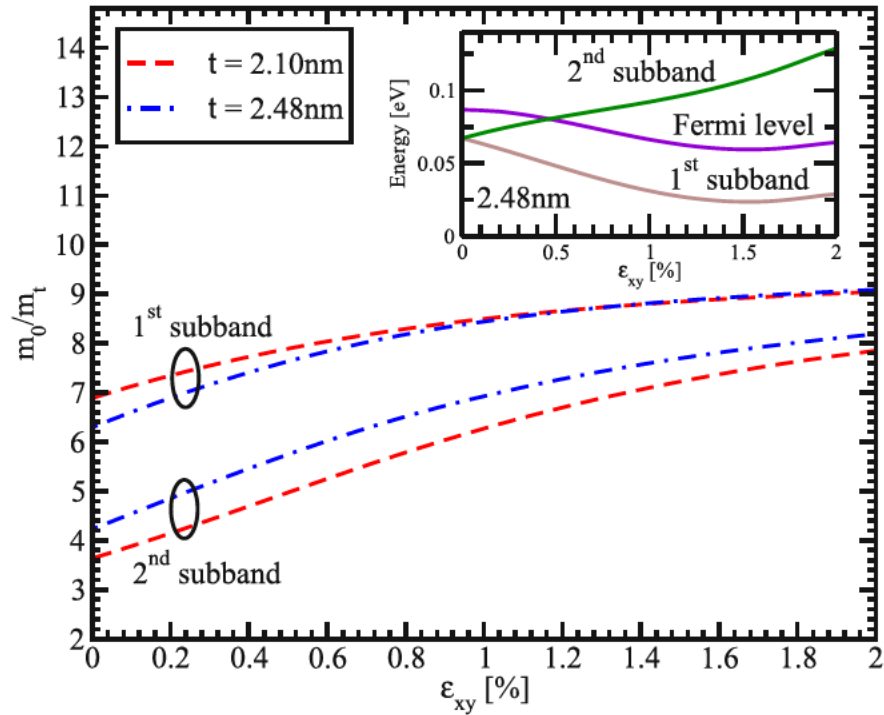
Figure 6.8: One over effective mass for the two lowest subbands as a function on shear strain for different film thicknesses. The inset shows the subbands energies and the Fermi level as a function of shear strain.
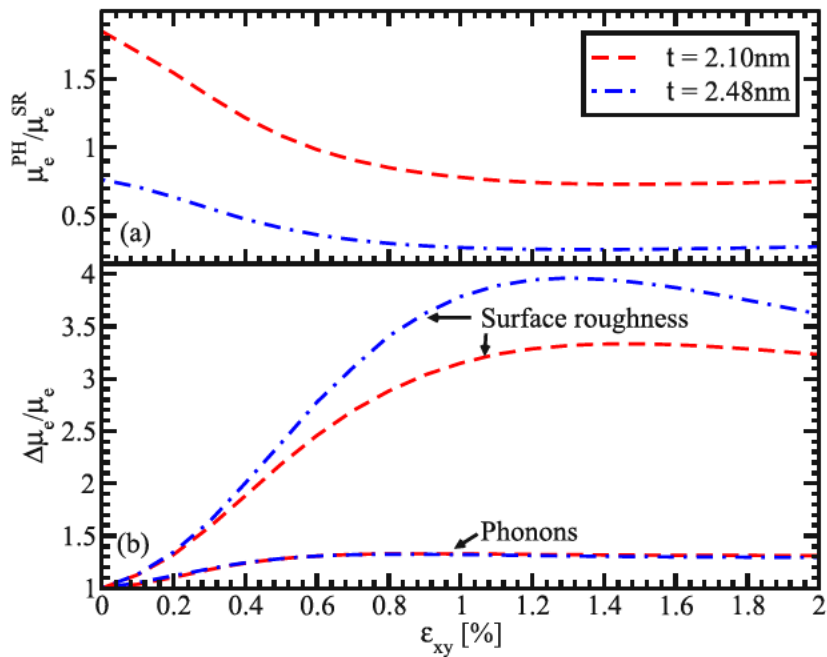
Figure 6.9: Dependence of (a) the phonon electron mobility to the surface roughness mobility ratio and (b) phonon and surface roughness electron mobility enhancement on shear strain for several thicknesses for an electron concentration of $2.59 \cdot 10^{12} \text{cm}^{-2}$.
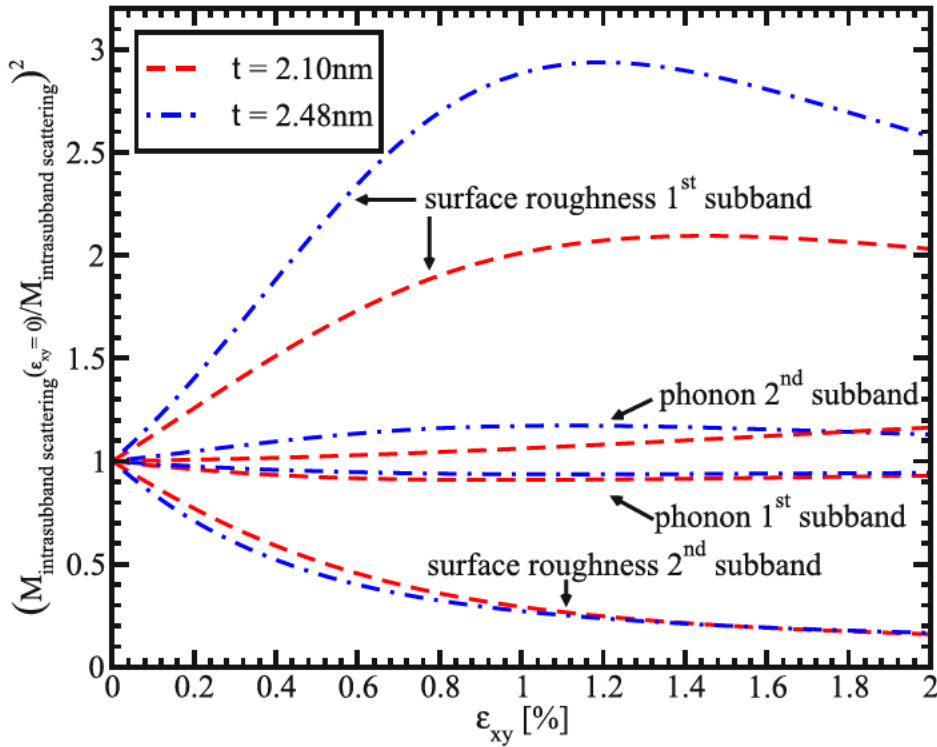
Figure 6.10: Dependence of the inversed normalized square of surface roughness and phonon intrasubband matrix elements for different film thicknesses.

strain is further increased the mobility saturates and even shows a slight decrease for the film thickness 2.1nm and 2.48nm.

The [110] mobility enhancement in surface layers due to tensile stress applied along the channel is usually explained by the effective transport mass reduction [115, 116]. However, the effective mass decrease in the lowest subband shown in Figure 6.8 may only account for roughly one half of the mobility enhancement obtained and cannot explain the two-fold mobility enhancement. Thus, a more detailed analysis is needed to understand the effect. The ratio of the phonon electron mobility to the surface roughness limited mobility as a function of strain is shown in Figure 6.9a. The surface roughness limited mobility in the 2.1nm thick film is of the same order as the phonon electron mobility. Thus, the total mobility is determined by the interplay between these two mechanisms. For the 2.48nm thick film the contribution of the phonon mobility is higher than for the 2.1nm thick film. The enhancement of the surface roughness and phonon limited mobility is shown in Figure 6.9b. The phonon mobility demonstrates an increase of about 40% consistent with the transport effective mass decrease. This behavior is supported by an almost negligible dependence of the electron-phonon scattering matrix elements on strain (Figure 6.10).

On the other hand, the surface roughness limited mobility for 2.1nm and 2.48nm thick films rises by about 200 and 300 percent, respectively, at around 1.2% shear strain and

shows a slight decrease at strain values bigger than 1.2%. This behavior is dictated by the corresponding enhancement of the inverse surface roughness scattering matrix elements (Figure 6.10). The mobility enhancement shown in Figure 6.9b and their ratio shown in Figure 6.9a are consistent with the total mobility enhancement observed in Figure 6.7. Indeed, for the t=2.1nm film the unaccounted mobility enhancement is mostly due to the surface roughness limited mobility increase. Although the surface roughness limited mobility growths even stronger for t=2.48nm, the main contribution limiting the mobility is the phonon scattering. For this reason the whole mobility is slightly less enhanced as compared to that in the t=2.1nm film.

7 Spin Relaxation

7.1 Strain Dependence of Surface Roughness Limited Spin Relaxation Matrix Elements

The surface roughness induced spin relaxation matrix elements are calculated between wave functions with opposite spin projections. The matrix elements are calculated in the same manner as in Chapter 6, i.e. the spin relaxation matrix elements normalized to the value of the intrasubband scattering at zero strain are written as

$$
M_{i,j} = \left. \frac{\frac{d\Psi_{i-\sigma}(z)}{dz} \frac{d\Psi_{j\sigma}(z)}{dz}}{\left(\frac{d\Psi_{i\sigma}(z)}{dz} \frac{d\Psi_{i\sigma}(z)}{dz} \right) \Big|_{\varepsilon_{xy}=0}} \right|_{z = \pm \frac{t}{2}}. \tag{7.1}
$$

Figure 7.1 and Figure 7.2 show the spin relaxation matrix elements (normalized to intravalley scattering at zero strain) on the angle between the incident and scattered wave vectors together with the valley splitting for the scattered wave. Oscillations of the valley splitting are observed. In Figure 7.1 the sharp increase of the relaxation matrix element is correlated with the reduction of the valley splitting which occurs for the values of the angle determined by zeroes of the $D\varepsilon_{xy} - \dfrac{\hbar^2 k_x k_y}{M}$ term. This is the condition of the formation of the so called spin hot spots characterized by the maximum spin mixing. In contrast to Figure 7.1, the valley splitting reduction due to the $\left| \sin \left(\sqrt{\dfrac{1 - y_n^2 - \eta^2}{1 - y_n^2}} k_0 t \right) \right|$ term shown in Figure 7.2 does not lead to a sharp increase of the spin relaxation matrix elements on the angle between the incident and scattered waves.

The splitting between the subbands depends on $D\varepsilon_{xy} - k_x k_y / M$ and their degeneracy is lifted by the kinetic-like term $k_x k_y / M$ even without shear strain. This results in a strong dependence of the surface roughness induced spin relaxation matrix elements on the angle between the incident and outgoing wave vectors (Figure 7.1 and Figure 7.2). Figure 7.3 shows the dependences of the relaxation matrix elements on this angle for different values of shear strain. The sharp peaks in Figure 7.3 for shear strain values 0.05% and 0.1% nature of which were discussed for Figure 7.1 and Figure 7.2 are observed for similar angle values. However, the intersubband matrix relaxation elements for higher strain show lower values, except peaks. For the shear strain of 1%

52
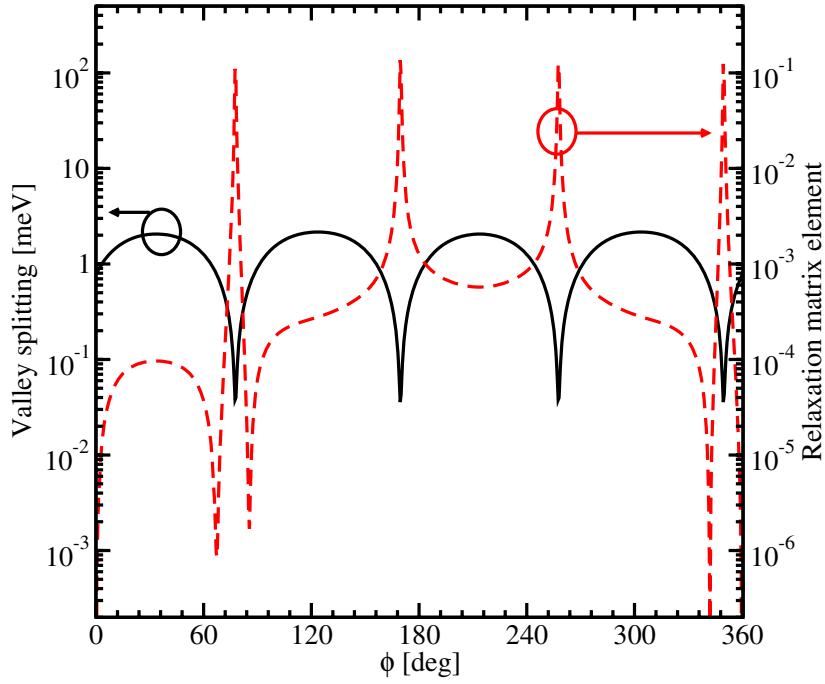
Figure 7.1: Dependence of the normalized spin relaxation matrix elements and valley splitting on the angle between the incident and scattered waves for the quantum well thickness is 4nm, the conduction band offset is 4eV, k_x=0.5nm^{-1}, k_y=0.1nm^{-1}, E_{field}=0MV/cm, ε=0.01%.
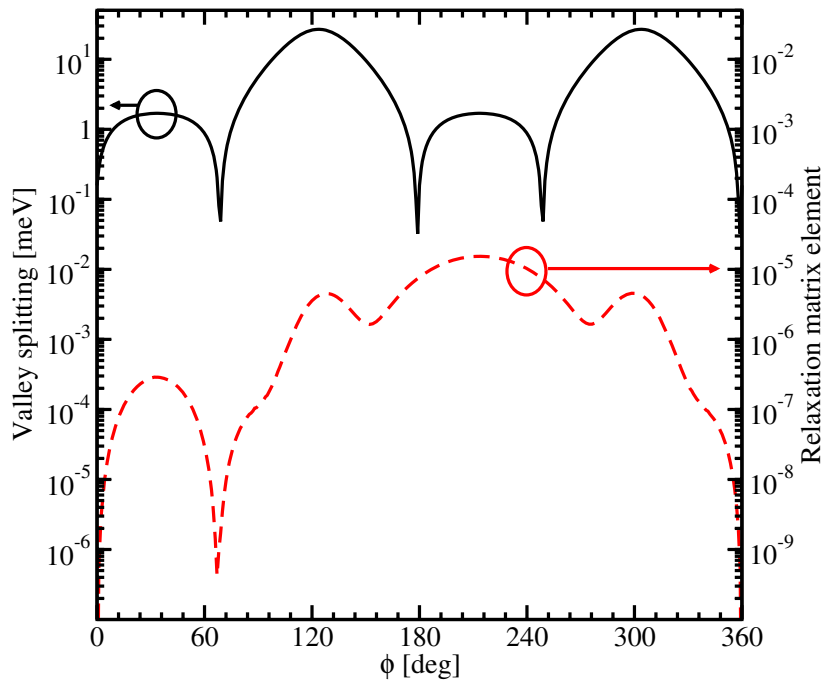
Figure 7.2: Dependence of the normalized spin relaxation matrix elements and valley splitting on the angle between the incident and scattered waves for the quantum well thickness is 4nm, the conduction band offset is 4eV, k_x=0.5nm^{-1}, k_y=0.1nm^{-1}, E_{field}=0MV/cm, ε=0.92%.
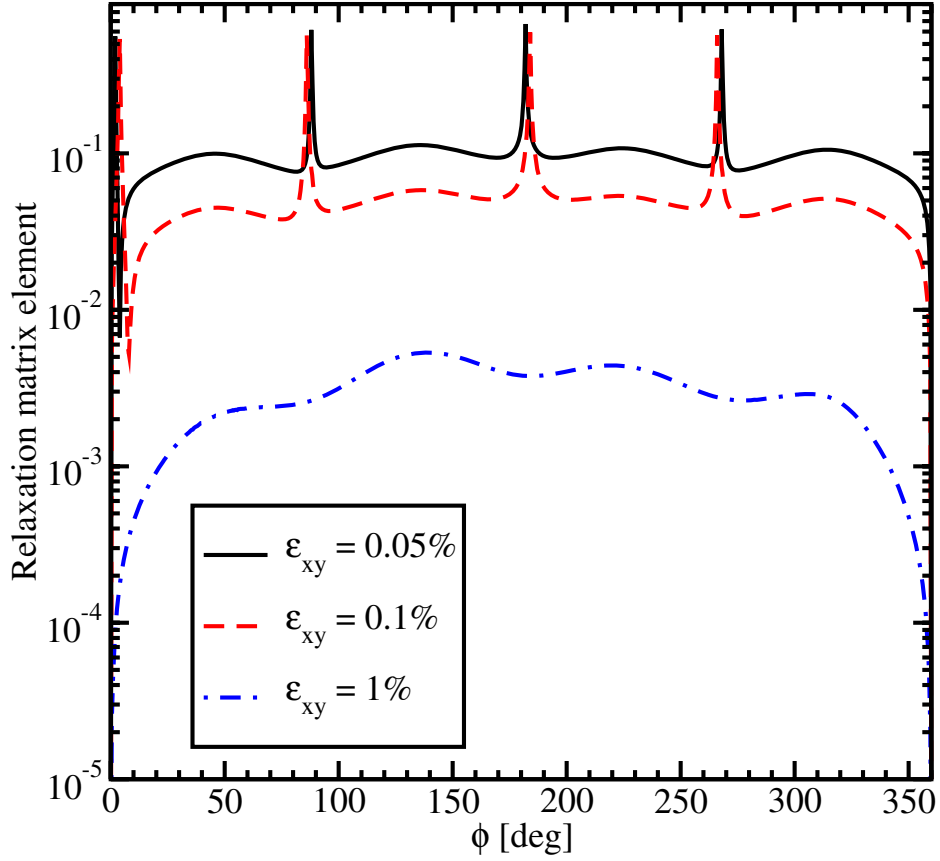
Figure 7.3: Dependence of the normalized spin relaxation matrix elements on the angle
between the incident and the relaxed wave for different values of strain for
k_x=0.8nm^{-1}, k_y=0, t=4nm, ΔE_C=10eV.

no peaks are observed and the matrix element values are smaller by several orders of
magnitude. As follows from Figure 7.3, shear strain leads to the reduction of the spin
relaxation matrix element.

Figure 7.4 and Figure 7.5 show the dependences on strain and electric field of the
matrix elements for the intrasubband and intersubband scattering. The intrasubband
scattering matrix elements have two decreasing regions shown in Figure 7.4. These
regions are in good agreement with the valley splitting minima in Figure 5.19. For
higher fields the second decreasing region around the shear strain value of 0.931%
vanishes. For the electric field of 0.5MV/cm the intrasubband matrix elements are
sharply reduced only for the shear strain value of 0.116%. At the same time, the
intersubband matrix elements show a sharp increase around the shear strain value of
0.116%. The electric field does not affect much the valley splitting provided by the
zero value of the term $D\varepsilon_{xy} - \dfrac{\hbar^2 k_x k_y}{M}$, and the sharp increase in the intersubband
matrix elements is observed at higher fields. At the same time the electric field washes
out a sharp minimum around the shear strain value of 0.931% in Figure 7.5. With
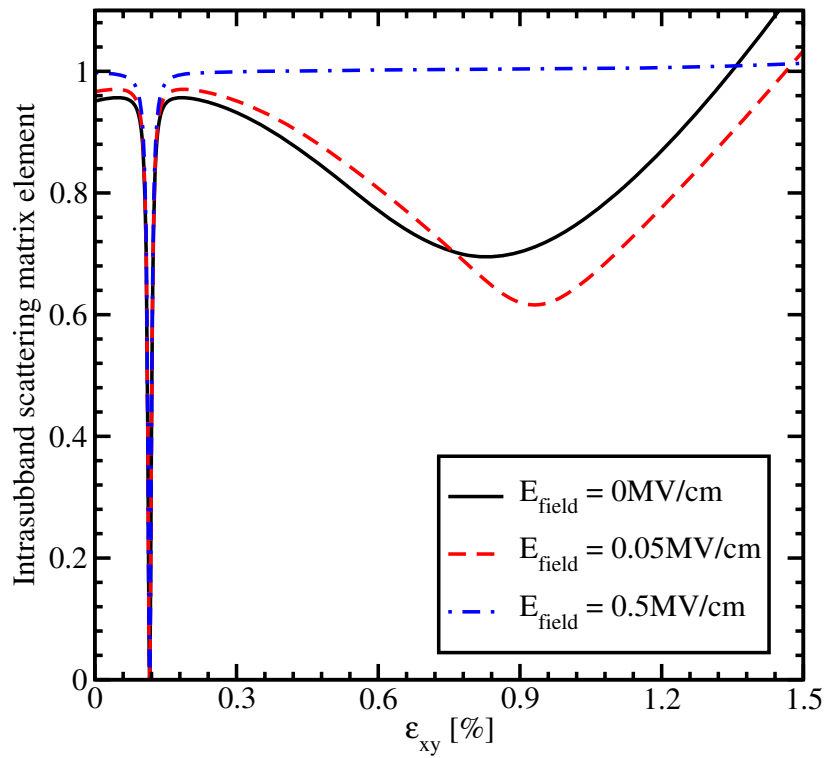
Figure 7.4: Intravalley scattering matrix elements normalized by their values for zero strain as a function of shear strain for different electric field values.
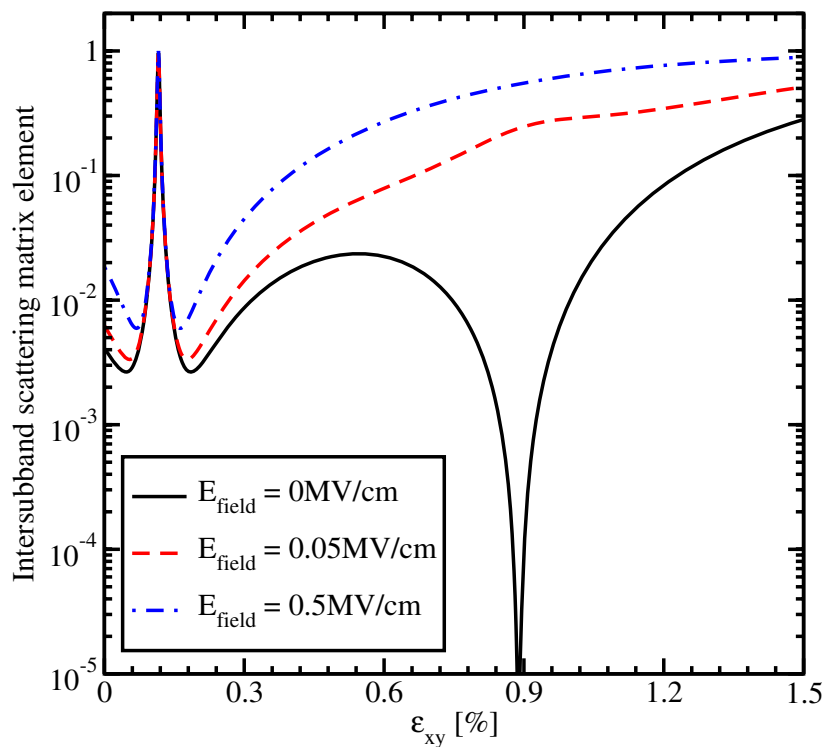
Figure 7.5: Intervalley scattering matrix elements normalized to the value of the intravalley scattering at zero strain as a function of strain for different electric field values.
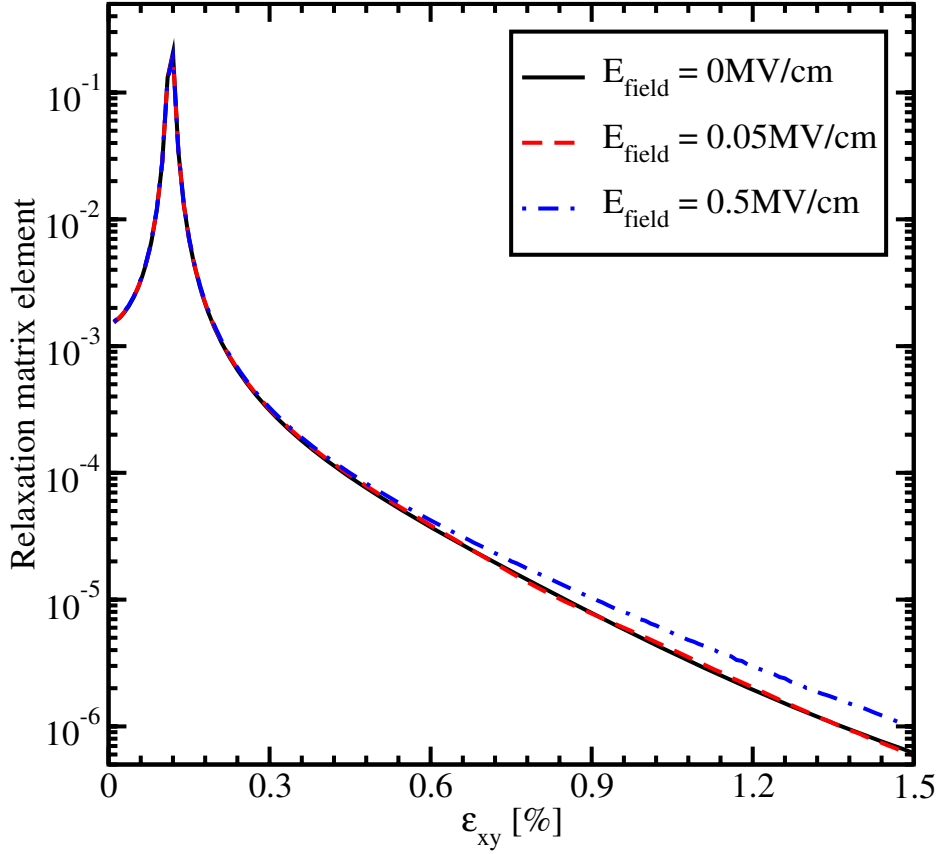
Figure 7.6: Spin relaxation matrix elements normalized to intravalley scattering at zero strain dependence on shear strain for several values of the electric field, k_x=0.5nm^{-1}, k_x=0.1nm^{-1}.

the electric field increased the confinement pushes the carriers closer to the interface which results in both an intersubband and an intrasubband scattering matrix elements increase.

The dependence of the spin relaxation matrix elements on shear strain for several values of the electric field is shown in Figure 7.6. The spin relaxation matrix elements increase until the strain value 0.116%, the point determined by the spin hot spot condition. Applying strain larger than 0.116% suppresses the spin relaxation significantly, for all values of the electric field. In contrary to the scattering matrix elements (Figure 7.4 and Figure 7.5), the relaxation matrix elements demonstrate a sharp feature only for the shear strain value of 0.116% at zero electric field. Large electric field leads to an increase of the relaxation matrix elements due to the additional field-induced confinement resulting in higher values of the surface roughness induced spin relaxation matrix elements.

Figure 7.7 displays the normalized spin relaxation matrix elements for an unstrained film. The "hot spots" are along the [100] and [010] directions. Shear strain pushes the
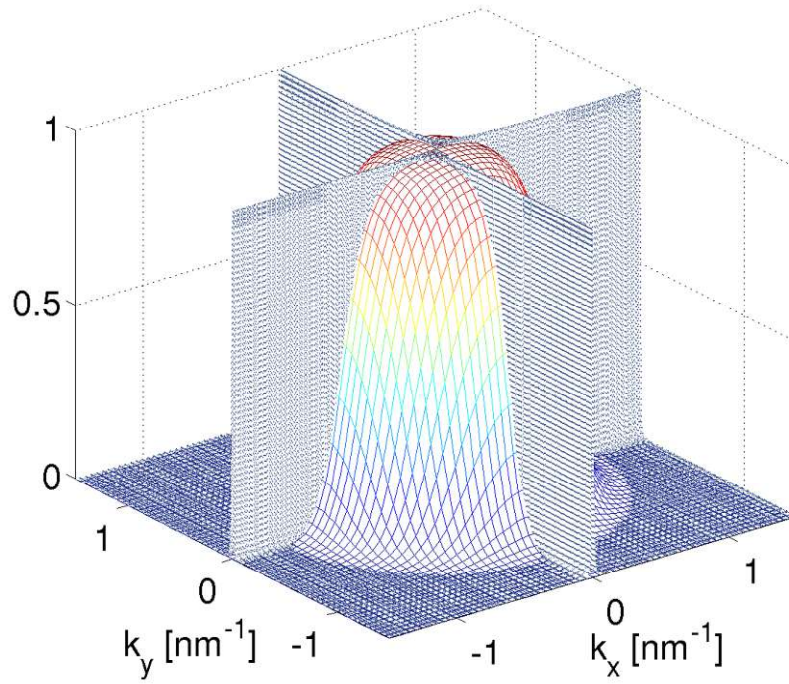
Figure 7.7: Intersubband relaxation matrix elements normalized to the intrasubband scattering elements at zero strain for an unstrained sample. The Fermi distribution for 300K is also shown.
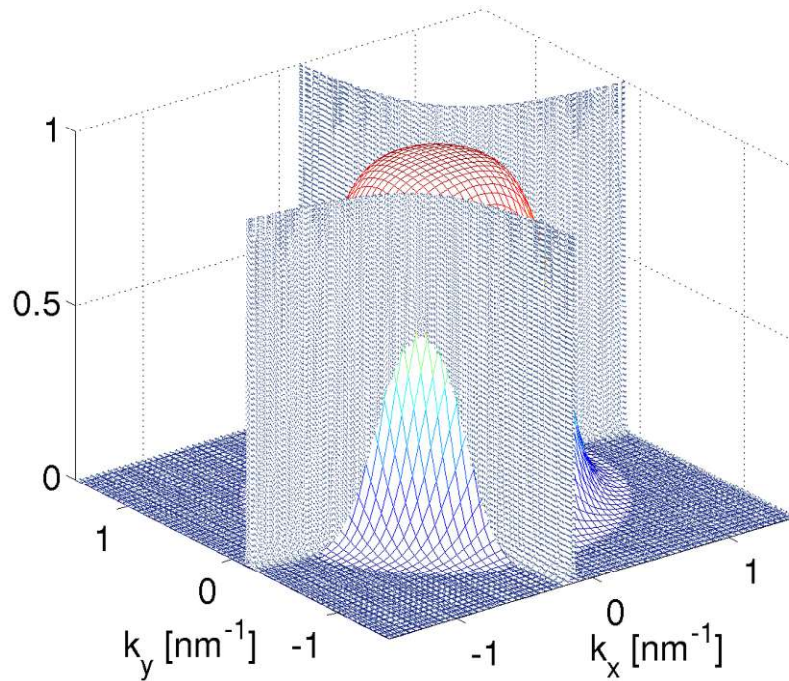
Figure 7.8: Normalized intersubband relaxation matrix elements for shear strain 0.5% shown together with the Fermi distribution at 300K.

"hot spots" to higher energies (Figure 7.8) outside of the states occupied by carriers. This leads to a reduction of the spin relaxation.

7.2 Spin Relaxation Rate

7.2.1 Surface Roughness Induced Spin Relaxation Rate

The surface roughness spin relaxation rate is calculated in the following way [29,117]

$$
\frac{1}{\tau_i^{SR}(\mathbf{K}_i)} = \frac{4\pi}{\hbar(2\pi)^2} \sum_j \int_0^{2\pi} \pi\Delta^2 L^2 \frac{1}{\epsilon_{ij}^2(\mathbf{K}_i - \mathbf{K}_j)} \frac{\hbar^4}{4m_l^2} \frac{|\mathbf{K}_j|}{\left|\dfrac{\partial E(\mathbf{K}_j)}{\partial \mathbf{K}_j}\right|} \cdot
$$
$$
\cdot \left[\left(\frac{d\Psi_{i\mathbf{K}_i-\sigma}}{dz}\right)^* \left(\frac{d\Psi_{j\mathbf{K}_j\sigma}}{dz}\right)\right]^2_{z=\pm\frac{t}{2}} \exp\left(\frac{-(\mathbf{K}_j - \mathbf{K}_i)L^2}{4}\right) d\varphi. \tag{7.2}
$$

$\mathbf{K}_i, \mathbf{K}_j$ are the in-plane wave vectors before and after scattering, φ is the angle between $\mathbf{K}_i$ and $\mathbf{K}_j$, ϵ is the dielectric permittivity, L is the autocorrelation length, Δ is the mean square value of the surface roughness fluctuations, $\Psi_{i\mathbf{K}_i}$ and $\Psi_{j\mathbf{K}_j}$ are the wave functions, and $\sigma = \pm 1$ is the spin projection to the [001] axis.

7.2.2 Phonons

All atoms in an ideal crystal lattice are fixed at their periodic positions. However, ions in non-ideal lattices oscillate around their fixed position. The oscillations depend on the lattice temperature and are called ion temperature oscillations. The nature of such oscillations is described by phonons. Since phonons have an oscillating nature a characteristic frequency ω_q can be associated with them. The energy of a phonon is characterized by the frequency ω_q is $\hbar\omega_q$. Oscillation are usually considered for a primitive cell. If the center mass of the cell during oscillations does not move then consider optic phonons, otherwise - acoustic phonons [64,65,131,133]. The number of optic modes for the primitive cell that contains p atoms is determined by the expression $3(p-1)$, while the number of acoustic modes is always 3. Each of the modes has three components - two transversal (TA1, TA2, TO1, TO2) and one longitudinal (LA, LO).

Following Ehrenreich and Overhauser [26] the phonons polarization vectors are written as

$$
e_{LA} = \frac{1}{q}\begin{bmatrix} q_x \\ q_y \\ q_z \end{bmatrix}, \tag{7.3}
$$

$$e_{TA1} = \frac{1}{\sqrt{q_x^2 + q_y^2}} \begin{bmatrix} q_y \\ -q_x \\ 0 \end{bmatrix}, \tag{7.4}$$

$$e_{TA2} = \frac{1}{q\sqrt{q_x^2 + q_y^2}} \begin{bmatrix} q_x q_z \\ q_y q_z \\ -\left(q_x^2 + q_y^2\right) \end{bmatrix}, \tag{7.5}$$

with $q = \sqrt{q_x^2 + q_y^2 + q_z^2}$.

Spin relaxation rates for transitions from band i to band j by mechanism m (i.e., acoustic phonon or optical phonon), are calculated using Fermi's second Golden Rule [45, 86, 107]

$$\frac{1}{\tau_i(\mathbf{K}_i)} = \frac{2(4)\pi}{\hbar} \int \frac{d^2\mathbf{K}_j}{(2\pi)^2} |M_{m;i,j}(\mathbf{K}_i, \mathbf{K}_j)|^2 \delta(E_j - E_i + \Delta E_m), \tag{7.6}$$

where M is the momentum scattering (spin relaxation) matrix element, the material volume is chosen as the unit volume, 4π for spin relaxation accounts for the fact that the net number of spin polarized electrons changes by two with each spin flip [107].

7.2.3 Intravalley and g-Intervalley Relaxation Processes Rates

The acoustic phonons scattering rate for the wave vector $\mathbf{K}_i$ in subband i is written as [35]

$$\frac{1}{\tau_i^{AC}(\mathbf{K}_i)} = \frac{4\pi k_B T}{\hbar \rho v^2} \sum_j \int_0^{2\pi} \frac{d\phi}{2\pi} \int_{-\infty}^{\infty} \frac{dq_z}{(2\pi)^2} \frac{\mathbf{K}_j}{\left|\frac{\partial E_j}{\partial \mathbf{K}_j}\right|} \cdot$$
$$\cdot \left[1 - \frac{\left|\frac{\partial E(\mathbf{K}_j)}{\partial \mathbf{K}_j}\right| f(E(\mathbf{K}_j))}{\left|\frac{\partial E(\mathbf{K}_i)}{\partial \mathbf{K}_i}\right| f(E(\mathbf{K}_i))}\right] \cdot \tag{7.7}$$
$$\cdot \sum_{\alpha\beta} \left|\frac{q_\alpha}{q} e_\beta(\mathbf{q}) \sum_{\nu,\mu} D_{\alpha\beta}^{(\nu,\mu)} \int_0^t dz \Psi_{\mu\mathbf{K}_j}^*(z) \exp(-iq_z z) \Psi_{\nu\mathbf{K}_i}(z)\right|^2 \cdot$$
$$\cdot \theta(E_i - E_j).$$

Here, $q = (\mathbf{K}_j - \mathbf{K}_i, q_z)$ is the phonon wave vector, $D_{\alpha\beta}^{(\nu,\mu)}$ is the deformation potential, $\alpha, \beta = \{x, y\}$, $e_\beta(\mathbf{q}) = \{e_{LA}(\mathbf{q}), e_{TA1}(\mathbf{q}), e_{TA2}(\mathbf{q})\}$ is the polarization vector.

By applying Fubini's theorem the modulus in Equation 7.7 is replaced with the repeated integral

$$
\begin{aligned}
\frac{1}{\tau_i^{AC}(\mathbf{K}_i)} =& \frac{4\pi k_B T}{\hbar \rho \upsilon^2} \sum_j \int_0^{2\pi} \frac{d\phi}{2\pi} \int_{-\infty}^{\infty} \frac{dq_z}{(2\pi)^2} \frac{\mathbf{K}_j}{\left|\dfrac{\partial E_j}{\partial \mathbf{K}_j}\right|} \cdot \\
& \cdot \left[1 - \frac{\left|\dfrac{\partial E(\mathbf{K}_j)}{\partial \mathbf{K}_j}\right| f(E(\mathbf{K}_j))}{\left|\dfrac{\partial E(\mathbf{K}_i)}{\partial \mathbf{K}_i}\right| f(E(\mathbf{K}_i))}\right] \cdot \\
& \cdot \int_0^t \int_0^t \left[\Psi_{j\mathbf{K}_j}^{\dagger}(z) M^{AC} \Psi_{i\mathbf{K}_i}(z)\right] \cdot \\
& \cdot \left[\Psi_{j\mathbf{K}_j}^{\dagger}(z') M^{AC} \Psi_{i\mathbf{K}_i}(z')\right] \mathcal{I}_{AC} \exp\left(-iq_z|z-z'|\right) dz dz' \cdot \\
& \cdot \theta(E_i - E_j).
\end{aligned}
\tag{7.8}
$$

where M^{AC} is the deformation potential matrix, the exact form of the matrix depends on phonon mode and is given further, the $\mathcal{I}_{AC}$ term depends on the spin-flip process and the phonon mode [106, 107]. By replacing the order of the integration in Equation 7.8 the acoustic phonon relaxation rate is written as

$$
\begin{aligned}
\frac{1}{\tau_i^{AC}(\mathbf{K}_i)} =& \frac{4\pi k_B T}{\hbar \rho \upsilon^2} \sum_j \int_0^{2\pi} \frac{d\phi}{2\pi} \frac{1}{(2\pi)^2} \frac{\mathbf{K}_j}{\left|\dfrac{\partial E_j}{\partial \mathbf{K}_j}\right|} \left[1 - \frac{\left|\dfrac{\partial E(\mathbf{K}_j)}{\partial \mathbf{K}_j}\right| f(E(\mathbf{K}_j))}{\left|\dfrac{\partial E(\mathbf{K}_i)}{\partial \mathbf{K}_i}\right| f(E(\mathbf{K}_i))}\right] \cdot \\
& \cdot \int_0^t \int_0^t \left[\Psi_{j\mathbf{K}_j}^{\dagger}(z) M^{AC} \Psi_{i\mathbf{K}_i}(z)\right] \left[\Psi_{j\mathbf{K}_j}^{\dagger}(z') M^{AC} \Psi_{i\mathbf{K}_i}(z')\right] \cdot \\
& \cdot \int_{-\infty}^{\infty} \mathcal{I}_{AC} \exp\left(-iq_z|z-z'|\right) dq_z dz dz' \cdot \\
& \cdot \theta(E_i - E_j).
\end{aligned}
\tag{7.9}
$$

Intervalley g-Process Spin Relaxation. The g-process describes scattering between opposite valleys. Following [106, 107] the $\mathcal{I}_{AC} \equiv 1$ for intervalley scattering. By taking into account the Dirac delta function

$$
2\pi\delta(z-z') = \int_{-\infty}^{\infty} e^{-i(z-z')q_z} dq_z,
\tag{7.10}
$$

and applying the following property of the Dirac delta function

$$
\int dz' \left[\Psi_{j\mathbf{K}_j}^{\dagger}(z') M^{AC} \Psi_{i\mathbf{K}_i}(z')\right] \delta(z-z') = \Psi_{j\mathbf{K}_j}^{\dagger}(z) M^{AC} \Psi_{i\mathbf{K}_i}(z),
\tag{7.11}
$$

Equation 7.9 is simplified to [87]

$$
\frac{1}{\tau_i^{LA}(\mathbf{K}_i)} = \frac{4\pi k_B T}{\hbar \rho v_{LA}^2} \sum_j \int_0^{2\pi} \frac{d\phi}{2\pi} \frac{1}{(2\pi)^2} \frac{\mathbf{K}_j}{\left|\frac{\partial E_j}{\partial \mathbf{K}_j}\right|} \left[1 - \frac{\left|\frac{\partial E(\mathbf{K}_j)}{\partial \mathbf{K}_j}\right| f(E(\mathbf{K}_j))}{\left|\frac{\partial E(\mathbf{K}_i)}{\partial \mathbf{K}_i}\right| f(E(\mathbf{K}_i))} \right] \cdot
$$

$$
\cdot 2\pi \int_0^t \left[\Psi_{j\mathbf{K}_j}^\dagger(z) M^{AC} \Psi_{i\mathbf{K}_i}(z) \right] \left[\Psi_{j\mathbf{K}_j}^\dagger(z) M^{AC} \Psi_{i\mathbf{K}_i}(z) \right] dz \cdot
$$

$$
\cdot \theta(E_i - E_j), \tag{7.12}
$$

where $v_{LA} = 8700\frac{m}{s}$ [51], the matrix M^{AC} (for the intervalley g-process spin relaxation denote it by M') contains the Elliott and Yafet contributions [107] is written as

$$
M' = \begin{bmatrix} M_{ZZ} & M_{SO} \\ M_{SO}^\dagger & M_{ZZ} \end{bmatrix}, \tag{7.13}
$$

$$
M_{ZZ} = \begin{bmatrix} \Xi & 0 \\ 0 & \Xi \end{bmatrix}, \tag{7.14}
$$

$$
M_{SO} = \begin{bmatrix} 0 & D_{SO}(r_y - ir_x) \\ D_{SO}(-r_y - ir_x) & 0 \end{bmatrix}, \tag{7.15}
$$

where $\Xi = 12\text{eV}$ is the acoustic deformation potential, $(r_y, r_x) = \mathbf{K}_i + \mathbf{K}_j$, and $D_{SO} = 15\text{meV}/k_0$ [107] with $k_0 = 0.15 \cdot 2\pi/a$ which is defined as the position of the valley minimum relative to the X-point in unstrained silicon.

Intravalley Transversal Acoustic Phonons Spin Relaxation. Intrasubband transitions are important for the contributions determined by the shear deformation potential. The $\mathcal{I}_{AC}$ due to the transversal acoustic phonons is [106]

$$
\mathcal{I}_{AC} = \frac{\left(q_x^2 - q_y^2\right)^2}{q_x^2 + q_y^2} + \frac{4q_x^2 q_y^2 q_z^2}{\left(q_x^2 + q_y^2\right)|\mathbf{q}|^2}. \tag{7.16}
$$

Applying the theory of residues with $Q^2 = q_x^2 + q_y^2$, the following integral is calculated

$$
\int_{-\infty}^\infty \frac{q_z^2 e^{-iq_z|z-z'|}}{(Q^2 + q_z^2)^2} dq_z = \int_{-\infty}^\infty \frac{q_z^2 e^{-iq_z|z-z'|}}{(iQ - q_z)^2 (iQ + q_z)^2} dq_z =
$$

$$
= -2\pi i \left[\left(\frac{d}{dq_z} \frac{q_z^2 e^{-iq_z|z-z'|}}{(iQ - q_z)^2} \right) \Big|_{q_z = -iQ} \right] = \tag{7.17}
$$

$$
= \frac{\pi}{2} \frac{1 - Q|z - z'|}{Q} e^{-Q|z-z'|}.
$$

The matrix M^{AC} for the intrasubband transversal acoustic phonons (M) is written as

$$
M = \begin{bmatrix} 0 & 0 & \dfrac{D}{2} & 0 \\ 0 & 0 & 0 & \dfrac{D}{2} \\ \dfrac{D}{2} & 0 & 0 & 0 \\ 0 & \dfrac{D}{2} & 0 & 0 \end{bmatrix}.
\tag{7.18}
$$

Here $D=14\text{eV}$ is the shear deformation potential.

Then Equation 7.9 for the intrasubband transversal acoustic phonons is then written as

$$
\begin{aligned}
\frac{1}{\tau_i^{TA}(\mathbf{K}_i)} =& \frac{4\pi k_B T}{\hbar \rho v_{TA}^2} \sum_j \int_0^{2\pi} \frac{1}{2\pi} \frac{1}{(2\pi)^2} \frac{|\mathbf{K}_j|}{\left| \dfrac{\partial E(\mathbf{K}_j)}{\partial \mathbf{K}_j} \right|} \left[1 - \frac{\left| \dfrac{\partial E(\mathbf{K}_j)}{\partial \mathbf{K}_j} \right| f(E(\mathbf{K}_j))}{\left| \dfrac{\partial E(\mathbf{K}_i)}{\partial \mathbf{K}_i} \right| f(E(\mathbf{K}_i))} \right] \cdot \\
& \cdot \int_0^t \int_0^t \exp\left(-\sqrt{q_x^2 + q_y^2} |z - z'| \right) \cdot \\
& \cdot \frac{\pi}{2} \left[\Psi_{j\mathbf{K}_j-\sigma}^\dagger(z) M \Psi_{i\mathbf{K}_i\sigma}(z) \right]^\dagger \left[\Psi_{j\mathbf{K}_j-\sigma}^\dagger(z') M \Psi_{i\mathbf{K}_i\sigma}(z') \right] \cdot \\
& \cdot \left[\frac{4 q_x^2 q_y^2 \left(1 - |z - z'| \sqrt{q_x^2 + q_y^2} \right)}{\left(\sqrt{q_x^2 + q_y^2} \right)^3} \right] dz\, dz'\, d\varphi
\end{aligned}
\tag{7.19}
$$

where $\rho=2329\dfrac{kg}{m^3}$ is the silicon density [51], $v_{TA}=5300\dfrac{m}{s}$ is the transversal phonons' velocity, $(q_x, q_y) = \mathbf{K}_i - \mathbf{K}_j$.

Intravalley Longitudinal Acoustic Phonon Spin Relaxation. The $\mathcal{I}_{AC}$ due to the longitudinal acoustic phonon is given by [106]

$$
\mathcal{I}_{AC} = \frac{4 q_x^2 q_y^2}{|\mathbf{q}|^2}.
\tag{7.20}
$$

Applying theory of residues with $Q^2 = q_x^2 + q_y^2$, the following integral is calculated

$$
\begin{aligned}
\int_{-\infty}^\infty \frac{e^{-iq_z|z-z'|}}{(Q^2 + q_z^2)^2} dq_z &= \int_{-\infty}^\infty \frac{e^{-iq_z|z-z'|}}{(iQ - q_z)^2 (iQ + q_z)^2} dq_z = \\
&= -2\pi i \left[\frac{d}{dq_z} \left(\frac{e^{-iq_z|z-z'|}}{(iQ - q_z)^2} \right) \Big|_{q_z = -iQ} \right] = \\
&= \frac{\pi}{2} \frac{Q|z-z'| + 1}{Q^3} e^{-Q|z-z'|}.
\end{aligned}
\tag{7.21}
$$

The matrix M^{AC} for the intrasubband longitudinal acoustic phonons is the same as in Equation 7.18.

From this follows, the intravalley spin relaxation rate due to longitudinal acoustic phonons is calculated as [87]

$$
\begin{aligned}
\frac{1}{\tau_i^{LA}\left(\mathbf{K}_i\right)} = & \frac{4\pi k_B T}{\hbar \rho v_{LA}^2} \sum_j \int_0^{2\pi} \frac{1}{2\pi} \frac{1}{(2\pi)^2} \frac{|\mathbf{K}_j|}{\left|\dfrac{\partial E\left(\mathbf{K}_j\right)}{\partial \mathbf{K}_j}\right|} \cdot \\
& \cdot \left[1 - \frac{\left|\dfrac{\partial E\left(\mathbf{K}_j\right)}{\partial \mathbf{K}_j}\right| f\left(E\left(\mathbf{K}_j\right)\right)}{\left|\dfrac{\partial E\left(\mathbf{K}_i\right)}{\partial \mathbf{K}_i}\right| f\left(E\left(\mathbf{K}_i\right)\right)} \right] \cdot \\
& \cdot \int_0^t \int_0^t \exp\left(-\sqrt{q_x^2 + q_y^2}\,|z - z'|\right) \cdot \\
& \cdot \left[\Psi_{j\mathbf{K}_j-\sigma}^\dagger\left(z\right) M \Psi_{i\mathbf{K}_i\sigma}\left(z\right) \right]^* \left[\Psi_{j\mathbf{K}_j-\sigma}^\dagger\left(z'\right) M \Psi_{i\mathbf{K}_i\sigma}\left(z'\right) \right] \cdot \\
& \cdot \frac{\pi}{2} \frac{4 q_x^2 q_y^2}{\left(\sqrt{q_x^2 + q_y^2}\right)^3} \left[\sqrt{q_x^2 + q_y^2}\,|z - z'| + 1 \right] dz\,dz'\,d\varphi.
\end{aligned}
\tag{7.22}
$$

7.3 Spin Lifetime Calculations

The dependence of the spin lifetime on temperature for phonon scattering, and surface roughness scattering for different carrier concentrations is shown in Figure 7.9. The spin relaxation is more efficient for higher carrier concentrations for all three considered mechanisms. While the temperature increases, the difference between the spin lifetimes for different values of the electron concentration becomes less pronounced. Figure 7.9 also shows that the surface roughness mechanism dominates for all concentration values. Spin relaxation due to transversal acoustic phonons is the weakest among the three considered mechanisms.

Figure 7.10 demonstrates that the main contribution to spin relaxation comes from the intersubband processes due to the presence of the spin hot spots characterized by the sharp peaks of the intersubband spin relaxation matrix elements. Their position is shown in Figure 7.11. For higher shear strain values the hot spots are pushed to higher energies, away from the subband minima (inset in Figure 7.11). This results in a strong increase of the spin lifetime with shear strain for surface roughness and the phonon mechanisms as shown in Figure 7.12.
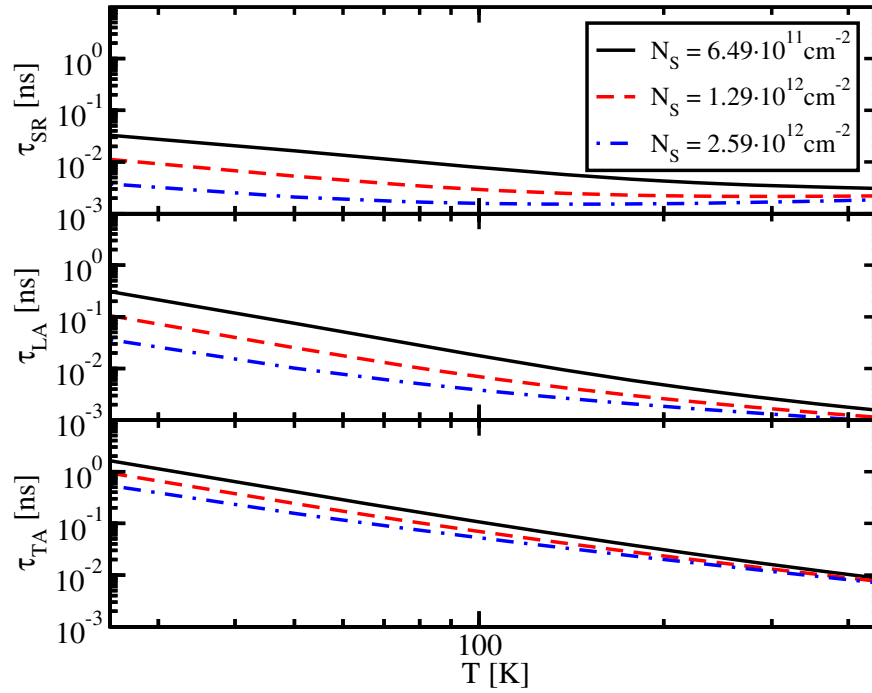
Figure 7.9: Dependence of the surface roughness (SR), the longitudinal phonons' (LA), and the transversal phonons' (TA) contribution to the spin lifetime on temperature for different values of the electron concentration, for $\varepsilon_{xy}=0$, and film thickness 2.1nm.
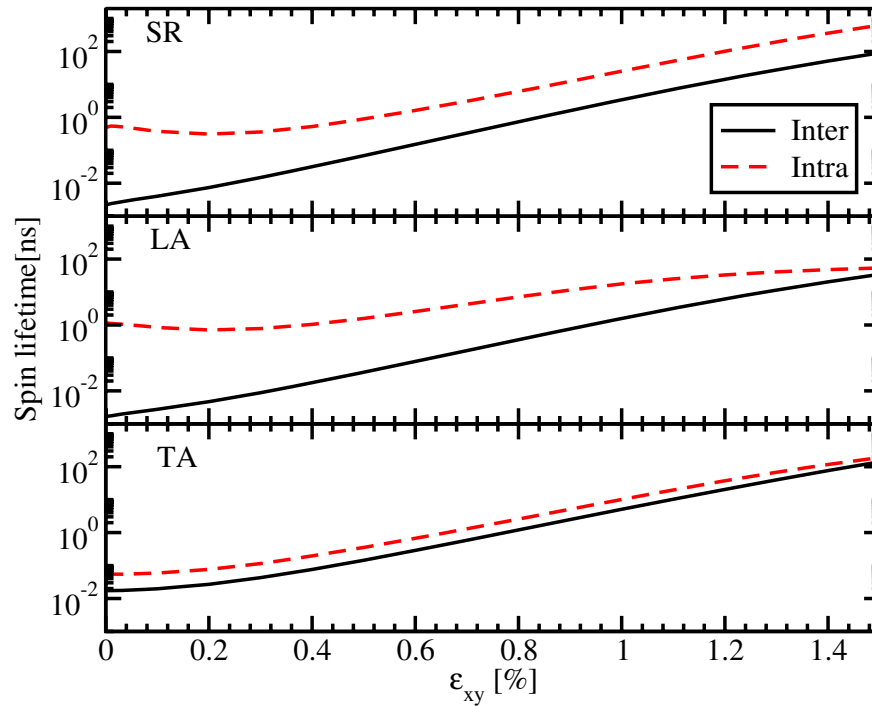
Figure 7.10: Dependence of the intersubband and intrasubband components of the momentum relaxation time induced by surface roughness (SR) and acoustic phonons (PH) on shear strain for the film thickness 1.36nm, $T=300$K, and electron concentration $1.29\cdot10^{12}$cm^{-2}.
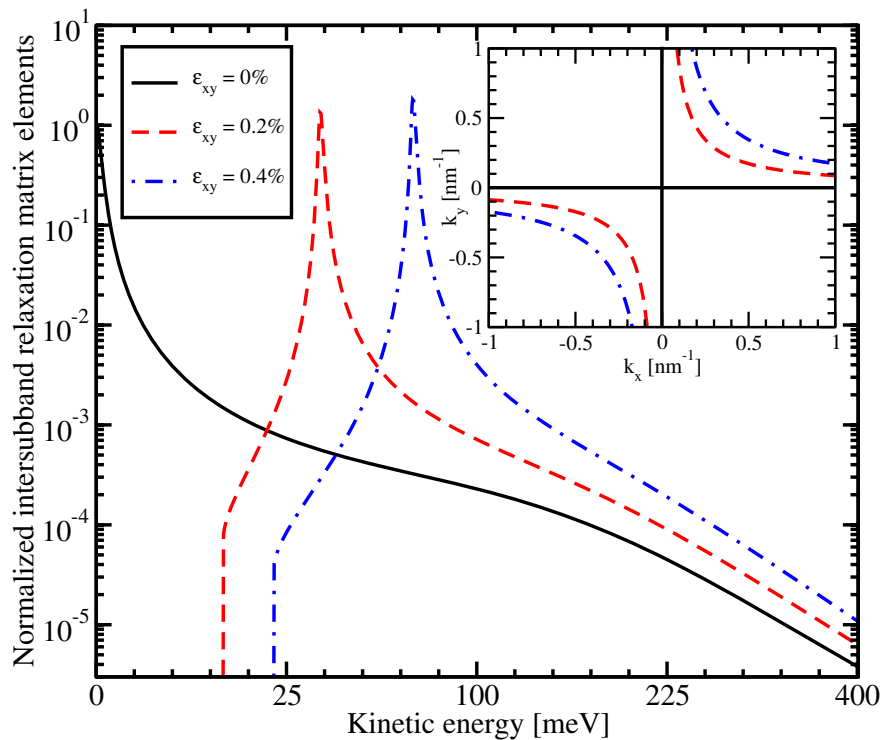
Figure 7.11: Normalized intersubband relaxation matrix elements as a function of the conduction electrons kinetic energy in [110] direction. The inset shows the positions of the hot spots for different values of shear strain.
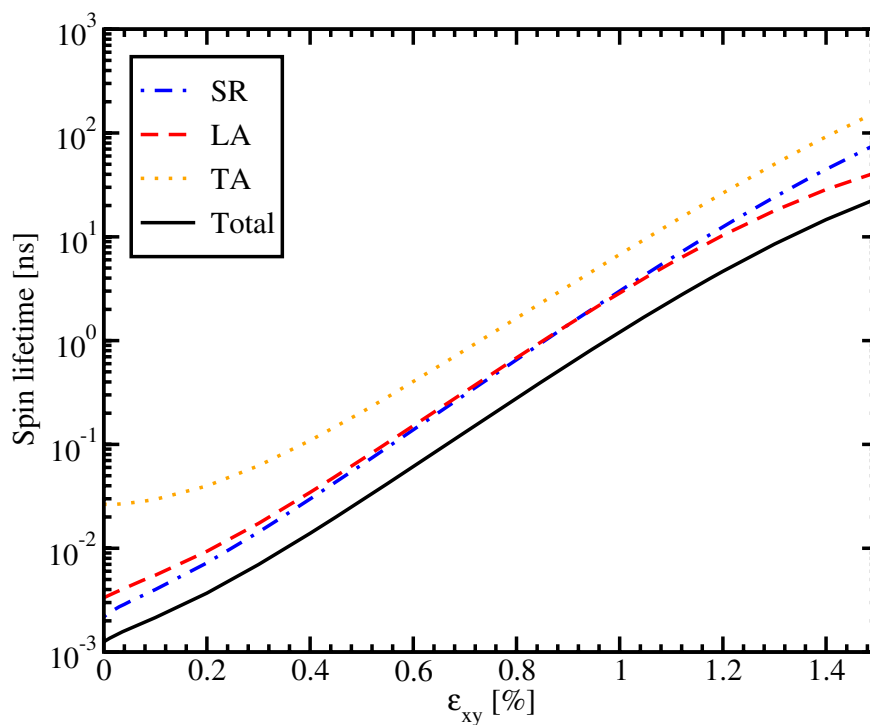
Figure 7.12: Dependence of the spin lifetime on shear strain for the film thickness 2.1nm, T=300K, and electron concentration $1.29 \cdot 10^{12}$cm^{-2}.
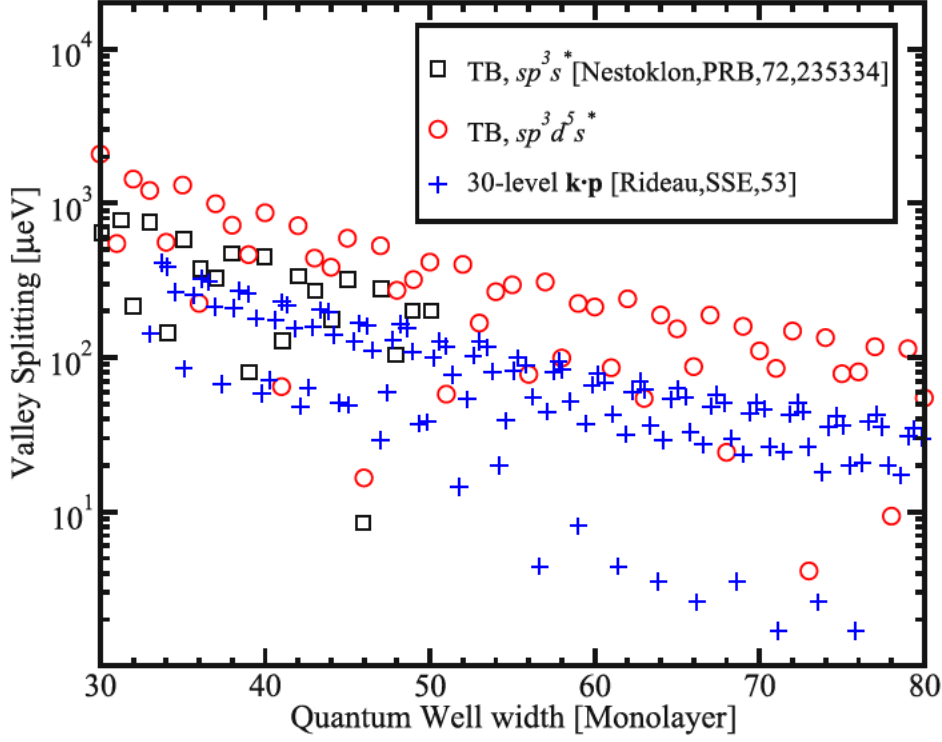
Figure 7.13: Valley splitting in a Si quantum well at zero strain as a function of the quantum
well width including results from literature [70, 107].

7.4 Valley Splitting in Unstrained Films

The [001] equivalent valley coupling through the Γ-point results in a subband splitting
in confined electron structures [5]. The values of the valley splitting obtained from
a 30-band **k·p** model [97], an atomistic tight-binding model [82], and $sp^3d^5s^*$ code
are shown in Figure 7.13. Although looking irregular, the results follow a certain
law. Figure 7.14 demonstrates a good agreement of the results of the tight-binding
calculations with the analytical expression for the subband splitting [111]

$$\Lambda_\Gamma = \frac{2\pi\Delta_\Gamma}{(k_0 t)^3}\sin(k_{0\Gamma}t), \qquad (7.23)$$

where Δ_Γ is the splitting at Γ point, $k_{0\Gamma} = 0.85\frac{2\pi}{a}$, a is the lattice constant, and t is
the film thickness. The good agreement is found for the value $\Delta_\Gamma{=}5.5\text{eV}$.

Figure 7.15 shows the dependence of the lowest unprimed subbands energies and their
splitting on shear strain with and without accounting for the Λ_Γ term. The unprimed
subbands are degenerate at zero strain without the Λ_Γ term. The Λ_Γ term lifts the
degeneracy while shear strain gives the major contribution to the splitting at high
strain values. The surface roughness scattering matrix elements are taken to be pro-
portional to the square of the product of the subband wave function derivatives at
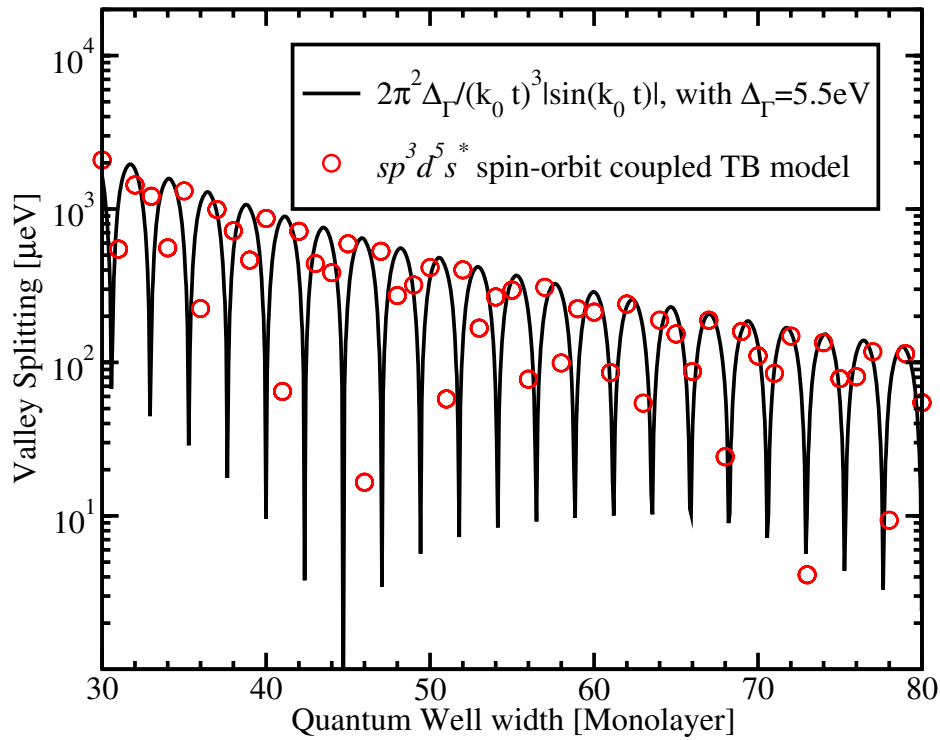
Figure 7.14: Dependence of the valley splitting on the quantum well width from the tight binding (TB) model and the analytical expression with Λ_Γ=5.5eV.
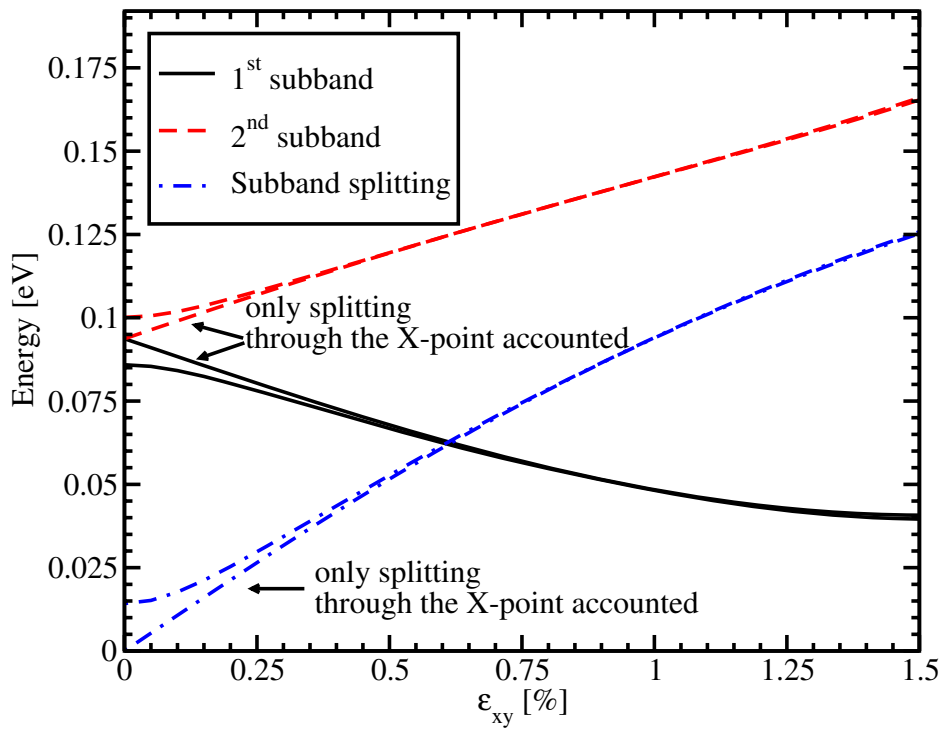
Figure 7.15: Dependence of energy of the 1st and the 2nd subband together with the subband splitting on shear strain for the film thickness of 2.1nm.
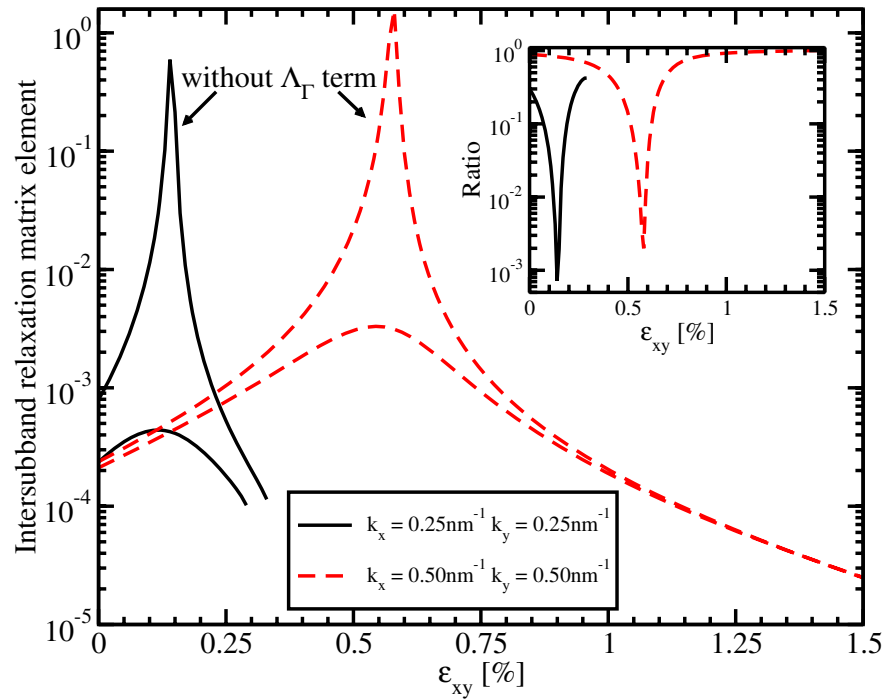
Figure 7.16: Dependence of the normalized intersubband relaxation matrix elements on shear strain for 2.1nm film thickness. The inset shows the ratio of the matrix elements with the Λ_Γ term to the matrix elements without the Λ_Γ term.
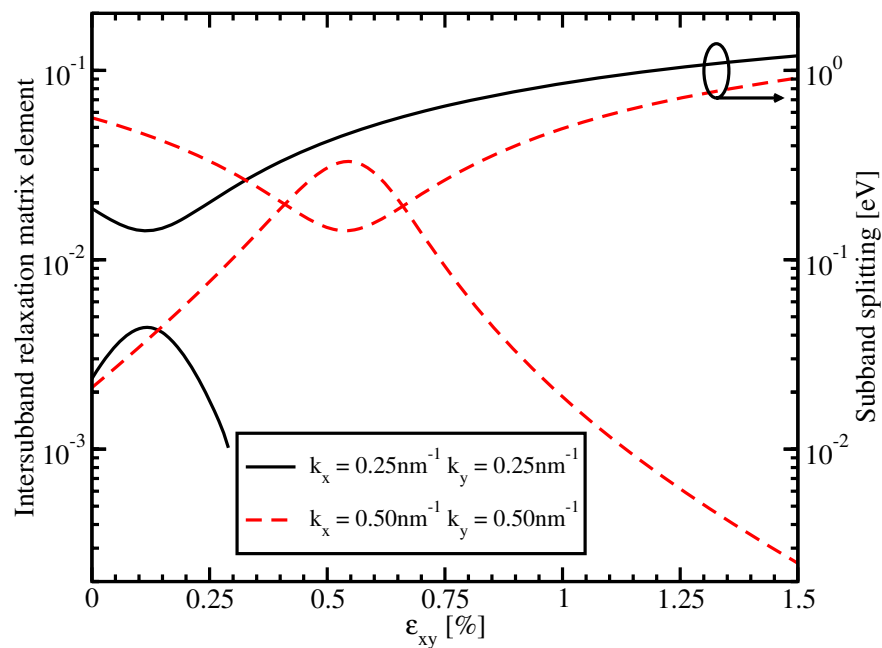
Figure 7.17: Normalized intersubband relaxation matrix elements and subband splitting as a function of shear strain calculated with taking into account zero-strain splitting.
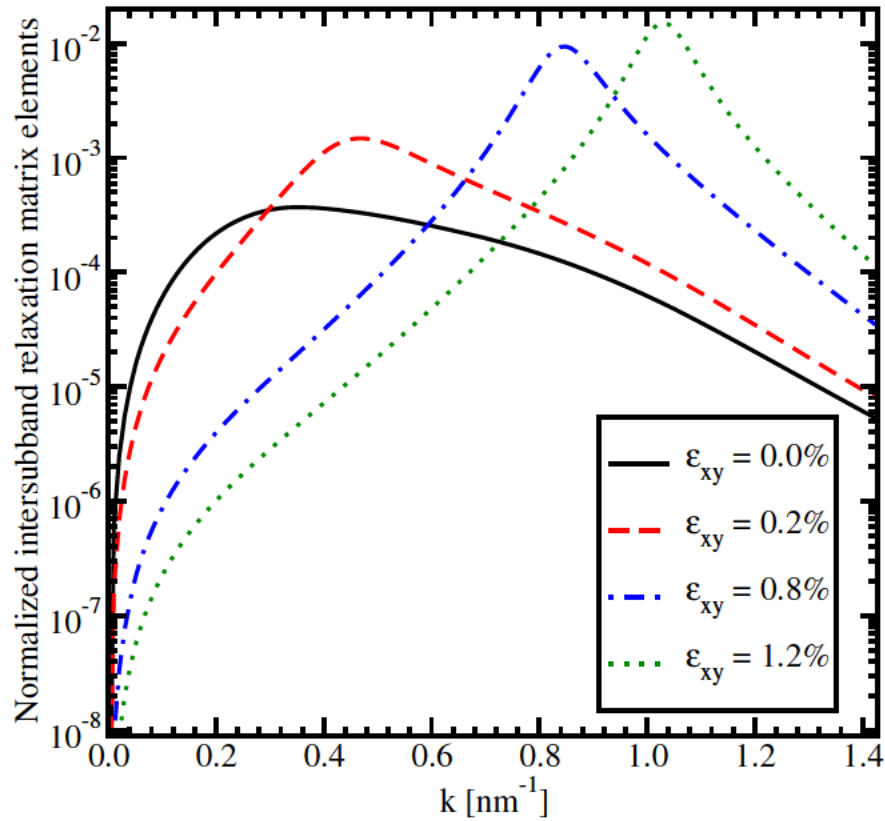
Figure 7.18: Normalized intersubband spin relaxation matrix elements as a function of the wave vector in [110] direction.
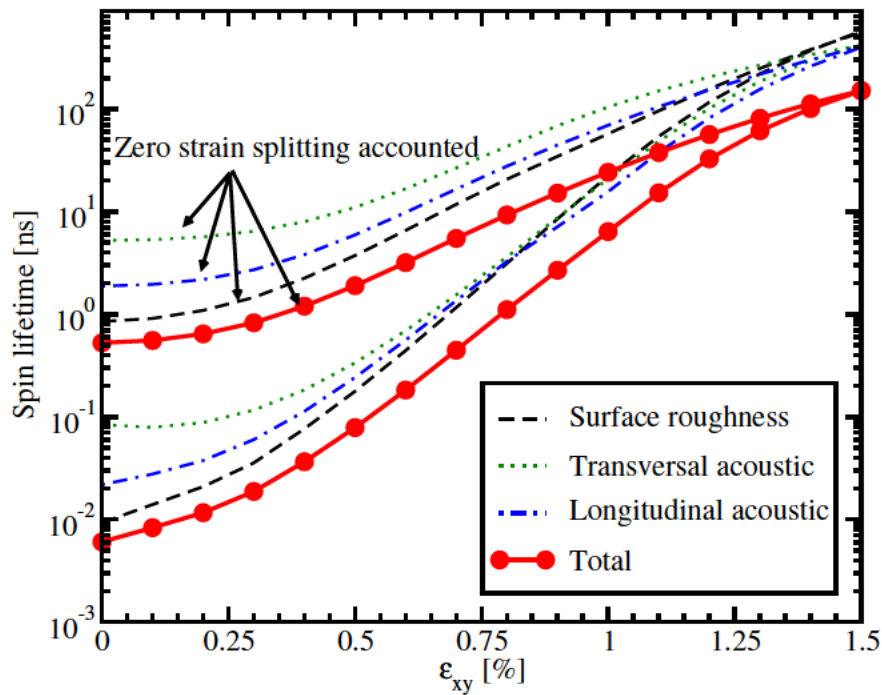
Figure 7.19: Dependence of spin lifetime on shear strain for $T=300$K and a film thickness of 2.1nm.

the interface [35]. The electron-phonon scattering is accounted for by the deformation potential approximation [87]. The surface roughness intersubband spin relaxation matrix elements with and without the Δ_Γ term are shown in Figure 7.16. The difference in the matrix elements' values calculated with and without the Δ_Γ term (inset Figure 7.16) can reach two orders of magnitude. Hence, the valley coupling through the Γ-point must be taken into account for the accurate spin lifetime calculations.

The hot-spot peaks shown in Figure 7.11 becomes smoother if the Γ-point splitting is considered (Figure 7.18). However, the peaks are still well-pronounced and follow the same trend.

The peaks on the matrix elements' dependences (Figure 7.16) are correlated with the unprimed subband splitting minima (Figure 7.17). For higher strain values the peaks corresponding to strong spin relaxation hot spots are pushed towards unoccupied states at higher energies (Figure 7.17). This leads to the strong increase of the spin lifetime demonstrated in Figure 7.19. The increase is less pronounced, if the Λ_Γ term responsible for the valley splitting in relaxed films is taken into account. However, even in this case the spin lifetime is boosted by almost two orders of magnitude.

7.5 Primed Subbands and f-Processes

7.5.1 Primed k·p Hamiltonian

The primed subbands are governed by the following Hamiltonian [111]

$$H' = \left[\begin{array}{cc} H'_1 & H'_3 \\ H'_3 & H'_2 \end{array} \right], \tag{7.24}$$

where H'_1, H'_2, and H'_3 are written as

$$H'_1 = \left[\begin{array}{cc} \frac{\hbar^2 k_z^2}{2m_l} + \frac{\hbar^2\left(k_x^2 + k_y^2\right)}{2m_t} - \frac{\hbar^2 k_x k_y}{M} + U(z) & 0 \\ 0 & \frac{\hbar^2 k_z^2}{2m_l} + \frac{\hbar^2\left(k_x^2 + k_y^2\right)}{2m_t} - \frac{\hbar^2 k_x k_y}{M} + U(z) \end{array} \right], \tag{7.25}$$

$$H'_2 = \left[\begin{array}{cc} \frac{\hbar^2 k_z^2}{2m_l} + \frac{\hbar^2\left(k_x^2 + k_y^2\right)}{2m_t} + \frac{\hbar^2 k_x k_y}{M} + U(z) & 0 \\ 0 & \frac{\hbar^2 k_z^2}{2m_l} + \frac{\hbar^2\left(k_x^2 + k_y^2\right)}{2m_t} + \frac{\hbar^2 k_x k_y}{M} + U(z) \end{array} \right], \tag{7.26}$$

$$H'_3 = \left[\begin{array}{cc} \frac{\hbar^2 k_z k_0}{m_l} & 0 \\ 0 & \frac{\hbar^2 k_z k_0}{m_l} \end{array} \right]. \tag{7.27}$$

A quantization along X-axis is assumed.

7.5.2 f-Process Relaxation Rate

The f-process describes scattering between valleys that reside on perpendicular axes. The spin relaxation is calculated by [35]

$$
\frac{1}{\tau_i^{(fp)}(\mathbf{K}_i)} = \frac{4\pi 3 d_0}{\hbar^2 \rho a^2 \omega_{op}} \sum_j \int_0^{2\pi} \frac{d\phi}{2\pi} \int_{-\infty}^{\infty} \frac{dq_z}{(2\pi)^2} \frac{\mathbf{K}_j}{\left|\frac{\partial E_j}{\partial \mathbf{K}_j}\right|} \cdot
$$

$$
\cdot \left[1 - \frac{\left|\frac{\partial E(\mathbf{K}_j)}{\partial \mathbf{K}_j}\right| f(E(\mathbf{K}_j))}{\left|\frac{\partial E(\mathbf{K}_i)}{\partial \mathbf{K}_i}\right| f(E(\mathbf{K}_i))}\right] \left(n_{op} + \frac{1}{2} \pm \frac{1}{2}\right) \cdot \tag{7.28}
$$

$$
\cdot \sum_\alpha \left| e_\alpha^{(op)}(\mathbf{q}) \sum_{\nu,\mu} D_{\alpha\beta}^{(\nu,\mu)} \int_0^t dz \Psi_{\mu\mathbf{K}_j}^*(z) \exp(-iq_z z) \Psi_{\nu\mathbf{K}_i}(z)\right|^2 \cdot
$$

$$
\cdot \theta(E_i - E_j \pm \hbar\omega_{op}),
$$

a defines the silicon lattice constant, d_0 is the optical deformation potential, ω_{op} denotes the frequency of the optical phonons, and n_{op} describes the Bose occupation factor

$$
n_{op} = \frac{1}{e^{\left(\frac{\hbar\omega_{op}}{k_B T}\right)} - 1}. \tag{7.29}
$$

The relaxation rate for the transition between primed and unprimed subbands is given by [35]

$$
\frac{1}{\tau_i^{OP}(\mathbf{K}_i)} = \frac{2\pi}{\rho\omega_{op}} \sum_j \rho_j(E_i \mp \hbar\omega_{op}) \int_0^t \left|\Psi_{j\mathbf{K}_j}^\dagger(z) M^{OP} \Psi_{i\mathbf{K}_i}(z)\right|^2 dz \cdot
$$

$$
\cdot \frac{1 - f(E(\mathbf{K}_i) \mp \hbar\omega_{op})}{1 - f(E(\mathbf{K}_j))} \left(n_{op} + \frac{1}{2} \pm \frac{1}{2}\right), \tag{7.30}
$$

$\rho_j(E)$ is the density of states for subband j and M^{OP} is written as

$$
M^{OP} = \begin{bmatrix} 0 & D_{op} & 0 & D_{op} \\ D_{op} & 0 & D_{op} & 0 \\ 0 & D_{op} & 0 & D_{op} \\ D_{op} & 0 & D_{op} & 0 \end{bmatrix} \tag{7.31}
$$

with $D_{op} = 6.5\text{meV}\frac{2\pi}{a}$ [107].
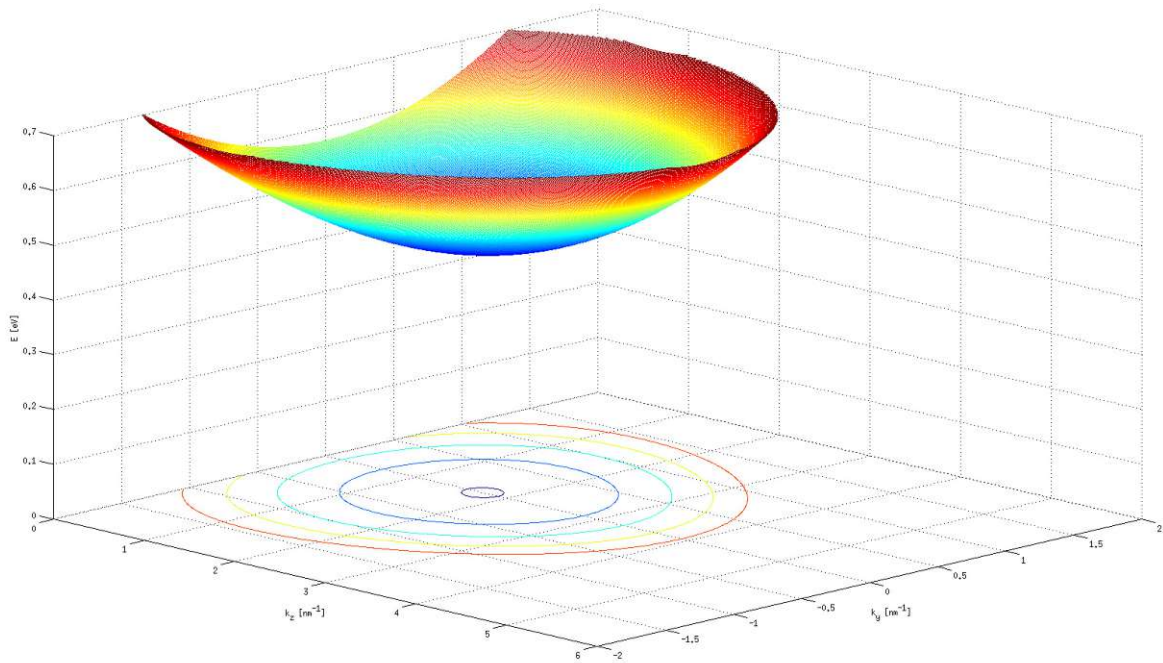
Figure 7.20: Energy dispersion for the primed subband for 2.1nm film thickness.
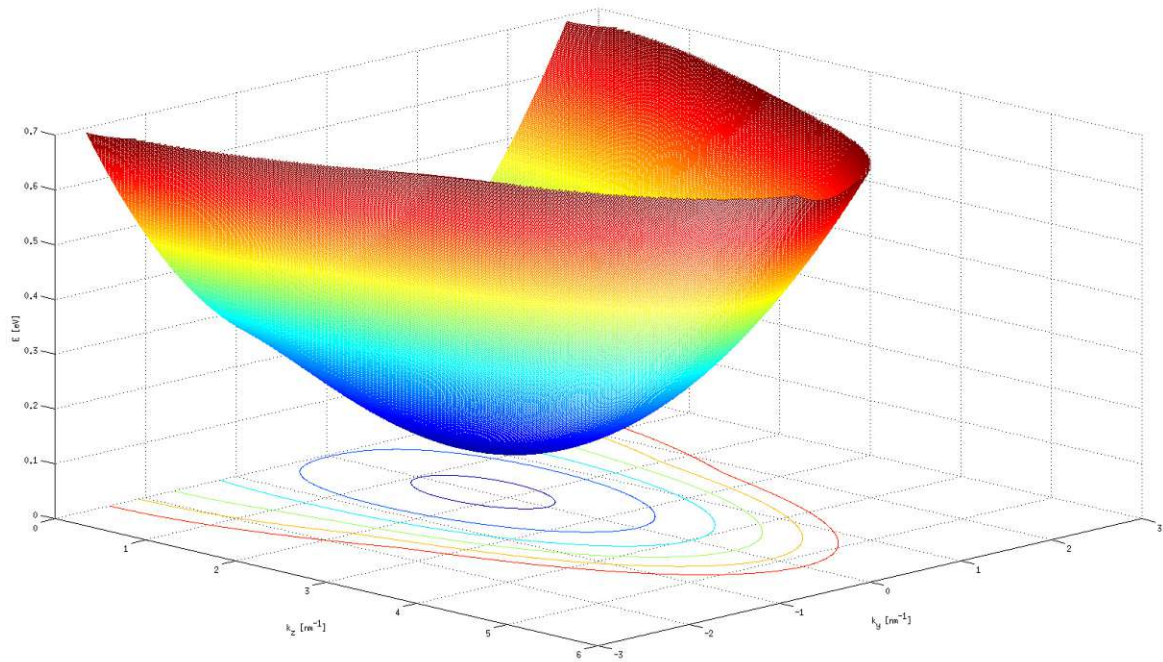
Figure 7.21: Energy dispersion for the primed subband for 5nm film thickness.
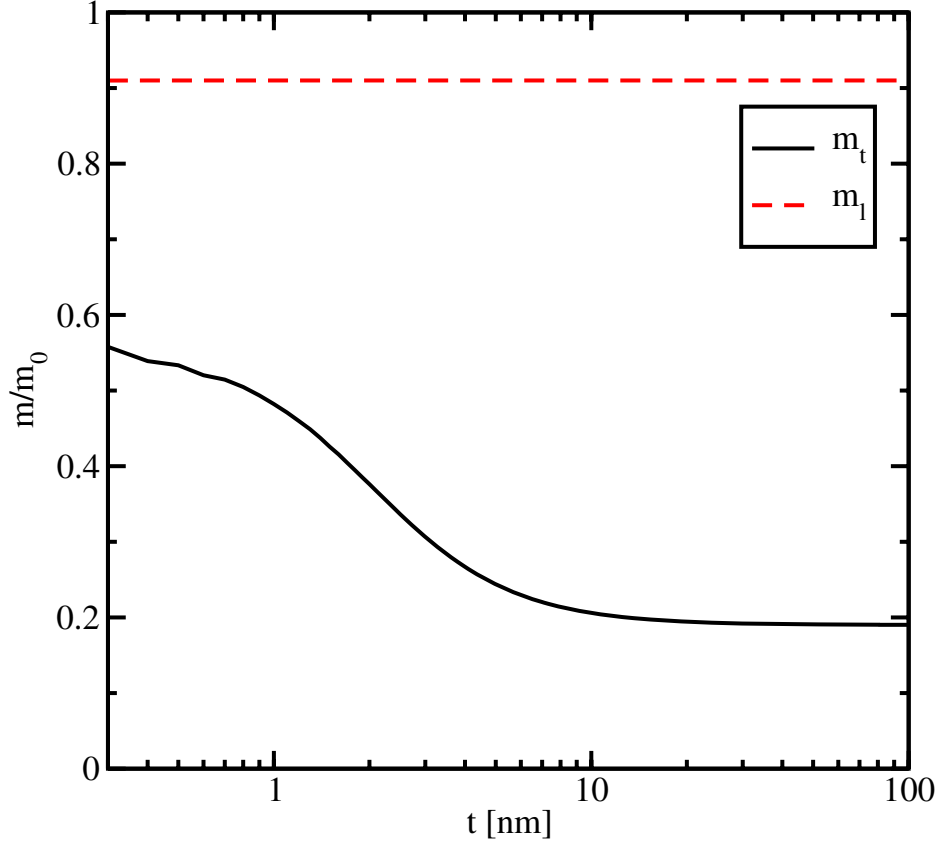
Figure 7.22: Dependence of the effective mass for the lowest ground subband on thickness.

7.6 Results

In Figure 7.20 and Figure 7.21 the dispersion of the first primed subband in films with thicknesses of 2.1nm and 5nm, respectively, is compared. The minimum energy of the subband is located at the point $k_z = k_0$, $k_y = 0$, and its value for an infinite potential square well is determined by

$$E = \frac{\pi^2 \hbar^2}{2 m_t t^2}. \tag{7.32}$$

The values of the subband minima for the well thickness of 2.1nm and 5nm are 0.44eV and 0.08eV, respectively. These values are in good agreement with Figure 7.20 and Figure 7.21.

The dependence of the longitudinal and transversal effective masses on the well thickness is shown in Figure 7.22. The longitudinal effective mass $m_l = 0.91 m_0$ does not depend on the thickness. In sharp contrast, the effective mass m_t shows a strong increase as the film thickness reduces, in agreement with earlier predictions [111].

Figure 7.23 and Figure 7.24 show the total spin lifetime and contributions due to acoustic, optical phonons, and surface roughness as a function of strain for two different
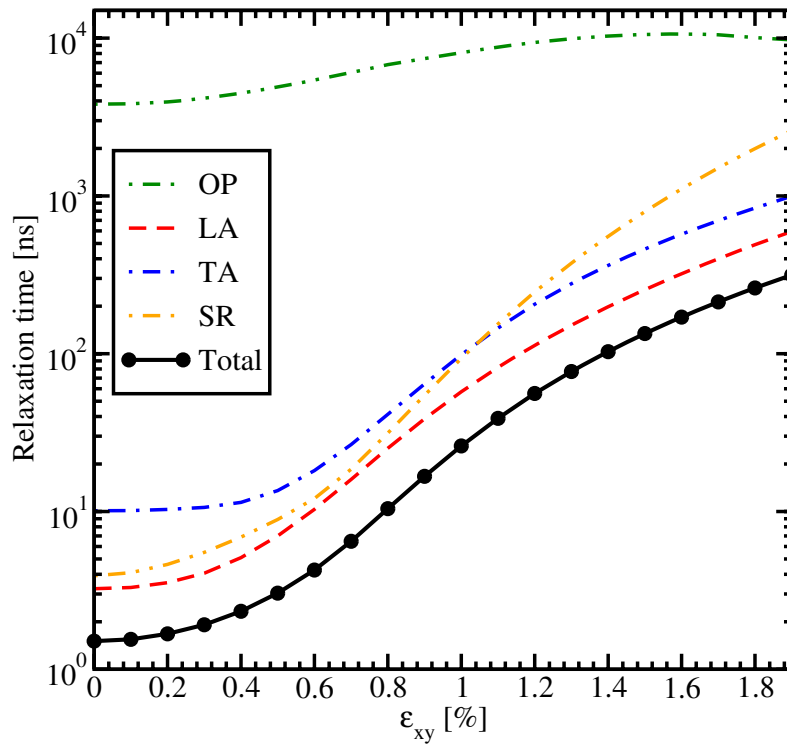
Figure 7.23: Spin lifetime as a function of strain for 3nm film thickness and an electron concentration of $5 \cdot 10^{12} cm^{-2}$. Contributions due to optical, acoustic and surface roughness are included.
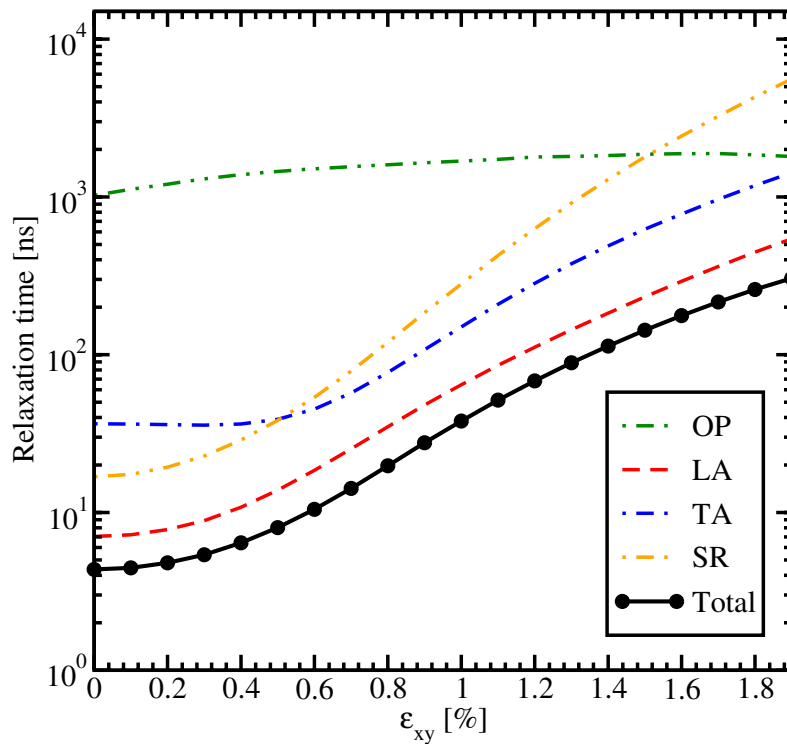
Figure 7.24: Spin lifetime as a function of strain for 4nm film thickness and an electron concentration of $5 \cdot 10^{12} cm^{-2}$. Contributions due to optical, acoustic and surface roughness are included.
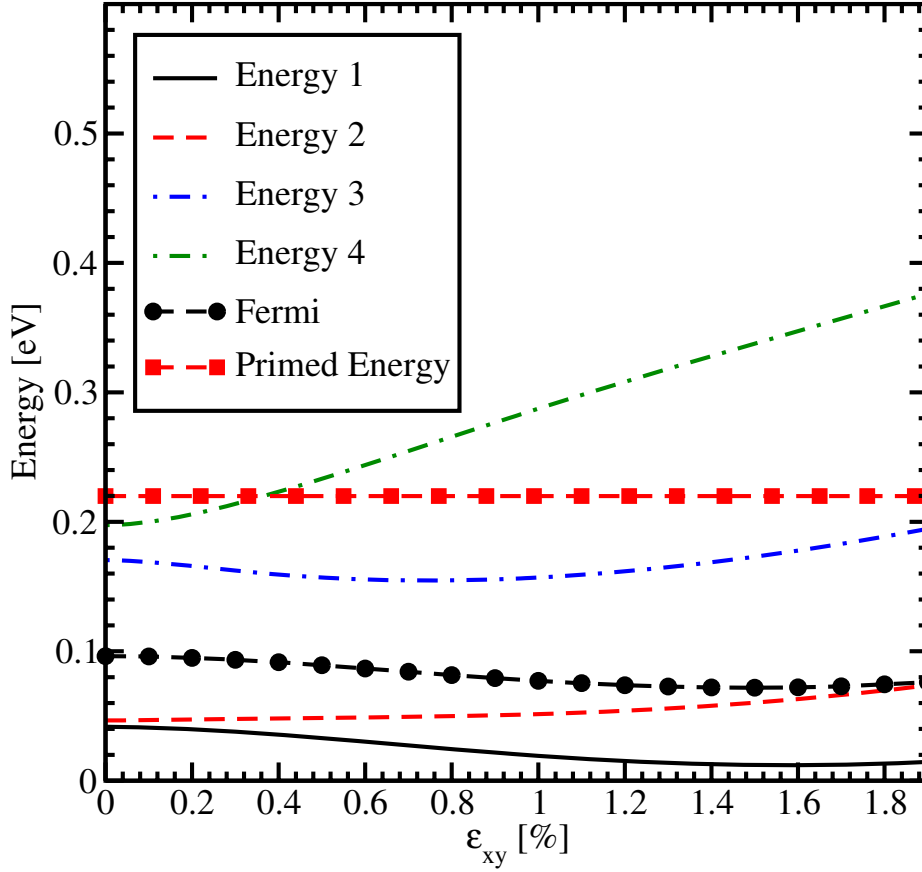
Figure 7.25: Dependence of energies for primed, unprimed subbands, and Fermi energy on strain for 3nm film thickness.

thicknesses (3nm and 4nm). For the film of 3nm thickness the contribution due to longitudinal acoustic phonons (LA) is close to the contribution from surface roughness for small shear strain values. Further increase of strain makes LA phonons the main contributors to the total spin lifetime. For the thicker film shown in Figure 7.24 the total spin lifetime mainly follows the same trend as the longitudinal acoustic phonons spin relaxation. Interestingly, the intersubband optical phonons calculated as g-process can be safely ignored for the film of 3nm thickness, while their contribution for the film of 4nm thickness is more considerable. The dependence of g-process phonons on strain is not so significant as the surface roughness, intrasubband scattering, and f-process scattering. Thus, for thicker films the effect of several orders of magnitude increase of spin lifetime in strained films should not be observed.

The dependence of energies for primed and unprimed subbands on strain for $k_x = 0$ and $k_y = 0$ together with the Fermi energy is shown in Figure 7.25 and Figure 7.26 for 3nm and 4nm, respectively. *Energy 1* and *Energy 2* stand for the lowest subbands of the two opposite valleys along [001] direction. *Energy 3* and *Energy 4* stand for the second unprimed subbands. The increasing importance of the g-process shown in Fig-
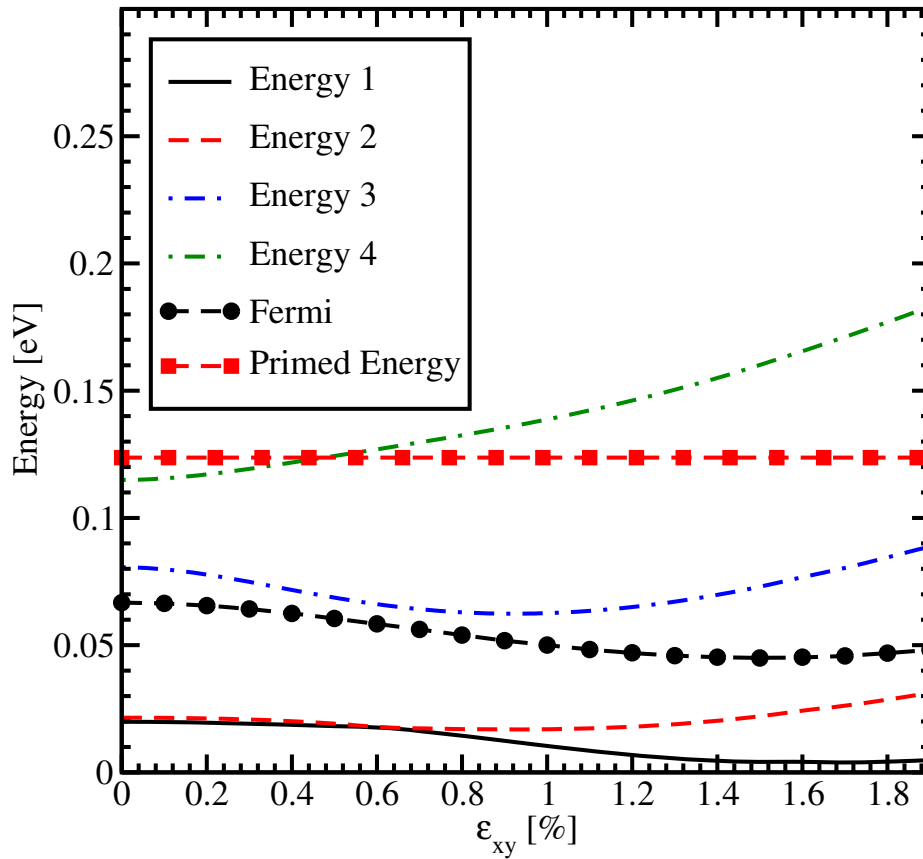
Figure 7.26: Dependence of energies for primed, unprimed subbands, and Fermi energy on strain for 4nm film thickness.

ure 7.24 compared to Figure 7.23 comes from the fact that the distance between the Fermi energy and the lowest energy in the primed subband decreases with thickness increasing. The occupation of the second subband become less pronounced at high strain as is confirmed by the Fermi level dependence for both thickness values (Figure 7.25 and Figure 7.26).

8 Spin Field-Effect Transistor

The spin field-effect transistor (SpinFET) is a future semiconductor spintronics device promising to deliver a performance superior to that achieved with present transistor technology. A schematic illustration of the SpinFET is shown in Figure 8.1. SpinFETs are composed of two ferromagnetic contacts (source and drain), which sandwich the semiconductor region. Ferromagnetic contacts contain mostly spin-polarized electrons and play the role of polarizer and analyzer as described by Datta and Das [22]. The ferromagnetic source contact injects spin-polarized electrons into the semiconductor region. Because of the non-zero spin-orbit interaction the electron spin precesses during the propagation through the channel [14, 72]. At the drain contact only the electrons with spin aligned to the drain magnetization can easily leave the channel and contribute most to the current. Thus, the total current through the device depends on the relative angle between the magnetization direction of the drain contact and the electron spin polarization at the end of the semiconductor channel. Current modulation is achieved by tuning the strength of the spin-orbit interaction in the semiconductor region and thus the degree of the spin precession. Importantly, the strength of the spin-orbit interaction in the channel depends on the effective electric field and can be controlled by the voltage applied to the gate [28, 42, 44, 46, 74, 84, 101, 129].

The spin precession angle $\Delta\theta$ defined as the difference between the orientation of the spin of the electron at the end and at the beginning of the semiconductor region is [109]

$$\Delta\theta = \frac{2\alpha m^*}{\hbar^2}t,\tag{8.1}$$

where α is the strength of the spin-orbit interaction, m^* is the effective mass of the electron, $\hbar$ is the reduced Planck constant, and t is the length of the semiconductor
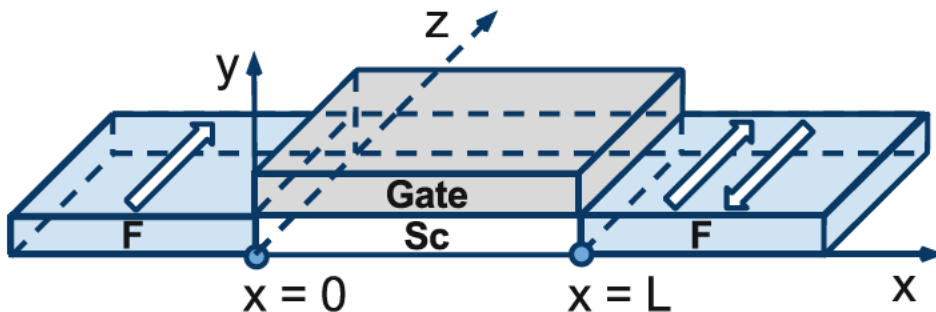
Figure 8.1: Schematic illustration of the spin field-effect transistor.

channel. In the absence of spin-orbit interaction and external magnetic field the electrons propagate with their spin orientation conserved. The strength of the spin-orbit interaction determines the minimum length of the semiconductor channel, which will be required to change the orientation of the spin to its opposite direction. Therefore, a tradeoff between spin lifetime and spin-orbit strength for sufficiently short channel needs to be found. Thus, in case of a material with a strong spin-orbit interaction such as InAs the semiconductor channel will be shorter than for a material with the weaker spin-orbit interaction such as silicon.

Large spin lifetime in silicon was shown in the previous chapters. Due to the excellence experience, and vast knowledge related to silicon and CMOS technology it is very attractive to investigate spin-based switching devices with silicon as a channel material. In order to relate the performance of silicon, InAs is studied as well.

8.1 Spin Transport

Spin transport plays the same important role in spin electronics as a charge transport in the traditional electronics. Spin-dependent scattering, spin diffusion, and spin injection through an interface, and control of the spin by magnetic field are the questions spintronics considers. Spin polarization can be achieved by optical spin excitation with circularly polarized light [67,76,81,91] and a current flowing from a ferromagnetic material into a non-magnetic material [19,59,77].

The intrinsic peculiarities of an ordinary ferromagnet lead to different conductivities for the two groups of electrons, parallel and anti-parallel to the magnetization direction of the ferromagnet. The current through the ferromagnet can be considered as spin polarized. In other words, the current of the spin up electrons ($I_\uparrow$) is not equal to the current of the spin-down electrons ($I_\downarrow$) as shown in Figure 8.2.

To effectively operate SpinFETs, the into the semiconductor injected spin-polarized current should preserve inequality between $I_\uparrow$ and $I_\downarrow$. To fulfill the condition that electrons mostly preserve their spin the transport time (τ_{tr}) should be much less compare to the spin relaxation time (τ_s)

$$\tau_s \ll \tau_{tr}. \tag{8.2}$$

The characteristic length of spin propagation in a semiconductor is determined by [37, 102, 121, 134, 135]

$$L_s = \sqrt{D_s \tau_s}, \tag{8.3}$$

where D_s is the diffusion coefficient.

However, it is hard to achieve high spin injection efficiency in a ferromagnet/semiconductor junction. The problem is known as the conduction impedance mismatch
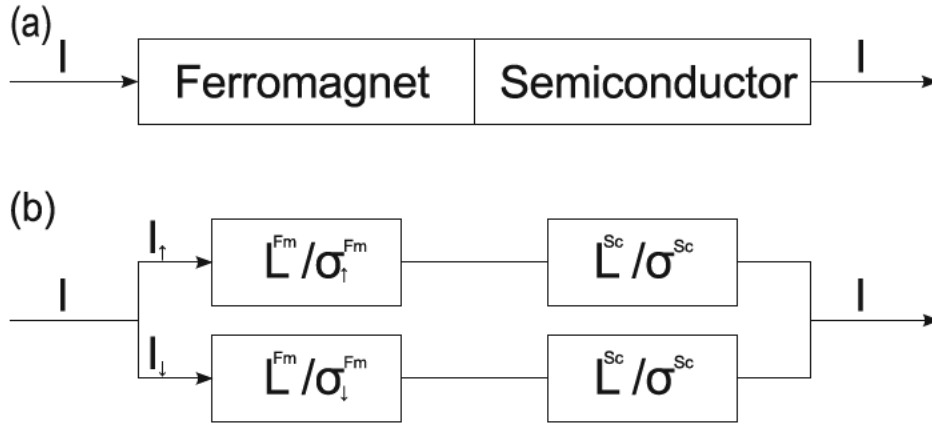
Figure 8.2: (a) a schematic illustration of the spin injection from a ferromagnet (ferromagnetic material) to a semiconductor through the ohmic junction. (b) equivalent scheme of the ferromagnetic/semiconductor contact represented as a parallel connection of the resistances. Upper part represents spin-up polarized electrons, bottom part - spin-down electrons.

problem [32, 57, 96, 103, 109]. The problem comes from the big difference between the semiconductor and ferromagnet conductions. Experiments [33] showed that the electrical injection of spin-polarized electrons in a semiconductor is not efficient. Authors stated that despite all their efforts, they have not been able to observe spin injection [33]. A physical explanation of that problem is given in [58, 102]. In Figure 8.2 (b) an equivalent circuit for up-down current in a ferromagnetic/semiconductor junction is shown. Each region of the junction is characterized by its own effective resistance, determined by the spin diffusion lengths in the bulk regions, or by the spin-dependent conductances in the contact [31, 60].

Following [31] the effective resistance of the ferromagnetic R^{Fm} and semiconductor R^{Sc} regions are introduced. The effective resistance is not equal to the electrical resistance of the region, it appears in the spin-polarized transport and is roughly equal to the actual resistance of the region of size L^{Fm} (L^{Sc}) [31]

$$R^{Fm} \equiv \frac{L^{Fm}}{\sigma_{\uparrow,\downarrow}^{Fm}}, \tag{8.4}$$

$$R^{Sc} \equiv \frac{L^{Sc}}{\sigma^{Sc}}, \tag{8.5}$$

where $\sigma_{\uparrow,\downarrow}^{Fm}(\sigma^{Sc})$ is the conductivity of the ferromagnetic (semiconductor) region. The spin injection coefficient is determined by

$$\gamma = \frac{I_\uparrow - I_\downarrow}{I_\uparrow + I_\downarrow}. \tag{8.6}$$

The observed low values of γ are the consequence of a big difference in conductivity between the ferromagnet and the semiconductor in the ferromagnet/semiconductor junction [102]. Indeed, if the following inequality

$$R^{Fm}_{\uparrow,\downarrow} \ll R^{Sc} \tag{8.7}$$

is true then $I_\uparrow$ and $I_\downarrow$ are practically the same. Thus, no spin injection is observed. There are two approaches to overcome this problem: 1) instead of an metallic ferromagnet use a ferromagnetic semiconductor that has a resistivity almost equal to the resistivity of the semiconductor ($R^{Fm}_{\uparrow,\downarrow} \approx R^{Sc}$); 2) use of a normal metallic ferromagnet but ensure a very high junction resistance (R_c) [31, 96]

$$R_c > R^{Sc}. \tag{8.8}$$

To fulfill Equation 8.8 a thin insulating tunnel barrier was introduced in [80]. The authors approach was to use AlO_x insulator as a tunnel barrier between the ferromagnetic layer and the (AlGa)As semiconductor heterostructure [80]. Under this conditions the current in semiconductor becomes spin-polarized. The success of the first experiment made by Alvarado [4] was because of the use of a tunneling microscope. Electrical spin injection from a ferromagnetic semiconductor into a non-magnetic semiconductor was experimentally demonstrated in [75, 85]. In [85] electrical spin injection into a non-magnetic semiconductor is achieved by using a p-type ferromagnetic semiconductor GaMnAs as the spin polarizer. In [75] the successful spin-polarized current injection from a GaMnAs ferromagnetic electrode into a GaAs layer through an AlAs barrier was demonstrated.

Another approach to resolve the conductivity mismatch problem is to apply half-metallic materials. Inomata [50] demonstrated giant tunneling magnetoresistance at room temperature for magnetic tunnel junctions using Co-based full-Heusler alloys. The attractive property of half-metallic materials is that the spin polarization can achieve values up to 100% [12, 23, 92, 108]. A number of researches considered applying half-metallic materials for spintronics application [20, 100, 110, 113]

8.2 Effective Spin-Orbit Hamiltonian

In order to make it possible to distinguish electrons in quantum structures with the same wave vector and opposite spins the electrons should have a different energy. In the absence of a magnetic field, the degeneracy is only lifted in systems without a center of inversion. There are two important reasons for the absence of a center of inversion. The first reason is the absence of a center of inversion in the bulk materials that have been used for the quantum structures. The Bulk Inversion Asymmetry (BIA) is usually present in III-V structures, while in diamond-like semiconductors (Si

and Ge) a BIA is absent [43]. The Hamiltonian of the spin-orbit interaction for 2D III-V [001]-oriented structures is written as [24]

$$\mathcal{H}_{BIA}(\mathbf{k}) = \beta(\sigma_x k_x - \sigma_y k_y), \tag{8.9}$$

where $\sigma_{x,y}$ - are the Pauli matrices defined in Equation 4.46 and Equation 4.47. Equation 8.9 is called the 2D Dresselhaus effective spin-orbit interaction.

The second mechanism that leads to a non-centrosymmetric structure is the Structure Inversion Asymmetry (SIA). The nature of the SIA is that the two opposite directions along the direction of growth are not equal. The reason of that inequality can be different barrier materials or an electric field along the direction of growth. Despite of the intuitive assumption that the average electric field in the conduction band is zero, mixing with the other bands makes the average electric field non-zero [43, 94]. The corresponding Hamiltonian for [001]-oriented structures is written as

$$\mathcal{H}_{SIA}(\mathbf{k}) = \alpha(\sigma_x k_y - \sigma_y k_x). \tag{8.10}$$

Hamiltonian 8.10 is called the Rashba Hamiltonian.

The anisotropy of chemical bonds at the interfaces can lead to an additional contribution to the effective spin-orbit interaction. Interface induced anisotropies (IIA) have a Dresselhaus-like (8.9) contribution in [001] oriented quantum wells [83, 95].

8.2.1 Spin-Orbit Interaction in the Semiconductor Channel

The spin-orbit coupling for InAs channels is usually taken in the Rashba form [41].

By analogy for silicon channels usually only the Rashba contribution is considered. Recently, however, it was shown [83] that thin silicon films inside SiGe/Si/SiGe structures may have relatively large values of spin-orbit interaction. Interestingly, the strength of the Rashba spin-orbit interaction is relatively small and is approximately ten times smaller than the value of the dominant contribution which is of the Dresselhaus type. This major contribution to the spin-orbit interaction is due to interfacial disorder induced inversion symmetry breaking and depends almost linearly on the effective electric field [95]. For a built-in field of 50kV/cm, the strength of the Dresselhaus spin-orbit interaction is found to be $\beta \approx 2\mu$eVnm, which is in agreement with the value found experimentally [123], while $\alpha_R \approx 0.1\mu$eVnm. This value of the spin-orbit interaction in confined silicon systems is sufficient for their applications as SpinFET channels.
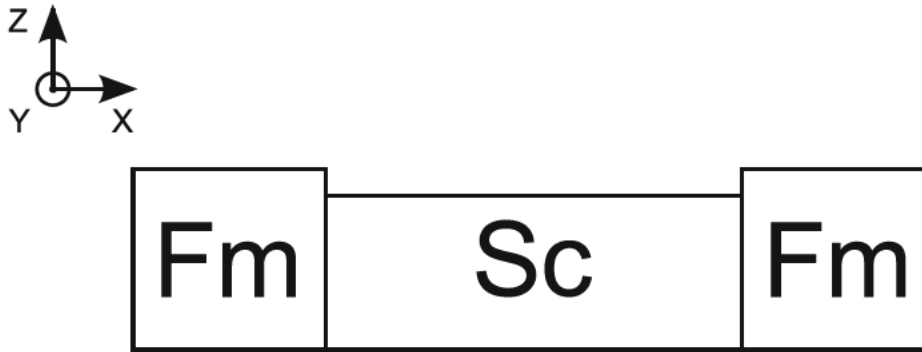
Figure 8.3: A schematic of a SpinFET, the semiconductor (Sc) channel is represented by quasi-one-dimensional channel in [100] direction, ferromagnetic contacts magnetized parallel or antiparallel to Z-axis.

8.2.2 D'yakonov-Perel' Spin Relaxation

The stronger spin-orbit interaction leads to an increased spin relaxation. The D'yakonov-Perel' mechanism is the main spin relaxation mechanism in systems with the effective spin-orbit interaction (Equation 8.9 and Equation 8.10), where the electron dispersion curves for the two spin projections are non-degenerate. In quasi-one-dimensional electron structures, however, a suppression of this spin relaxation mechanism is expected [11]. Indeed, in case of elastic scattering only back-scattering is allowed. Reversal of the electron momentum results in the inversion of the effective magnetic field direction. Therefore, the precession angle does not depend on the number of scattering events along the carrier trajectory in the channel, but is a function of the channel length alone. Thus, the spin-independent elastic scattering does not result in additional spin decoherence. In the presence of an external magnetic field, however, spin-flip processes become possible, and the Elliott-Yafet spin relaxation mechanism is likely relevant [15].

8.3 Datta-Das SpinFET Model

The originally by Datta and Das proposed spin transistor consists of one semiconductor layer and two ferromagnetic layers Figure 8.3.

To calculate the transport properties of a ballistic spin field-effect transistor a model similar to [15] and [54] is considered. The Hamiltonian in the ferromagnetic regions has the following form in the one-band effective mass approximation [47,53,54,71]

$$\mathcal{H}_F^L = \frac{p_x^2}{2m_f^*} + h_0\sigma_z, \quad x < 0, \tag{8.11}$$

$$\mathcal{H}_F^R = \frac{p_x^2}{2m_f^*} \pm h_0 \sigma_z, \quad x > t, \tag{8.12}$$

where m_f^* is the effective mass in the contacts, $h_0 = 2PE_F/(P^2 + 1)$ is the exchange splitting energy with P defined as the spin polarization in the ferromagnetic regions, E_F is the Fermi energy, and σ_z is the Pauli matrix; $\pm$ in (8.12) stands for the parallel and anti-parallel configuration of the contact magnetization. For the semiconductor channel region the Hamiltonian reads [15, 54]

$$\mathcal{H}_S = \frac{p_x^2}{2m_s^*} + \delta E_c - \frac{\alpha_R}{\hbar} \sigma_y p_x + \frac{1}{2} g \mu_B B \sigma^*, \tag{8.13}$$

where m_s^* is the subband effective mass, δE_c is the band mismatch between the ferromagnetic and the semiconductor region, α_R is the strength of the spin-orbit interaction, g is the Landé factor, μ_B is the Bohr magneton, B is the magnetic field, and $\sigma^* \equiv \sigma_x cos\gamma + \sigma_y sin\gamma$ with γ defined as the angle between the magnetic field and the transport direction.

To calculate the dependence of the transport properties on the spin-orbit interaction the electron eigenfunctions in the various regions are needed. For the ferromagnetic regions spin-up and spin-down eigenstates have the form $(1, 0)^\dagger$ and $(0, 1)^\dagger$, respectively. The wave function in the left contact has the following form [15, 54]

$$\Psi_{L\uparrow}(x) = (e^{ik_\uparrow x} + R_\uparrow e^{-ik_\uparrow x}) \begin{pmatrix} 1 \\ 0 \end{pmatrix} + R_\downarrow e^{-ik_\downarrow x} \begin{pmatrix} 0 \\ 1 \end{pmatrix}, \tag{8.14}$$

$$\Psi_{L\downarrow}(x) = R_\uparrow e^{-ik_\uparrow x} \begin{pmatrix} 1 \\ 0 \end{pmatrix} + (e^{ik_\downarrow x} + R_\downarrow e^{-ik_\downarrow x}) \begin{pmatrix} 0 \\ 1 \end{pmatrix}, \tag{8.15}$$

where (8.14) represents the incoming spin-up electrons and (8.15) the incoming spin-down electrons, correspondingly, $k_{\uparrow(\downarrow)} = \sqrt{2m_f^*(E \mp h_0)/\hbar^2}$ is the wave vector of the spin-up(spin-down) electron and $R_{\uparrow(\downarrow)}$ is the amplitude of the reflected wave. To find eigenvectors to the corresponding vector $k_{\uparrow(\downarrow)}$ the Schrödinger equation spin-up spinor for the right contact the wave function is given by [15, 54]

$$\Psi_R(x) = C_\uparrow e^{ik_\uparrow x} \begin{pmatrix} 1 \\ 0 \end{pmatrix} + C_\downarrow e^{ik_\downarrow x} \begin{pmatrix} 0 \\ 1 \end{pmatrix}. \tag{8.16}$$

For the semiconductor region the wave function can be written as [15, 54]

$$\Psi_S(x) = A_+ e^{ik_{x1}^{(+)}x} \begin{pmatrix} k_1 \\ 1 \end{pmatrix} + B_+ e^{ik_{x2}^{(+)}x} \begin{pmatrix} k_2 \\ 1 \end{pmatrix} +$$
$$+ A_- e^{ik_{x1}^{(-)}x} \begin{pmatrix} k_3 \\ -1 \end{pmatrix} + B_- e^{ik_{x2}^{(-)}x} \begin{pmatrix} k_4 \\ -1 \end{pmatrix}, \tag{8.17}$$

where $k_{x1(x2)}^{(+)}$ and $k_{x1(x2)}^{(-)}$ are the wave vectors obtained by solving the equations $\dfrac{\hbar^2 k^2}{2m_s^*} +$

$$\delta E_c \pm \sqrt{\left(\frac{Bg\mu_B \cos(\gamma)}{2}\right)^2 + \left(\frac{Bg\mu_B \sin(\gamma)}{2} - \alpha_R k\right)^2} = E,\text{ respectively.}$$

The usual boundary conditions are applied: the wave functions are continuous at the interfaces and that there is a step discontinuity of the first derivative of the wave function over channel direction $\left(\dfrac{\partial \Psi}{\partial x}\right)$ due to an assumed delta-function-like barrier at the interfaces between the ferromagnetic and the semiconductor region. Thus, boundary conditions are written as [47]

$$\Psi_L(x)\Big|_{0^-} = \Psi_S(x)\Big|_{0^+}, \tag{8.18}$$

$$\Psi_S(x)\Big|_{t^-} = \Psi_R(x)\Big|_{t^+}, \tag{8.19}$$

$$-\frac{i\hbar}{m_f^*}\frac{\partial \Psi_L(x)}{\partial x}\Bigg|_{0^-} - \frac{2i}{\hbar}U_x\Psi_L(x)\Bigg|_{0^-} = -\frac{i\hbar}{m_s^*}\frac{\partial \Psi_S(x)}{\partial x}\Bigg|_{0^+}, \tag{8.20}$$

$$-\frac{i\hbar}{m_s^*}\frac{\partial \Psi_S(x)}{\partial x}\Bigg|_{t^-} = -\frac{i\hbar}{m_f^*}\frac{\partial \Psi_R(x)}{\partial x}\Bigg|_{t^+}. \tag{8.21}$$

The coefficients k_1, k_2, k_3, k_4 are calculated as [15, 54]

$$k_1 = -\frac{i\left(Bg\mu_B \sin(\gamma) - 2\alpha_R k_{x1}^{(+)}\right) - Bg\mu_B \cos(\gamma)}{2\sqrt{\left(\frac{Bg\mu_B \cos(\gamma)}{2}\right)^2 + \left(\frac{Bg\mu_B \sin(\gamma)}{2} - \alpha_R k_{x1}^{(+)}\right)^2}}, \tag{8.22}$$

$$k_2 = -\frac{i\left(Bg\mu_B \sin(\gamma) - 2\alpha_R k_{x2}^{(+)}\right) - Bg\mu_B \cos(\gamma)}{2\sqrt{\left(\frac{Bg\mu_B \cos(\gamma)}{2}\right)^2 + \left(\frac{Bg\mu_B \sin(\gamma)}{2} - \alpha_R k_{x2}^{(+)}\right)^2}}, \tag{8.23}$$

$$k_3 = \frac{i\left(Bg\mu_B \sin(\gamma) - 2\alpha_R k_{x1}^{(-)}\right) - Bg\mu_B \cos(\gamma)}{2\sqrt{\left(\frac{Bg\mu_B \cos(\gamma)}{2}\right)^2 + \left(\frac{Bg\mu_B \sin(\gamma)}{2} - \alpha_R k_{x1}^{(-)}\right)^2}}, \tag{8.24}$$

$$k_4 = \frac{i\left(Bg\mu_B \sin(\gamma) - 2\alpha_R k_{x2}^{(-)}\right) - Bg\mu_B \cos(\gamma)}{2\sqrt{\left(\frac{Bg\mu_B \cos(\gamma)}{2}\right)^2 + \left(\frac{Bg\mu_B \sin(\gamma)}{2} - \alpha_R k_{x2}^{(-)}\right)^2}}. \tag{8.25}$$

The reflection and transmission coefficients are determined by applying the boundary conditions at the ferromagnet/semiconductor interfaces.

The current through the device is computed as [68, 88, 89]

$$I^{P(AP)}(V) = \frac{e}{h} \int_{\delta E}^{\infty} \left[T_\uparrow^{P(AP)}(E) + T_\downarrow^{P(AP)}(E)\right]$$
$$\left\{\frac{1}{1 + e^{\frac{E - E_F}{k_B T}}} - \frac{1}{1 + e^{\frac{E - E_F + eV}{k_B T}}}\right\} dE, \tag{8.26}$$

where k_B is the Boltzmann constant, T is the temperature, and V is the voltage. The spin-up ($T_\uparrow^P$) and spin-down ($T_\downarrow^P$) transmission probabilities for the parallel configuration of the contact magnetization are defined as

$$T_\uparrow^P = |C_\uparrow|^2 + \frac{k_\downarrow}{k_\uparrow}|C_\downarrow|^2, \tag{8.27}$$

$$T_\downarrow^P = \frac{k_\uparrow}{k_\downarrow}|C_\uparrow|^2 + |C_\downarrow|^2. \tag{8.28}$$

For the anti-parallel configuration of the contact magnetization the transmission probabilities are given by

$$T_\uparrow^{AP} = \frac{k_\downarrow}{k_\uparrow}|C_\uparrow|^2 + |C_\downarrow|^2, \tag{8.29}$$

$$T_\downarrow^{AP} = |C_\uparrow|^2 + \frac{k_\uparrow}{k_\downarrow}|C_\downarrow|^2. \tag{8.30}$$

The conductance is defined as

$$G^{P(AP)} = \lim_{V \to 0} \frac{I^{P(AP)}}{V}. \tag{8.31}$$

In the limit of low temperature the conductance must coincide with the one obtained from the Landauer-Büttiker formula [13, 68]

$$G^{P(AP)} = \frac{e^2}{h}\left(T_\uparrow^{P(AP)}(E_F) + T_\downarrow^{P(AP)}(E_F)\right). \tag{8.32}$$

Finally, the tunneling magnetoresistance (TMR) is defined as [15, 54]

$$\text{TMR} \equiv \frac{G^P - G^{AP}}{G^{AP}}. \tag{8.33}$$
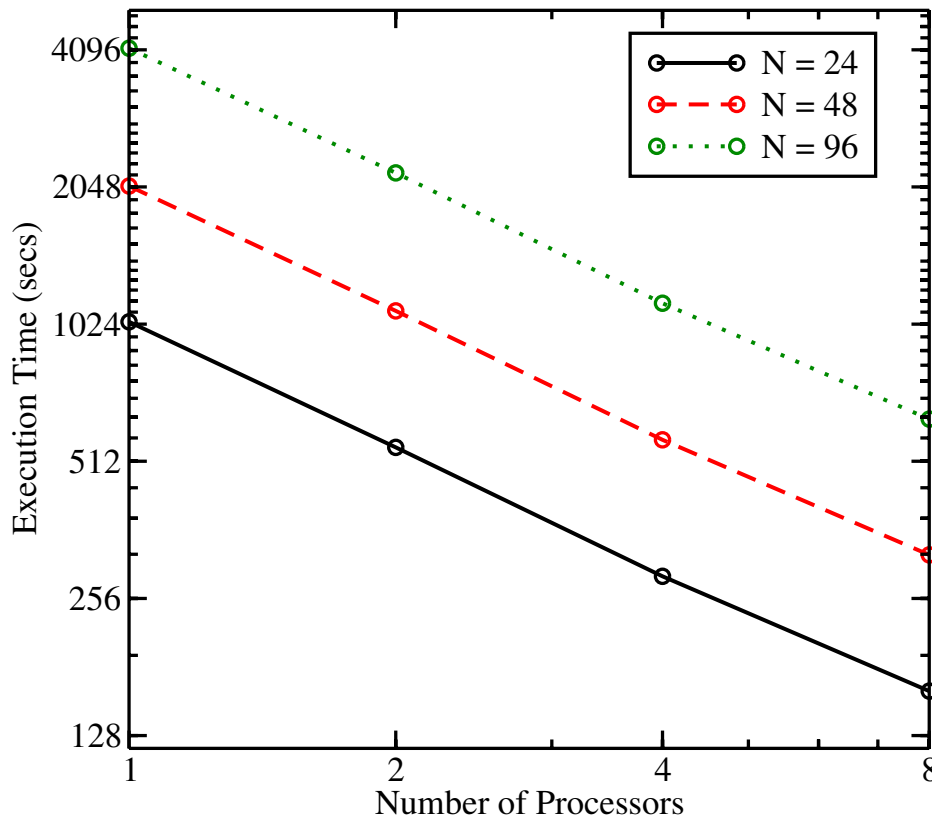
Figure 8.4: Dependence of time of calculations on number of processor cores.

8.4 Code Parallelization

The dependence of the conductance through the silicon SpinFET on the physical parameters was investigated. In order to calculate the conductance one first has to determine the wave vectors, then compose the system of equations corresponding to the boundary conditions, and finally solve the obtained system of linear equations to gain the transmission coefficients for the spin-up and spin-down electrons. These calculations must be performed for the parallel and the anti-parallel configuration of the contact magnetization for each energy point of the half-infinite integrand (8.26). It follows from (8.32) that the integral evaluated numerically describes the conductance for a single point of the conduction band mismatch δE_c, at a single value of temperature T. Thus to investigate the transport properties of the silicon SpinFET at various parameter values a huge amount of calculations must be carried out. To reduce the simulation time the code for the model must be heavily optimized and parallelized.

The usual techniques for parallelization are divided into two groups - parallelization in case of shared-memory and parallelization in case of distributed memory systems. The advantage of shared-memory parallelization is that it guarantees uniform access to the memory for each process. This means that the time spent for data manipulation in the memory is approximately the same for each process. The advantage of distributed
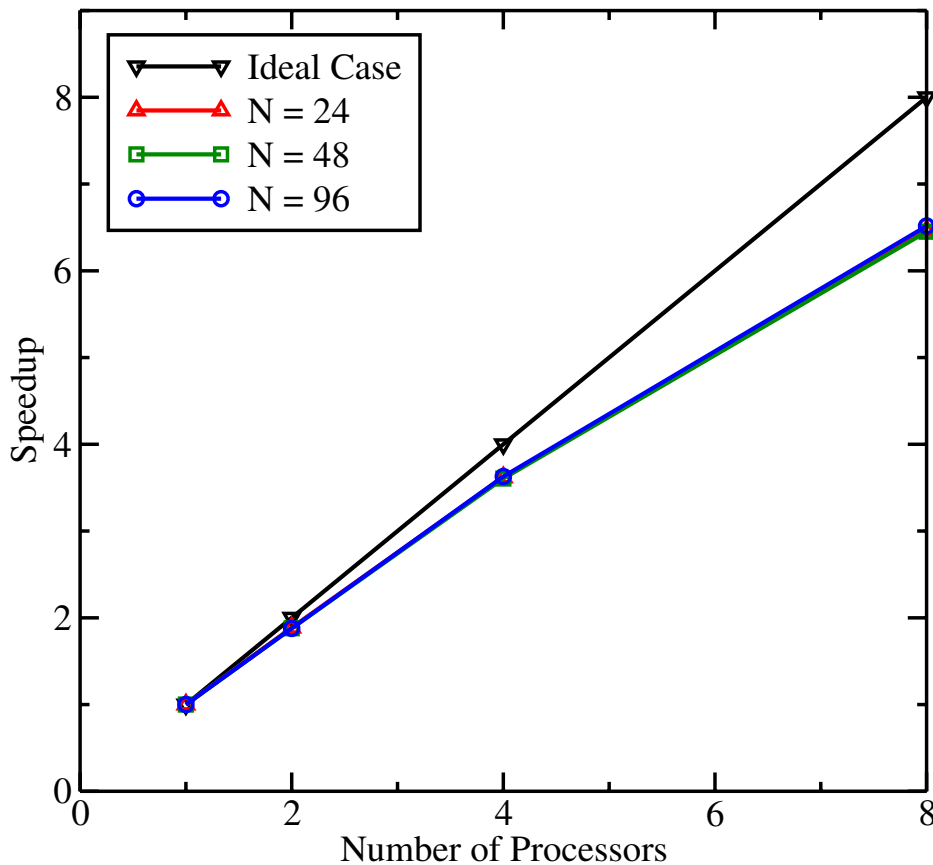
Figure 8.5: Speedup of the calculations as a function of number of processor cores.

calculations is that the number of processors used for the calculations is not limited to the number of processors on a single node.

In the simulations the code is parallelized with the OpenMP library. Because of the absence of the correlation between the conductances at different energy points the whole calculations are distributed between a large number of computing threads. Thus the time spent for the calculations is reduced proportionally to the number of parallel threads. Although threads perform calculations in parallel, the time spent by each thread to fulfill the tasks is not the same. Therefore one has to take proper care of a uniform distribution of the computational load between the threads. This problem is crucial for obtaining the maximum possible speed-up. Since OpenMP provides a possibility to control the amount of calculations for each thread in the run-time mode, the problem of the uniform distribution of the computational load is solved by standard tools.

The performance of the code has been improved by utilizing the OpenMP approach. The results of using the parallel implementation are presented in Table 8.1. The actual speedup of the code is very close to the ideal (linear) speedup, in which the increase of the number of processors (cores) by two leads to the decrease in the computing time

Table 8.1: Calculation time (seconds) depending on the number of processors and the number of points.

Number of Processors	N=24	N=48	N=96
1	1036	2057	4129
2	549	1094	2198
4	286	570	1138
8	160	318	633

by two. This excellent improvement is possible due to the already mentioned fact that there is no correlation between the calculations of the conductances.

Calculations in the presence of temperature require high accuracy. Therefore, the adaptive methods from the GNU Scientific Library [2] have been used for the numerical integration.

8.5 Simulation Results

Two types of material for the semiconductor region are used: InAs, which is characterized by a strong value of the spin-orbit interaction, and silicon, which is characterized by a moderate value of the spin-orbit interaction.

8.5.1 InAs Channels

All calculations for the InAs semiconductor channel assume that the dominant mechanism of the spin-orbit coupling due to the geometry-induced inversion symmetry breaking (Rashba type). Common simulation parameters are as follows: the effective mass for the ferromagnetic region $m_f^* = m_0$ and for the semiconductor region m_s^*=0.036m_0, where m_0 is the electron rest mass. Figure 8.6 shows the dependence of the TMR on the value of the band mismatch δE_c between the ferromagnetic source contact and the semiconductor channel. The TMR oscillates between positive and negative values. As the length of the semiconductor channel decreases, the period of the oscillations increases roughly proportionally to the inverse length of the semiconductor channel.

The temperature exerts a significant influence on the device characteristics as shown in Figure 8.7. For a channel length t=0.05μm the oscillatory amplitude of the TMR decreases for T=77K and completely vanishes for T=180K. The reason for the oscillatory behavior to disappear at T=180K is a relatively short period of the conductance oscillations (and correspondingly TMR oscillation shown in Figure 8.6) with respect
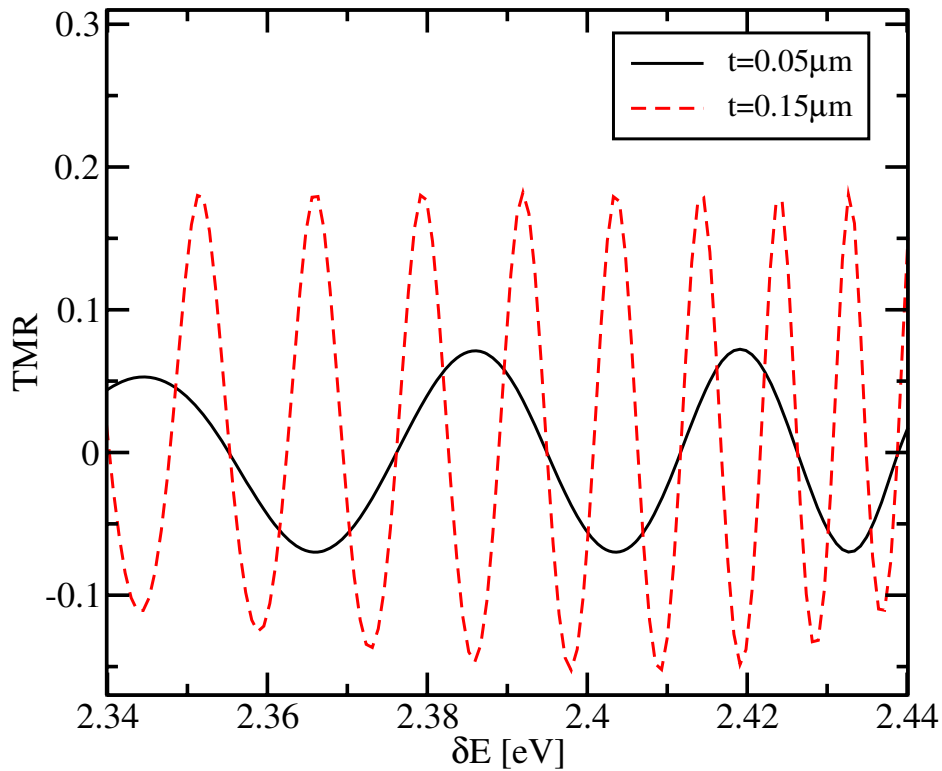
Figure 8.6: TMR dependence on the value of δE_c, for E_F=2.47eV, P=0.4, B=0T, z=0, α_R=42.3meVnm, T=0K.
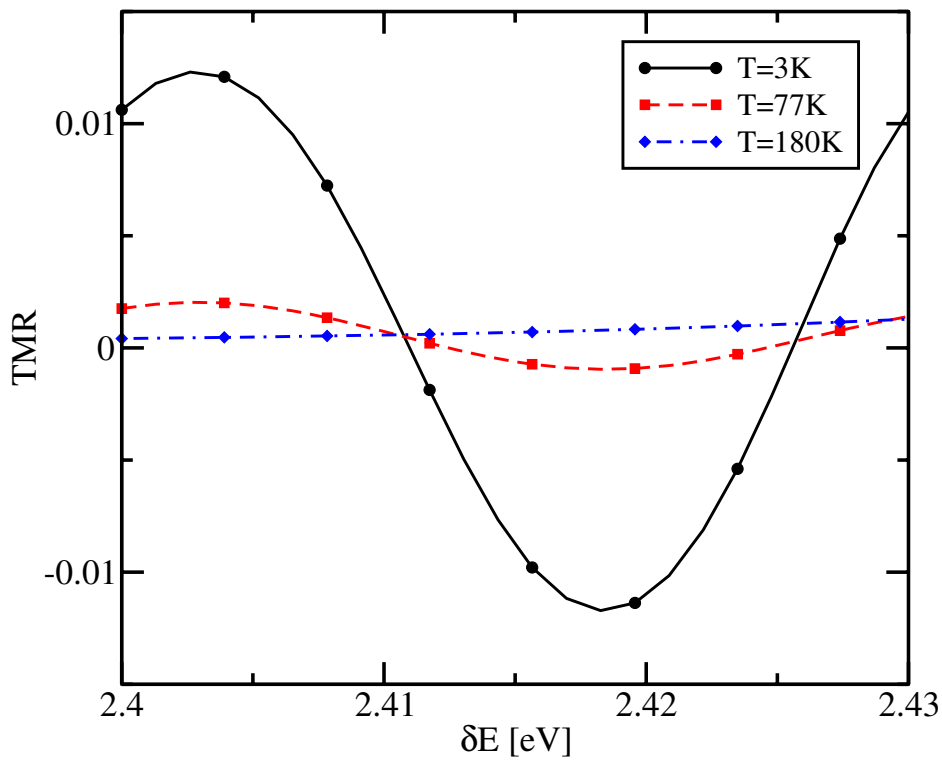
Figure 8.7: TMR dependence on the value of δE_c, for α_R=31.7meVnm, E_F=2.47eV, P=0.4, B=0T, z=0, t=0.05μm.

89
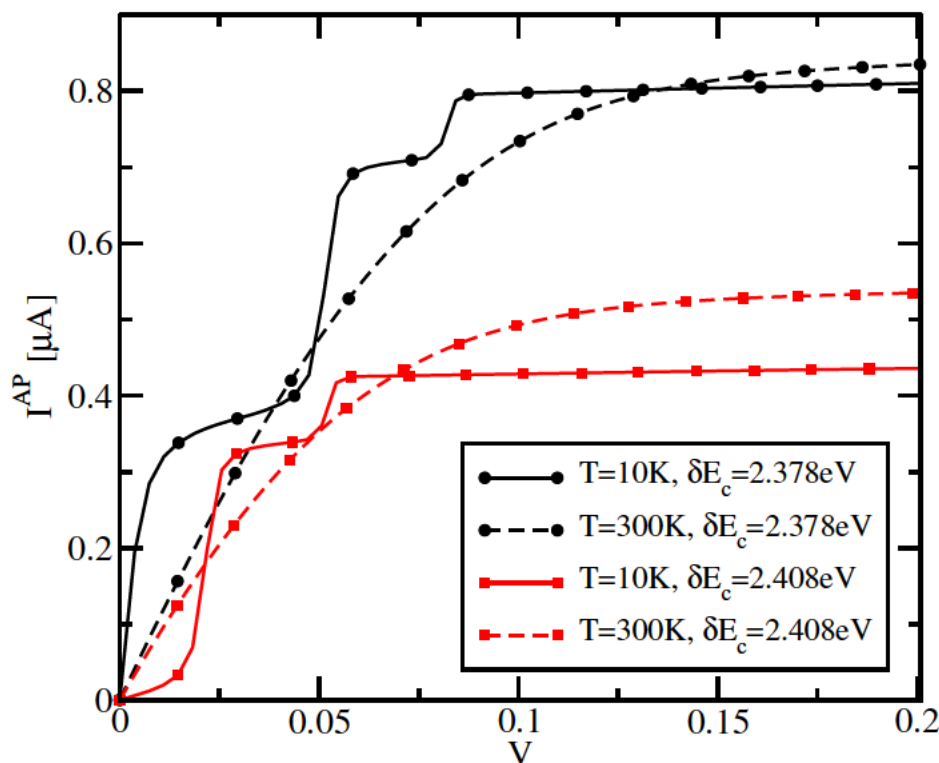
Figure 8.8: Current dependence on the value of the drain-source voltage for $B=0$T, $z=3$, $t=0.03\mu$m, $P=0.4$.

to δE_c. Thus, one can expect that for the shorter channel the amplitude of oscillations is sufficient to modulate the current in the SpinFET at higher temperatures.

To facilitate the injection of the spin-polarized current into the channel, following [15] and [54], delta-function barriers of strength $z = 2m_f^* U/h^2 k_F$, where $k_F = \sqrt{2m_f^* E_F/\hbar^2}$, at the interfaces between the contacts and the channel are introduced. The current dependence on the value of the drain-source voltage is shown in Figure 8.8. A clear S-like shape of the curves is observed at $T=10$K. This is a manifestation of the conductance oscillations as a function of δE_c, which have a large amplitude due to the presence of the delta-function barriers at the interfaces between the contact and the channel ($z=3$). A large amplitude of the conductance oscillations guarantees the different slopes of the I-V curves corresponding to different δE_c. Although the S-like non-linearity is not well pronounced at higher temperatures, the difference in the slopes at small voltages is not completely washed out, even at room temperature.

Figure 8.9 and Figure 8.10 show the dependence of the TMR on the band mismatch between the source/drain contacts and the semiconductor region, for several temperatures in absence of a magnetic field and under an applied field of 3T. At low temperatures the TMR oscillates around zero, and the strength of the magnetic field does not influence the oscillations much, which is in agreement with [54]. As the band
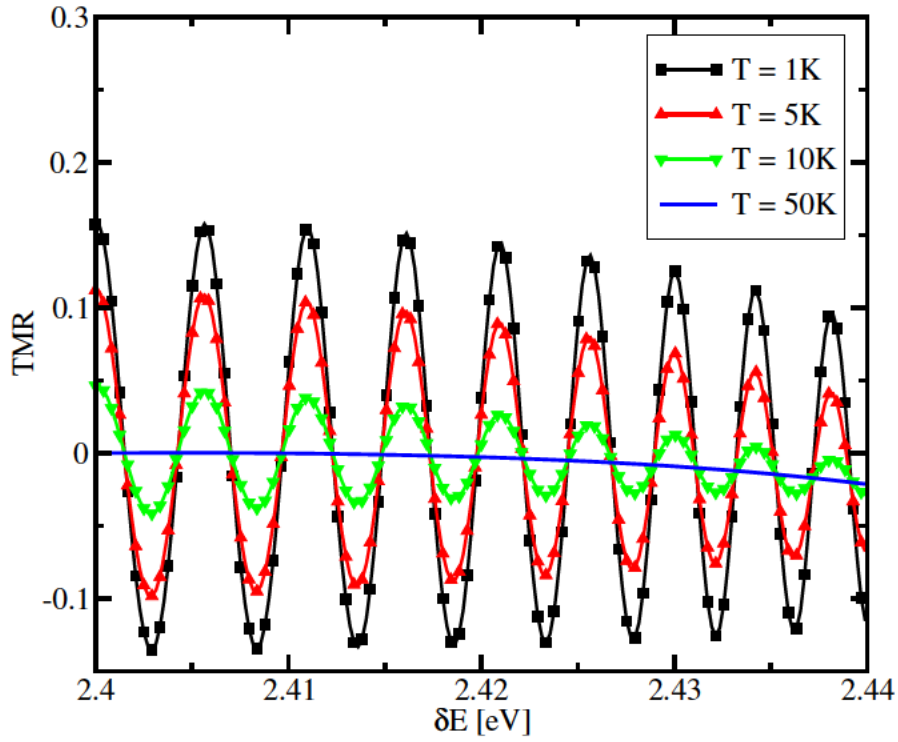
Figure 8.9: TMR dependence on the value of δE_c, for E_F=2.47eV, eV=0.001eV, α_R=31.7meVnm without magnetic field.
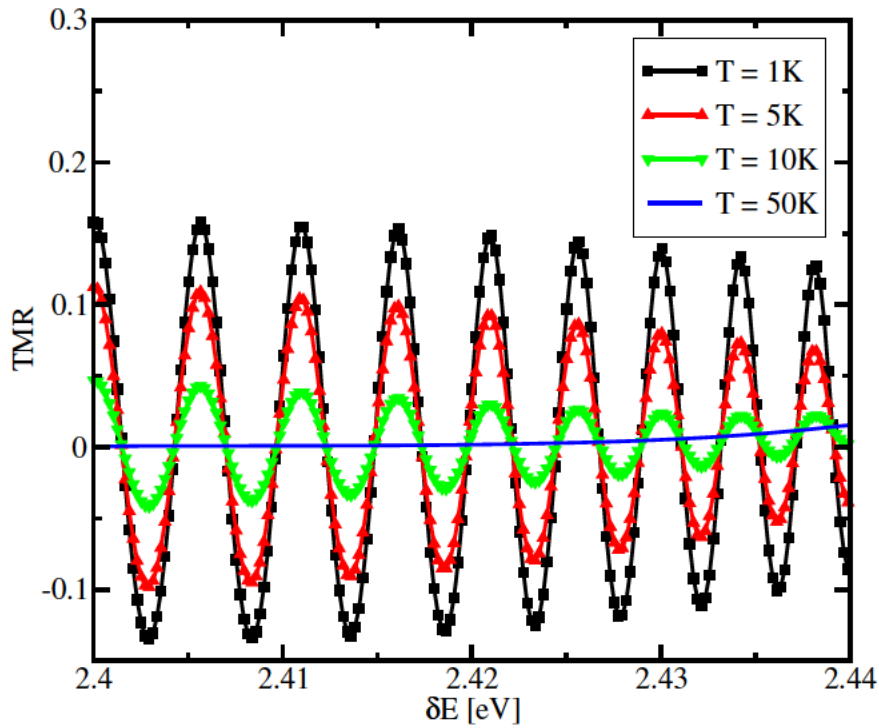
Figure 8.10: Same as in Figure 8.9 with a magnetic field of 3T.
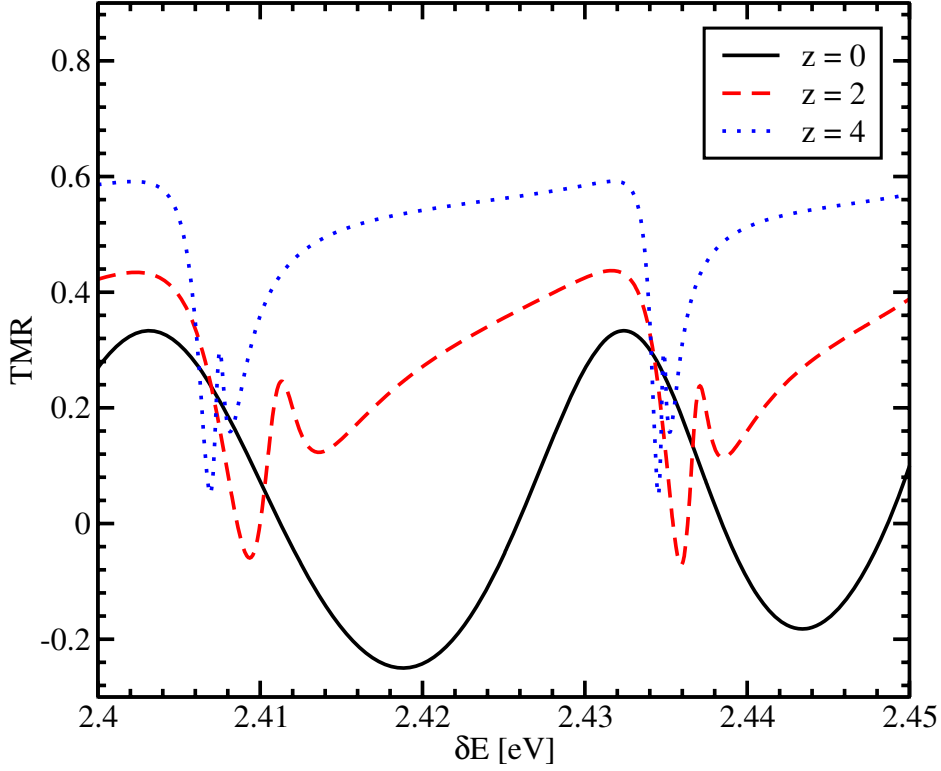
Figure 8.11: TMR dependence on the value of the δE_c for different values of barrier z, for the Fermi energy at E_F=2.47eV, length t=0.05μm, and polarization P=0.5.

mismatch increases, influence of the magnetic field becomes more significant. Also, one can see that increasing the temperature leads to a dramatic decrease in the amplitude of the TMR oscillations and reduces the ability to modulate the TMR by adjusting the band mismatch.

Another option to proceed to higher temperatures is to boost the value of the TMR by exploiting its dependence on α_R. Figure 8.11 illustrates the corresponding change. As the barriers become stronger the quantization of the energy in the semiconductor channel becomes more pronounced. The energy quantization is responsible for the appearance of the sharp peaks on the TMR dependence on δE_c clearly seen in Figure 8.11. An excellent feature following from Figure 8.11 is that the TMR value remains positive in a broad range of δE_c. Most importantly, the sign and the values of the TMR depend on the strength of the spin-orbit interaction. It then follows that in the presence of the barriers between the contact and the channel the values of the TMR must depend on the strength of the spin-orbit interaction controlled by the gate voltage at elevated temperatures as well. Next this consideration [15,54] is generalized to finite temperatures.

Figure 8.12 displays the TMR dependence on the strength of the spin-orbit interaction at different temperatures. The TMR modulation is preserved at elevated temperatures, thus opening a practical possibility to control the TMR by changing the value
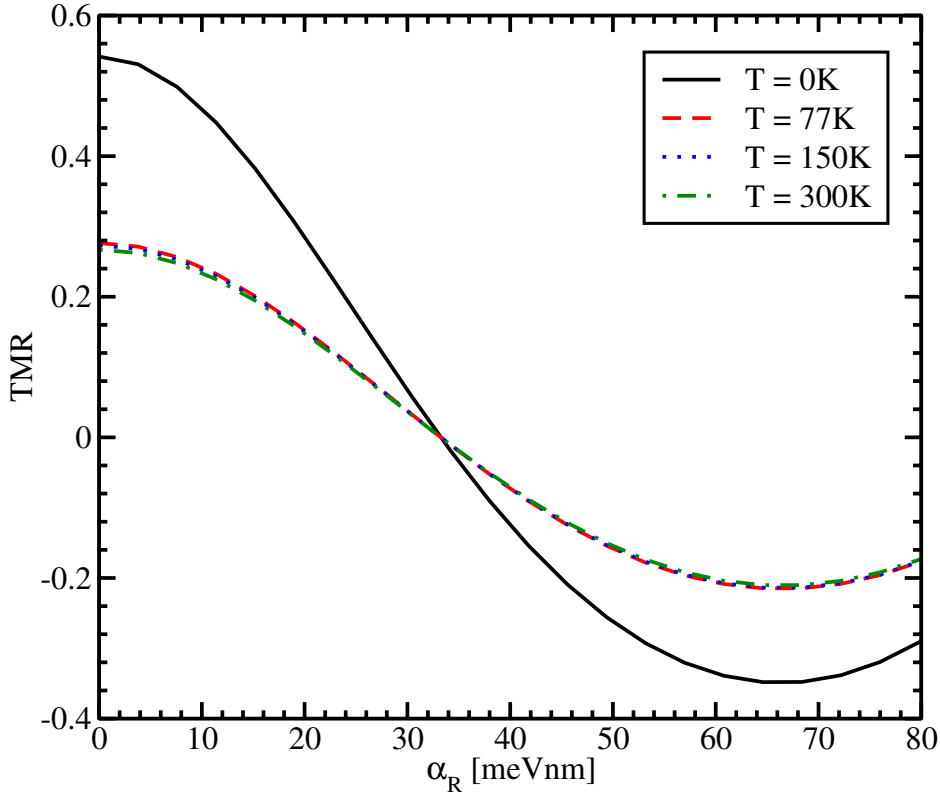
Figure 8.12: TMR dependence on the value of spin-orbit interaction for E_F=2.47eV, t=0.05μm, δE_c=2.42eV, P=0.5, z=4.

of α_R even at room temperature.

8.5.2 Silicon Channels

Square silicon fins with [100] or [110] orientation, with (001) horizontal faces are considered. The parabolic band approximation for the band structure in silicon is not sufficient to accurately obtain the subband structure in thin and narrow silicon fins. The two-band **k·p** model proposed in [9] is employed, which has been shown to be accurate up to 0.5eV above the conduction band edge in silicon [112]. The resulting Schrödinger differential equation, with the confinement potential appropriately added to the Hamiltonian [9], is discretized using the box integration method and solved for each value of the conserved momentum p_x along the current direction using efficient numerical algorithms available through the Vienna Schrödinger-Poisson framework (VSP) [62].

Figure 8.13 demonstrates the dependence of the subband minima as function of the fin thickness t for the lowest four subbands; the fin orientation is along the [110] direction. The dependence of the splitting between the unprimed subbands with decreasing t, which are perfectly degenerate in the effective mass approximation, is clearly seen.
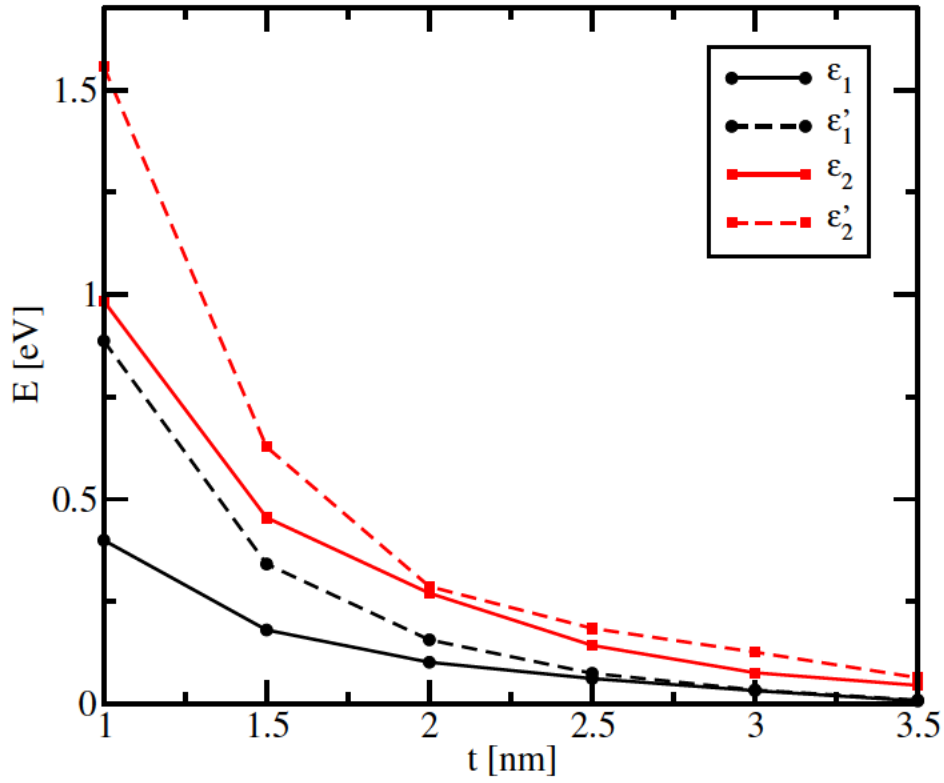
Figure 8.13: Subband minima as a function of thickness t in a [110]-oriented fin.
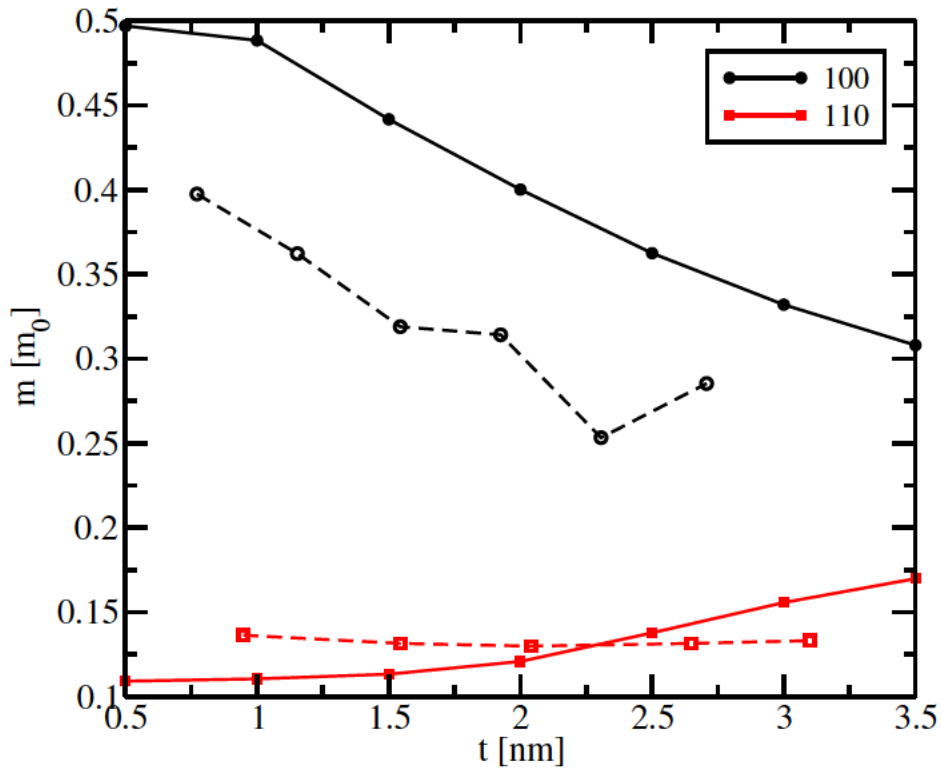
Figure 8.14: Ground subband effective mass dependence on t in [100] and [110] fins. Dashed lines are from [114].
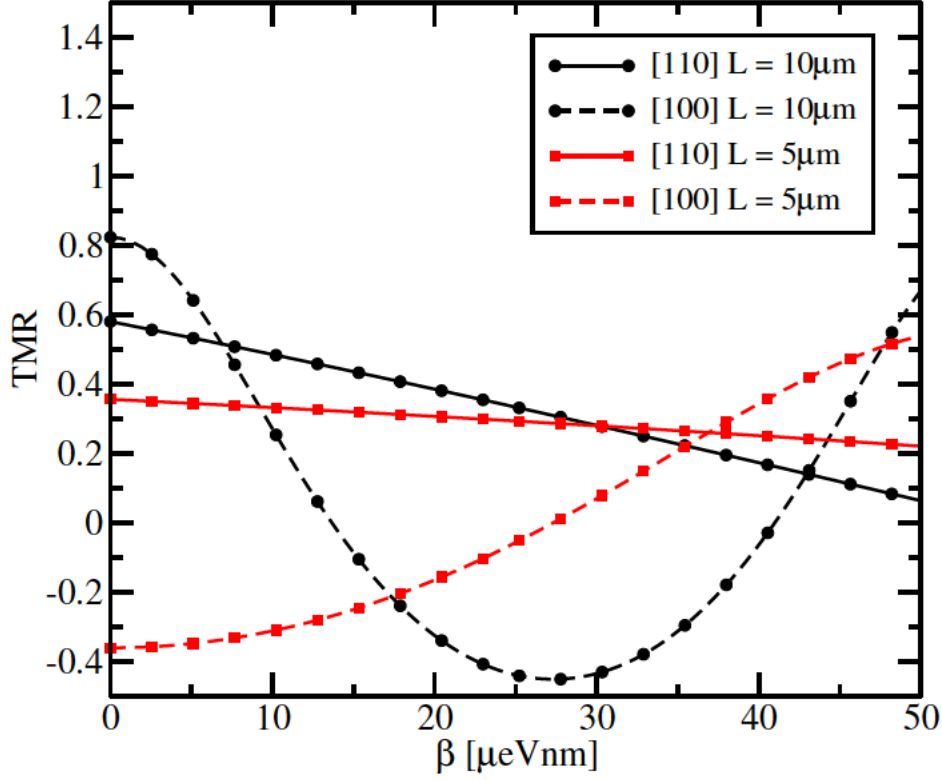
Figure 8.15: TMR dependence on the value of the Dresselhaus spin-orbit interaction for t=1.5nm, B=4T, P=0.6, z=3, γ=0, T=0K.

The splitting between valleys in a [100] fin is negligible [114]. In contrast to that, the dependence of the effective mass of the ground subband in [100] fins on t is more pronounced as compared to [110] fins. Results of density-functional calculations [114] confirm the mass dependences obtained from the **k·p** model (Figure 8.14).

With the values of the effective masses and subband offsets obtained, the conductance properties for the parallel and anti-parallel configurations of the contact magnetization is studied. The spin-orbit interaction is treated in the Dresselhaus form (8.9). The Hamiltonian in the channel for [100] oriented fins reads

$$\mathcal{H}_S = \sum_n \frac{p_x^2}{2m_n^*} + \delta E_n - \frac{\beta}{\hbar}\sigma_x p_x + \frac{1}{2}g\mu_B B\sigma^*, \tag{8.34}$$

and

$$\mathcal{H}_S = \sum_n \frac{p_x^2}{2m_n^*} + \delta E_n - \frac{\beta}{\hbar}\sigma_y p_x + \frac{1}{2}g\mu_B B\sigma^*, \tag{8.35}$$

for [110] oriented fins. Here m_n^* is the subband effective mass, δE_n is the subband mismatch between the ferromagnetic region and the channel, and β is the strength of the spin-orbit interaction.
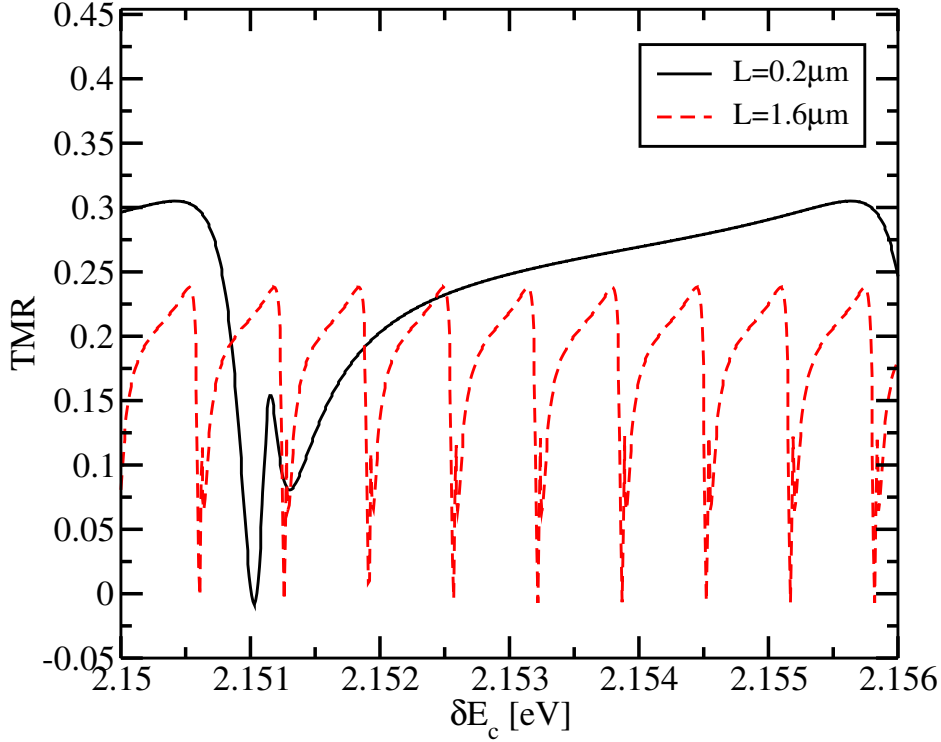
Figure 8.16: TMR dependence on the value of the δE_c for E_F=2.47eV, P=0.4, z=3, β=42.3μeVnm, T=0K.

Figure 8.15 shows the dependence of the TMR for [100] and [110] oriented fins with $t = 1.5$nm on the value of the spin-orbit interaction. Fins with [100] orientation show a stronger dependence on β compared to [110] oriented fins. Thus [100] oriented fins are preferred for silicon SpinFETs. The reason of the stronger dependence is that the characteristic length on which the spin-orbit interaction produces the full spin precession is defined by the inverse of the wave vector $k_D = m_n^* \beta / \hbar^2$. As shown in Figure 8.14, the effective mass value for the [110] oriented fins is smaller compared to the [100] oriented fins, hence for the same variation of k_D in case of the [110] oriented fins a larger variation of β is required to achieve the same TMR value modulation.

Figure 8.16 shows the dependence of the oscillations of the TMR on the value of the conduction band mismatch δE_c. The period of the oscillations is roughly inversely proportional to the length of the semiconductor channel as also shown in Figure 8.6. The presence of the delta-function barriers at the interfaces between the contact and the channel exerts a significant influence on the oscillation shape. For higher and thicker barriers, the TMR, although being a periodic function of the conductance band mismatch, stops oscillating around zero and becomes positive (or negative) in a broad range of the conduction band mismatch. This sign definitiveness leads to the complete absence of the oscillations of the TMR at T=77K as shown in Figure 8.17. It is important that, although reduced, the TMR is not zero at 77K. Therefore, the TMR modulation as a function of the spin-orbit interaction strength is preserved even
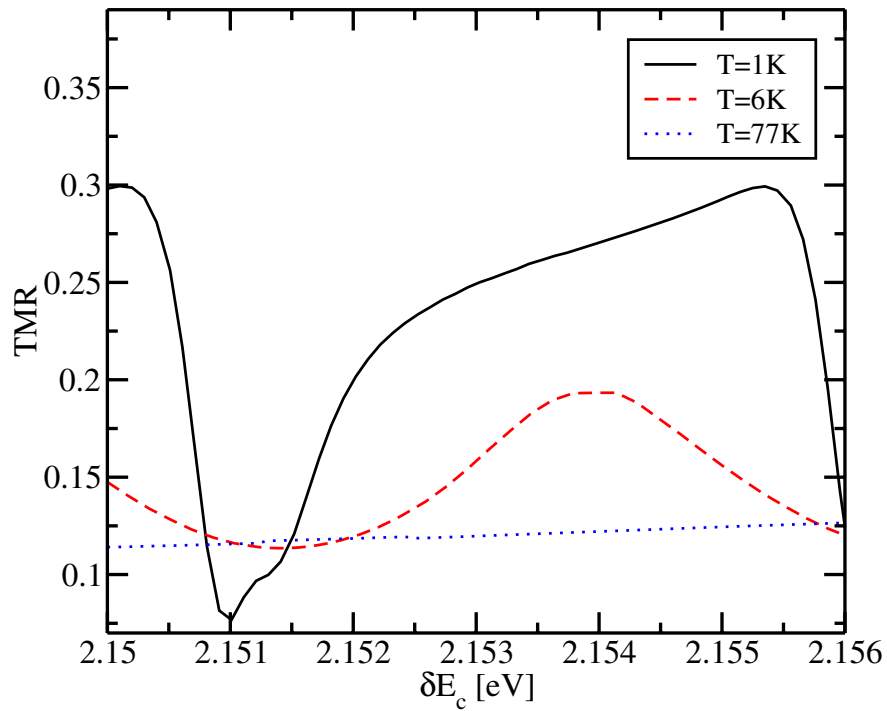
Figure 8.17: TMR dependence on the value of the δE_c for E_F=2.47eV, P=0.4, z=3, t=0,2μm, V=0.1meV, β=42.3μeVnm.
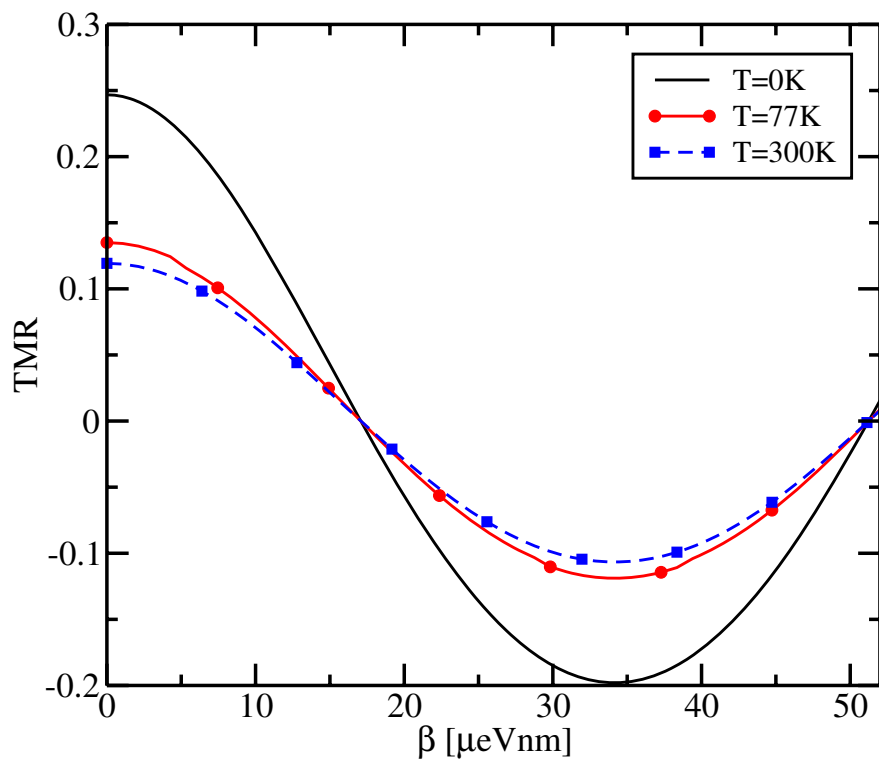
Figure 8.18: TMR dependence on the value of the Dresselhaus spin-orbit interaction for E_F=2.47eV, δE_c=2.154eV, P=0.4, z=3, t=8μm, V=1meV.

at high temperatures as shown in Figure 8.18. This opens the possibility to modulate the TMR by changing the value of β even at room temperature.

9 Summary and Outlook

The **k·p** approach is a powerful tool which allows to obtain the wave functions and the eigenenergies of stationary states in confined electron systems. A two-band **k·p** model including spin is employed to find the electron subband energies and the corresponding wave functions in thin silicon films under shear strain. To describe spin properties in silicon films an important ingredient, the intrinsic spin-orbit interaction is taken into account. The **k·p** model is extensively verified by comparing the results to a computationally more demanding but more accurate method which allows to represent the wave function by an appropriate linear combination of bulk band Bloch functions. The Bloch functions are obtained from a non-local pseudo-potential solver.

The use of the two-band **k·p** model with spin-orbit interaction included allows to investigate the subband structure including spin. In (001) oriented silicon films the degeneracy of the unprimed subbands is lifted by shear strain. The value of the splitting depends on the in-plane wave vector value, the film thickness, the external electric field, and strain. This leads to the transport effective mass dependence on strain. By taking into account this dependence the mobility in thin films is expected to be enhanced by 30-40% along the [110] direction of tensile strain. The usually ignored dependence of the surface roughness and electron-phonon scattering matrix elements on shear strain results in additional 70% mobility enhancement resulting in an overall two-fold mobility enhancement in thin silicon films.

The unprimed subbands degeneracy lifting is even more important for spin transport properties in silicon. Indeed, it is shown that when the spin-orbit interaction is taken into account the minimum value of the energy splitting between the spin-up and spin-down states from the two otherwise degenerate unprimed subbands is determined by the strength of the spin-orbit interaction alone. This leads to a strong mixing between the spin-up and spin-down states from the two unprimed subbands resulting in the formation of the hot spots characterized by strong spin relaxation. With shear strain the degeneracy is lifted, which results in an almost two orders of magnitude increase of the spin lifetime in thin silicon films. The calculations are performed by considering surface roughness and electron-phonon interaction mediated spin relaxation. Both transversal and longitudinal acoustic phonons are included. Because of the necessity to perform double integration with respect to the in-plane momentum on which the wave functions depend upon, the use of analytically found wave functions was a critical to reduce the computation time. It was found that, in contrast to the momentum relaxation time determined by the intravalley scattering, intervalley processes between equivalent valleys (g-processes) are the most important for spin relaxation.

The same but properly rotated two-band $\mathbf{k \cdot p}$ Hamiltonian with spin also allows to find the dispersions and the wave functions of the primed subbands. Evaluation of the spin relaxation due to optical phonons mediated scattering between non-equivalent valleys (f-processes) demonstrates that in thin films f-scattering can be neglected, in contrast to bulk silicon where it is mostly responsible for spin lifetime. The inclusion of the zero-strain valley splitting is done by considering the valley coupling through the Γ-point. This softens the spin relaxation hot spots, although the strong spin lifetime enhancement with strain is preserved.

The long spin lifetime in strained silicon films make these structures attractive for use as spin conducting channels in spin field-effect transistors. It is shown that in short silicon channels the conduction band mismatch between the channel and the ferromagnetic contacts allows to modulate tunneling magnetoresistance but only at low temperature. At room temperature the magnetoresistance oscillations are preserved only if the Schottky barriers between the channel and the contacts are present. It is shown that due to the larger transport mass and therefore stronger spin-orbit interaction the length of the channel needed to observe the maximum magnetoresistance modulation is shorter for [001] oriented silicon fins making them preferred candidates for practical implementations. However, even in this case the length of the channel is close to a micron, and finding efficient ways to manipulate spins in silicon by purely electrical means become paramount.

The spin properties and spin transport in silicon films are promising for designing low power devices in the near future. The methods developed in the thesis can be generalized to study the spin transport in three-dimensional structures and FinFETs. Because the numerical solution of the Schrödinger equation is required, developing fast Schrödinger equation solver, interpolation schemes, and extensive use of accelerators (Intel® Xeon Phi™or GPU) is necessary in the future for an ultimate evaluation of spin properties in confined silicon systems.

Bibliography

[1] International Technology Roadmap for Semiconductors 2010 Update Overview. http://www.itrs.net/Links/2010ITRS/2010Update/-ToPost/2010_Update_Overview.pdf, 2010.

[2] GNU Scientific Library [ONLINE]. http://www.gnu.org/s/gsl/, 2013.

[3] The Discovery of Giant Magnetoresistance (Scientific Background on the Nobel Prize in Physics 2007) [ONLINE]. http://www.kva.se/Documents/Priser/Nobel/2007/sciback_fy_en_07.pdf, 2013.

[4] S. F. Alvarado and P. Renaud. Observation of Spin-Polarized Eelectron Tunneling from a Ferromagnet into GaAs. *Physical Review Letters*, 68:1387–1390, 1992.

[5] T. Ando, A. B. Fowler, and F. Stern. Electronic Properties of Two-Dimensional Systems. *Reviews of Modern Physics*, 54:437–672, 1982.

[6] A. G. Aronov and G. E. Pikus. Spin Injection in Semiconductors. *Fizika i Tekhnika Poluprovodnikov (Sankt-Peterburg)*, 10(6):1177–80, 1976.

[7] O. Baumgartner, Z. Stanojevic, K. Schnass, M. Karner, and H. Kosina. VSP–a Quantum-Electronic Simulation Framework. *Journal of Computational Electronics*, 12(4):701–721, 2013.

[8] G. Bir, A. G. Aronov, and G. E. Pikus. Spin Relaxation of Electrons due to Scattering by Holes. *Journal of Experimental and Theoretical Physics*, 42(4):1382–1397, 1975.

[9] G. Bir and G. Pikus. *Symmetry and Strain-Induced Effects in Semiconductors.* New York/Toronto: J. Wiley & Sons, 1974.

[10] V. Borisenko and S. Ossicini. *What is What in the Nanoworld: A Handbook on Nanoscience and Nanotechnology.* Wiley, 2013.

[11] A. Bournel, P. Dollfus, P. Bruno, and P. Hesto. Gate-Induced Spin Precession in an $In_{0.53}Ga_{0.47}As$ Two Dimensional Electron Gas. *The European Physical Journal Applied Physics*, 4:1–4, 1998.

[12] M. Bowen, M. Bibes, A. Barthélémy, J.-P. Contour, A. Anane, Y. Lemaitre, and A. Fert. Nearly Total Spin Polarization in La$_2$/3Sr$_1$/3MnO$_3$ from Tunneling Experiments. *Applied Physics Letters*, 82(2):233–235, 2003.

[13] M. Büttiker. Four-Terminal Phase-Coherent Conductance. *Physical Review Letters*, 57:1761–1764, 1986.

[14] Y. A. Bychkov and E. I. Rashba. Oscillatory Effects and the Magnetic Susceptibility of Carriers in Inversion Layers. *Journal of Physics C: Solid State Physics*, 17(33):6039, 1984.

[15] M. Cahay and S. Bandyopadhyay. Phase-Coherent Quantum Mechanical Spin Transport in a Weakly Disordered Quasi-One-Dimensional Channel. *Physical Review B*, 69:045303, 2004.

[16] M. Cardona and F. H. Pollak. Energy-Band Structure of Germanium and Silicon: The $\mathbf{k} \cdot \mathbf{p}$ Method. *Physical Review*, 142:530–543, 1966.

[17] J. Cheng, M. Wu, and J. Fabian. Theory of the Spin Relaxation of Conduction Electrons in Silicon. *Physical Review Letters*, 104:016601, 2010.

[18] M. Chiao. An attractive theory [ONLINE]. http://www.nature.com/milestones/milespin/pdf/milespin05.pdf, 2008.

[19] W. G. Clark and G. Feher. Nuclear Polarization in InSb by a dc Current. *Physical Review Letters*, 10:134–138, 1963.

[20] J. M. D. Coey and M. Venkatesan. Half-Metallic Ferromagnetism: Example of CrO$_2$ (invited). *Journal of Applied Physics*, 91(10):8345–8350, 2002.

[21] S. Dash, S. Sharma, R. Patel, M. de Jong, and R. Jansen. Electrical Creation of Spin Polarization in Silicon at Room Temperature. *Nature*, 462:491–494, 2009.

[22] S. Datta and B. Das. Electronic Analog of the Electro-Optic Modulator. *Applied Physics Letters*, 56:665, 1990.

[23] R. A. de Groot, F. M. Mueller, P. G. v. Engen, and K. H. J. Buschow. New Class of Materials: Half-Metallic Ferromagnets. *Physical Review Letters*, 50:2024–2027, 1983.

[24] G. Dresselhaus. Spin-Orbit Coupling Effects in Zinc Blende Structures. *Physical Review*, 100:580–586, 1955.

[25] M. I. D'yakonov and V. I. Perel'. Spin Relaxation of Conduction Electrons in Noncentrosymetric Semiconductors. *Fizika Tverdogo Tela*, 13:1382–1397, 1971.

[26] H. Ehrenreich and A. W. Overhauser. Scattering of Holes by Phonons in Germanium. *Physical Review*, 104:331–342, 1956.

[27] R. J. Elliott. Theory of the Effect of Spin-Orbit Coupling on Magnetic Resonance in Some Semiconductors. *Physical Review*, 96:266–279, 1954.

[28] G. Engels, J. Lange, T. Schäpers, and H. Lüth. Experimental and Theoretical Approach to Spin Splitting in Modulation-Doped In$_x$Ga$_{1-x}$As/InP Quantum Wells for B→0. *Physical Review B*, 55:R1958–R1961, 1997.

[29] D. Esseni. On the Modeling of Surface Roughness Limited Mobility in SOI MOSFETs and its Correlation to the Transistor Effective Field. *Electron Devices, IEEE Transactions*, 51(3):394–401, 2004.

[30] D. Esseni and P. Palestri. Linear Combination of Bulk Bands Method for Investigating the Low-Dimensional Electron Gas in Nanostructured Devices. *Physical Review B*, 72:165342, 2005.

[31] J. Fabian. *Semiconductor Spintronics*. Institute of Physics, Slovak Academy of Sciences, 2007.

[32] A. Fert and H. Jaffrès. Conditions for Efficient Spin Injection from a Ferromagnetic Metal into a Semiconductor. *Physical Review B*, 64:184420, 2001.

[33] A. T. Filip, B. H. Hoving, F. J. Jedema, B. J. van Wees, B. Dutta, and S. Borghs. Experimental Search for the Electrical Spin Injection in a Semiconductor. *Physical Review B*, 62:9996–9999, 2000.

[34] M. Fischetti and S. Laux. Monte Carlo Study of Electron Transport in Silicon Inversion Layers. *Physical Review B*, 48:2244–2274, 1993.

[35] M. Fischetti, Z. Ren, P. Solomon, M. Yang, and K. Rim. Six-band $\mathbf{k} \cdot \mathbf{p}$ Calculation of the Hole Mobility in Silicon Inversion Layers: Dependence on Surface Orientation, Strain, and Silicon Thickness. *Journal of Applied Physics*, 94(2):1079–1095, 2003.

[36] M. V. Fischetti and S. E. Laux. Band Structure, Deformation Potentials, and Carrier Mobility in Strained Si, Ge, and SiGe Alloys. *Journal of Applied Physics*, 80(4):2234–2252, 1996.

[37] M. E. Flatté and J. M. Byers. Spin Diffusion in Semiconductors. *Physical Review Letters*, 84:4220–4223, 2000.

[38] M. Friesen, S. Chutia, C. Tahan, and S. Coppersmith. Valley Splitting Theory of SiGe/Si/SiGe Quantum Wells. *Physical Review B*, 75:115318, 2007.

[39] F. Gámiz, J. B. Roldán, J. A. López-Villanueva, P. Cartujo-Cassinello, and J. E. Carceller. Surface Roughness at the Si–SiO$_2$ Interfaces in Fully Depleted Silicon-On-Insulator Inversion Layers. *Journal of Applied Physics*, 86(12):6854–6863, 1999.

[40] W. Gerlach and O. Stern. Der Experimentelle Nachweis der Richtungsquantelung im Magnetfeld. *Zeitschrift für Physik A Hadrons and Nuclei*, 9(1):349–352, 1922.

[41] S. Giglberger, L. E. Golub, V. V. Bel'kov, S. N. Danilov, D. Schuh, C. Gerl, F. Rohlfing, J. Stahl, W. Wegscheider, D. Weiss, W. Prettl, and S. D. Ganichev. Rashba and Dresselhaus Spin Splittings in Semiconductor Quantum Wells Measured by Spin Photocurrents. *Physical Review B*, 75:035327, 2007.

[42] D. Grundler. Large Rashba Splitting in InAs Quantum Wells due to Electron Wave Function Penetration into the Barrier Layers. *Physical Review Letters*, 84:6074–6077, 2000.

[43] R. Hanson, L. P. Kouwenhoven, J. R. Petta, S. Tarucha, and L. M. K. Vandersypen. Spins in Few-Electron Quantum Dots. *Reviews of Modern Physics*, 79:1217–1265, 2007.

[44] J. P. Heida, B. J. van Wees, J. J. Kuipers, T. M. Klapwijk, and G. Borghs. Spin-Orbit Interaction in a Two-Dimensional Electron Gas in a InAs/AlSb Quantum Well with Gate-Controlled Electron Density. *Physical Review B*, 57:11911–11914, 1998.

[45] J. M. Hinckley and J. Singh. Monte Carlo Studies of Ohmic Hole Mobility in Silicon and Germanium: Examination of the Optical Phonon Deformation Potential. *Journal of Applied Physics*, 76(7):4192–4200, 1994.

[46] C.-M. Hu, J. Nitta, T. Akazaki, H. Takayanagi, J. Osaka, P. Pfeffer, and W. Zawadzki. Zero-Field Spin Splitting in an Inverted $In_{0.53}Ga_{0.47}AsIn_{0.52}Al_{0.48}As$ Heterostructure: Band Nonparabolicity Influence and the Subband Dependence. *Physical Review B*, 60:7736–7739, 1999.

[47] L. Hu, J. Gao, and S.-Q. Shen. Conductance Modulations in Spin Field-Effect Transistors Under Finite Bias Voltages. *Physical Review B*, 69:165304, 2004.

[48] B. Huang, D. Monsma, and I. Appelbaum. Coherent Spin Transport Through a 350 Micron Thick Silicon Wafer. *Physical Review Letters*, 99:177209, 2007.

[49] T. Inokuchi, M. Ishikawa, H. Sugiyama, Y. Saito, and N. Tezuka. Spin Injection and Detection Between CoFe/AlOx Junctions and SOI Investigated by Hanle Effect Measurements. *Journal of Applied Physics*, 111(7):–, 2012.

[50] K. Inomata, N. Ikeda, N. Tezuka, R. Goto, S. Sugimoto, M. Wojcik, and E. Jedryka. Highly Spin-Polarized Materials and Devices for Spintronics. *Science and Technology of Advanced Materials*, 9(1):014101, 2008.

[51] C. Jacoboni and L. Reggiani. The Monte Carlo Method for the Solution of Charge Transport in Semiconductors with Applications to Covalent Materials. *Reviews of Modern Physics*, 55:645–705, 1983.

[52] R. Jansen. Silicon Spintronics. *Nature Materials*, 11:400–408, 2012.

[53] K. M. Jiang, J. Yang, R. Zhang, and H. Wang. Ballistic Transport Properties in Spin Field-Effect Transistors. *Journal of Applied Physics*, 104(5):–, 2008.

[54] K.-M. Jiang, R. Zhang, J. Yang, C.-X. Yue, and Z.-Y. Sun. Tunneling Magnetoresistance Properties in Ballistic Spin Field-Effect Transistors. *IEEE Transactions on Electron Devices*, 57(8):2005–2012, 2010.

[55] S. Jin, M. Fischetti, and T. Tang. Modeling of Electron Mobility in Gated Silicon Nanowires at Room Temperature: Surface Roughness Scattering, Dielectric Screening, and Band Nonparabolicity. *Journal of Applied Physics*, 102(8):083715, 2007.

[56] J. Li and I. Appelbaum. Modeling Spin Transport in Electrostatically-Gated Lateral-Channel Silicon Devices: Role of Interfacial Spin Relaxation. *Physical Review B*, 84:165318, 2011.

[57] M. Johnson. Spin Injection in Metals and Semiconductors. *Semiconductor Science and Technology*, 17(4):298, 2002.

[58] M. Johnson and R. H. Silsbee. Interfacial Charge-Spin Coupling: Injection and Detection of Spin Magnetization in Metals. *Physical Review Letters*, 55:1790–1793, 1985.

[59] M. Johnson and R. H. Silsbee. Coupling of Electronic Charge and Spin at a Ferromagnetic-Paramagnetic Metal Interface. *Physical Review B*, 37:5312–5325, 1988.

[60] B. Jonker, S. Erwin, A. Petrou, and A. Petukhov. Electrical Spin Injection and Transport in Semiconductor Spintronic Devices. *MRS bulletin*, 28(10):740–748, 2003.

[61] E. Kane. Energy Band Structure in p-type Germanium and Silicon. *Journal of Physics and Chemistry of Solids*, 1(1–2):82–99, 1956.

[62] M. Karner, A. Gehring, S. Holzer, M. Pourfath, M. Wagner, W. Goes, M. Vasicek, O. Baumgartner, C. Kernstock, K. Schnass, G. Zeiler, T. Grasser, H. Kosina, and S. Selberherr. A Multi-Purpose Schrödinger-Poisson Solver for TCAD Applications. *Journal of Computational Electronics*, 6(1-3):179–182, 2007.

[63] Y. K. Kato, R. C. Myers, A. C. Gossard, and D. D. Awschalom. Observation of the Spin Hall Effect in Semiconductors. *Science*, 306:1910, 2004.

[64] C. Kittel. *Quantum Theory of Solids*. Wiley, 1963.

[65] C. Kittel. *Introduction to Solid State Physics*. Wiley, 2004.

[66] K. Kuhn. CMOS Scaling Beyond 32nm: Challenges and Opportunities. In *Design Automation Conference, 2009. DAC '09. 46th ACM/IEEE*, pages 310–313, 2009.

[67] G. Lampel. Nuclear Dynamic Polarization by Optical Electronic Saturation and Optical Pumping in Semiconductors. *Physical Review Letters*, 20:491–493, 1968.

[68] R. Landauer. Spatial Variation of Currents and Fields due to Localized Scatterers in Metallic Conduction (and Comment). *Journal of Mathematical Physics*, 37(10):5259–5268, 1996.

[69] C. Li, O. V. Erve, and B. Jonker. Electrical Injection and Detection of Spin Accumulation in Silicon at 500 K with Magnetic Metal/Silicon Dioxide Contacts. *Nature Communications*, 2:245, 2011.

[70] P. Li and H. Dery. Spin-Orbit Symmetries of Conduction Electrons in Silicon. *Physical Review Letters*, 107:107203, 2011.

[71] Y.-X. Li, Y. Guo, and B.-Z. Li. Rashba Spin-Orbit Effect on Electronic Transport in Ferromagnetic/Semiconductor/Ferromagnetic Nanostructures under an Applied Electric Field. *Physical Review B*, 71:012406, 2005.

[72] G. Lommer, F. Malcher, and U. Rossler. Spin Splitting in Semiconductor Heterostructures for B→0. *Physical Review Letters*, 60:728–731, 1988.

[73] J. M. Luttinger and W. Kohn. Motion of Electrons and Holes in Perturbed Periodic Fields. *Physical Review*, 97:869–883, 1955.

[74] T. Matsuyama, R. Kürsten, C. Meißner, and U. Merkt. Rashba Spin Splitting in Inversion Layers on *p*-type Bulk InAs. *Physical Review B*, 61:15588–15591, 2000.

[75] R. Mattana, J.-M. George, H. Jaffrès, F. Nguyen Van Dau, A. Fert, B. Lépine, A. Guivarc'h, and G. Jézéquel. Electrical Detection of Spin Accumulation in a *p*-Type GaAs Quantum Well. *Physical Review Letters*, 90:166601, 2003.

[76] B. S. Mendoza and J. L. Cabellos. Optical Spin Injection at Semiconductor Surfaces. *Physical Review B*, 85:165324, 2012.

[77] R. Meservey, D. Paraskevopoulos, and P. M. Tedrow. Correlation Between Spin Polarization of Tunnel Currents from $3d$ Ferromagnets and Their Magnetic Moments. *Physical Review Letters*, 37:858–860, 1976.

[78] G. Moore. Progress in Digital Integrated Electronics. In *Electron Devices Meeting, 1975 International*, volume 21, pages 11–13, 1975.

[79] G. E. Moore et al. Cramming More Components onto Integrated Circuits, 1965.

[80] V. F. Motsnyi, J. De Boeck, J. Das, W. Van Roy, G. Borghs, E. Goovaerts, and V. I. Safarov. Electrical Spin Injection in a Ferromagnet/Tunnel Barrier/Semiconductor Heterostructure. *Applied Physics Letters*, 81(2):265–267, 2002.

[81] F. Nastos, J. Rioux, M. Strimas-Mackey, B. S. Mendoza, and J. E. Sipe. Full Band Structure LDA and $\mathbf{k} \cdot \mathbf{p}$ Calculations of Optical Spin-Injection. *Physical Review B*, 76:205113, 2007.

[82] M. O. Nestoklon, L. E. Golub, and E. L. Ivchenko. Spin and Valley-Orbit Splittings in SiGe/Si Heterostructures. *Physical Review B*, 73:235334, 2006.

[83] M. O. Nestoklon, E. L. Ivchenko, J.-M. Jancu, and P. Voisin. Electric Field Effect on Electron Spin Splitting in SiGe/Si Quantum Wells. *Physical Review B*, 77:155328, 2008.

[84] J. Nitta, T. Akazaki, H. Takayanagi, and T. Enoki. Gate Control of Spin-Orbit Interaction in an Inverted $In_{0.53}Ga_{0.47}As/In_{0.52}Al_{0.48}As$ Heterostructure. *Physical Review Letters*, 78:1335–1338, 1997.

[85] Y. Ohno, D. Young, B. a. Beschoten, F. Matsukura, H. Ohno, and D. Awschalom. Electrical Spin Injection in a Ferromagnetic Semiconductor Heterostructure. *Nature*, 402(6763):790–792, 1999.

[86] T. ORegan, M. Fischetti, B. Soree, S. Jin, W. Magnus, and M. Meuris. Calculation of the Electron Mobility in III-V Inversion Layers with High- #x3ba; Dielectrics. *Journal of Applied Physics*, 108(10):103705–103705–11, 2010.

[87] D. Osintsev, V. Sverdlov, and S. Selberherr. Reduction of Momentum and Spin Relaxation Rate in Strained Thin Silicon Films. In *Proceedings of the 43rd European Solid-State Device Research Conference (ESSDERC)*, pages 334–337, 2013. talk: European Solid-State Device Research Conference (ESSDERC), Bucharest, Romania; 2013-09-16 – 2013-09-20.

[88] D. Osintsev, V. Sverdlov, Z. Stanojevic, A. Makarov, and S. Selberherr. Transport Properties of Spin Field-Effect Transistors Built on Si and InAs. In *Ultimate Integration on Silicon (ULIS), 2011 12th International Conference on*, pages 1–4, 2011.

[89] D. Osintsev, V. Sverdlov, Z. Stanojevic, A. Makarov, J. Weinbub, and S. Selberherr. Properties of Silicon Ballistic Spin Fin-Based Field-Effect Transistors. *ECS Transactions*, 35(5):277–282, 2011.

[90] A. W. Overhauser. Paramagnetic Relaxation in Metals. *Physical Review*, 89:689–700, 1953.

[91] A. W. Overhauser. Polarization of Nuclei in Metals. *Physical Review*, 92:411–415, 1953.

[92] J.-H. Park, E. Vescovo, H.-J. Kim, C. Kwon, R. Ramesh, and T. Venkatesan. Direct Evidence for a Half-Metallic Ferromagnet. *Nature*, 392(6678):794–796, 1998.

[93] S. S. Parkin, C. Kaiser, A. Panchula, P. M. Rice, B. Hughes, M. Samant, and S.-H. Yang. Giant Tunnelling Magnetoresistance at Room Temperature with MgO (100) Tunnel Barriers. *Nature materials*, 3(12):862–867, 2004.

[94] P. Pfeffer. Effect of Inversion Asymmetry on the Conduction Subbands in GaAs-$Ga_{1-x}Al_xAs$ Heterostructures. *Physical Review B*, 59:15902–15909, 1999.

[95] M. Prada, G. Klimeck, and R. Joynt. Spin-Orbit Splittings in Si/SiGe Quantum Wells: from Ideal Si Membranes to Realistic Heterostructures. *New Journal of Physics*, 13(1):013009, 2011.

[96] E. I. Rashba. Theory of Electrical Spin Injection: Tunnel Contacts as a Solution of the Conductivity Mismatch Problem. *Physical Review B*, 62:R16267–R16270, 2000.

[97] D. Rideau, M. Feraille, M. Michaillat, Y. Niquet, C. Tavernier, and H. Jaouen. On the Validity of the Effective Mass Approximation and the Luttinger $\mathbf{k} \cdot \mathbf{p}$ Model in Fully Depleted SOI MOSFETs. *Solid-State Electronics*, 53(4):452–461, 2009. Special Issue with papers selected from the Ultimate Integration on Silicon Conference, (ULIS) 2008.

[98] K. Rupp and S. Selberherr. The Economic Limit to Moore's Law [Point of View]. *Proceedings of the IEEE*, 98(3):351–353, 2010.

[99] K. Rupp and S. Selberherr. The Economic Limit to Moore's Law. *IEEE Transactions on Semiconductor Manufacturing*, 24(1):1–4, 2011.

[100] Y. Sakuraba, M. Hattori, M. Oogane, Y. Ando, H. Kato, A. Sakuma, T. Miyazaki, and H. Kubota. Giant Tunneling Magnetoresistance in Co_2MnSi/Al–O/Co_2MnSi Magnetic Tunnel Junctions. *Applied Physics Letters*, 88(19), 2006.

[101] T. Schäpers, G. Engels, J. Lange, T. Klocke, M. Hollfelder, and H. Lüth. Effect of the Heterointerface on the Spin Splitting in Modulation Doped $In_xGa_{1-x}As$/InP Quantum Wells for B→0. *Journal of Applied Physics*, 83(8):4324–4333, 1998.

[102] G. Schmidt, D. Ferrand, L. W. Molenkamp, A. T. Filip, and B. J. van Wees. Fundamental Obstacle for Electrical Spin Injection From a Ferromagnetic Metal into a Diffusive Semiconductor. *Physical Review B*, 62:R4790–R4793, 2000.

[103] G. Schmidt and L. W. Molenkamp. Spin Injection into Semiconductors, Physics and Experiments. *Semiconductor Science and Technology*, 17(4):310, 2002.

[104] F. Seitz. The Theoretical Constitution of Metallic Lithium. *Physical Review*, 47:400–412, 1935.

[105] T. Shinjo. *Nanomagnetism and Spintronics*. Elsevier insights. Elsevier Science, 2013.

[106] Y. Song. *Theory of Intrinsic Spin-Dependent Transport in Semiconductors and Two-Dimensional Membranes*. PhD thesis, Department of Physics and Astronomy Arts, Sciences and Engineering School of Arts and Sciences, 2013.

[107] Y. Song and H. Dery. Analysis of Phonon-Induced Spin Relaxation Processes in Silicon. *Physical Review B*, 86:085201, 2012.

[108] R. J. Soulen, J. M. Byers, M. S. Osofsky, B. Nadgorny, T. Ambrose, S. F. Cheng, P. R. Broussard, C. T. Tanaka, J. Nowak, J. S. Moodera, A. Barry, and J. M. D. Coey. Measuring the Spin Polarization of a Metal with a Superconducting Point Contact. *Science*, 282(5386):85–88, 1998.

[109] S. Sugahara and J. Nitta. Spin Transistor Electronics: An Overview and Outlook. *Proceedings of the IEEE*, 98(12):2124–2154, 2010.

[110] S. Sugahara and M. Tanaka. A Spin Metal–Oxide–Semiconductor Field-Effect Transistor using Half-Metallic-Ferromagnet Contacts for the Source and Drain. *Applied Physics Letters*, 84(13):2307–2309, 2004.

[111] V. Sverdlov. *Strain-Induced Effects in Advanced MOSFETs.* Wien - New York: Springer, 2011.

[112] V. Sverdlov, O. Baumgartner, T. Windbacher, and S. Selberherr. Modeling of Modern MOSFETs with Strain. *Journal of Computational Electronics*, 8(3-4):192–208, 2009.

[113] S. Trudel, O. Gaier, J. Hamrle, and B. Hillebrands. Magnetic Anisotropy, Exchange and Damping in Cobalt-Based Full-Heusler Compounds: an Experimental Review. *Journal of Physics D: Applied Physics*, 43(19):193001, 2010.

[114] H. Tsuchiya, H. Ando, S. Sawamoto, T. Maegawa, T. Hara, H. Yao, and M. Ogawa. Comparisons of Performance Potentials of Silicon Nanowire and Graphene Nanoribbon MOSFETs Considering First-Principles Bandstructure Effects. *IEEE Transactions on Electron Devices*, 57(2):406–414, 2010.

[115] G. Tsutsui, M. Saitoh, T. Saraya, T. Nagumo, and T. Hiramoto. Mobility Enhancement due to Volume Inversion in [110]-Oriented Ultra-Thin Body Double-Gate nMOSFETs with Body Thickness Less than 5 nm. In *Electron Devices Meeting, 2005. IEDM Technical Digest. IEEE International*, pages 729–732, 2005.

[116] K. Uchida, T. Krishnamohan, K. Saraswat, and Y. Nishi. Physical Mechanisms of Electron Mobility Enhancement in Uniaxial Stressed MOSFETs and Impact of Uniaxial Stress Engineering in Ballistic Regime. In *Electron Devices Meeting, 2005. IEDM Technical Digest. IEEE International*, pages 129–132, 2005.

[117] E. Ungersboeck, S. Dhar, G. Karlowatz, V. Sverdlov, H. Kosina, and S. Selberherr. The Effect of General Strain on the Band Structure and Electron Mobility of Silicon. *IEEE Transactions on Electron Devices*, 54(9):2183–2190, 2007.

[118] A. Valavanis, Z. Ikonić, and R. W. Kelsall. Intervalley Splitting and Intersubband Transitions in *n*-type Si/SiGe Quantum Wells: Pseudopotential vs. Effective Mass Calculation. *Physical Review B*, 75:205332, 2007.

[119] L. Vorob'ev, E. L. Ivchenko, G. Pikus, I. I. Farbshtein, V. A. Shalygin, and A. V. Shturbin. Optical Activity in Tellurium Induced by a Current. *JETP Letters*, 1979.

[120] R. Webb. New Resonance [ONLINE]. http://www.nature.com/milestones/milespin/pdf/milespin08.pdf, 2008.

[121] M. Q. Weng, M. W. Wu, and H. L. Cui. Spin Relaxation in *n*-type GaAs Quantum Wells with Transient Spin Grating. *Journal of Applied Physics*, 103(6), 2008.

[122] E. Wigner and F. Seitz. On the Constitution of Metallic Sodium. *Physical Review*, 43:804–810, 1933.

[123] Z. Wilamowski and W. Jantsch. Suppression of Spin Relaxation of Conduction Electrons by Cyclotron Motion. *Physical Review B*, 69:035328, 2004.

[124] T. Windbacher, V. Sverdlov, O. Baumgartner, and S. Selberherr. Electron Subband Structure in Strained Silicon UTB Films from the Hensel-Hasegawa-Nakayama Model - Part 1 Analytical Consideration and Strain-Induced Valley Splitting. *Solid-State Electronics*, 54(2):137–142, 2010.

[125] R. Winkler. *Spin-orbit Coupling Effects in Two-Dimensional Electron and Hole Systems*. Number no. 191 in Physics and Astronomy Online Library. Springer, 2003.

[126] A. Wright. The Spinning Electron [ONLINE]. http://www.nature.com/milestones/milespin/pdf/milespin03.pdf, 2008.

[127] A. Wright. Vital Statistics [ONLINE]. http://www.nature.com/milestones/milespin/pdf/milespin07.pdf, 2008.

[128] M. Wu, J. Jiang, and M. Weng. Spin Dynamics in Semiconductors. *Physics Reports*, 493(2–4):61–236, 2010.

[129] J. Wunderlich, B.-G. Park, A. C. Irvine, L. P. Zârbo, E. Rozkotová, P. Nemec, V. Novák, J. Sinova, and T. Jungwirth. Spin Hall Effect Transistor. *Science*, 330(6012):1801–1804, 2010.

[130] Y. Yafet. *g-factors and Spin-Lattice Relaxation of Conduction Electrons*, volume 14. Academic Press, 1963.

[131] P. Yu and M. Cardona. *Fundamentals of Semiconductors: Physics And Materials Properties*. Number Bd. 3 in Advanced texts in physics. Springer, 2005.

[132] S. Yuasa, T. Nagahama, A. Fukushima, Y. Suzuki, and K. Ando. Giant Room-Temperature Magnetoresistance in Single-Crystal Fe/MgO/Fe Magnetic Tunnel Junctions. *Nature materials*, 3(12):868–871, 2004.

[133] J. Ziman. *Electrons and Phonons: The Theory of Transport Phenomena in Solids.* The international series of monographs on physics. Oxford University Press, Incorporated, 1962.

[134] I. Žutić, J. Fabian, and S. Das Sarma. Spin Injection Through the Depletion Layer: A theory of Spin-Polarized *p-n* Junctions and Solar Cells. *Physical Review B*, 64:121201, 2001.

[135] I. Žutić, J. Fabian, and S. Das Sarma. Spin-Polarized Transport in Inhomogeneous Magnetic Semiconductors: Theory of Magnetic/Nonmagnetic *p-n* Junctions. *Physical Review Letters*, 88:066603, 2002.

[136] I. Žutić, J. Fabian, and S. Das Sarma. Spintronics: Fundamentals and Applications. *Rev. Mod. Phys.*, 76:323–410, 2004.

[137] Л. Д. Ландау и Е. М. Лифшиц. *Квантовая механика: нерелятивистская теория.* Теоретическая физика / Л. Д. Ландау, Е. М. Лифшиц. Наука, 1974.

List of Publications

[1] A. Makarov, D. Osintsev, V. Sverdlov, and S. Selberherr. Modeling Spin-Based Electronic Devices. In *Book of Abstracts*, 2014. invited; talk: Nano and Giga Challenges in Microelectronics (NGCM), Phoenix, USA; 2014-03-10 – 2014-03-14.

[2] D. Osintsev, V. Sverdlov, N. Neophytou, and S. Selberherr. Valley Splitting and Spin Lifetime Enhancement in Strained Silicon Heterostructures. In *Proceedings of International Winterschool on New Developments in Solid State Physics*, pages 88–89, 2014. poster presentation: International Winterschool on New Developments in Solid State Physics, Mauterndorf, Austria; 2014-02-23 – 2014-02-28.

[3] D. Osintsev, V. Sverdlov, and S. Selberherr. Acoustic phonon and surface roughness spin relaxation mechanisms in strained ultra-scaled silicon films. *Advanced Materials Research - Print/CD*, 854:29–34, 2014.

[4] D. Osintsev, V. Sverdlov, and S. Selberherr. Increasing mobility and spin lifetime with shear strain in thin silicon films. In *Conference Proceedings of the Tenth Workshop of the Thematic Network on Silicon on Insulator Technology, Devices and Circuits*, pages 1–2, 2014. talk: Workshop of the Thematic Network on Silicon On Insulator Technology, Devices and Circuits (EUROSOI), Tarragona, Spain; 2014-01-27 – 2014-01-29.

[5] D. Osintsev, V. Sverdlov, and S. Selberherr. Mobility and spin lifetime enhancement in thin silicon films by shear strain. In *Bulletin of the American Physical Society (APS March Meeting)*, 59/1, 2014. talk: APS March Meeting, Denver, USA; 2014-03-03 – 2014-03-07.

[6] V. Sverdlov, J. Ghosh, H. Mahmoudi, A. Makarov, D. Osintsev, T. Windbacher, and S. Selberherr. Modeling of Spin-Based Silicon Technology. In *Proc.Intl.Conf.on Ultimate Integration on Silicon (ULIS)*, 2014. invited; talk: International Conference on Ultimate Integration of Silicon (ULIS), Stockholm, Sweden; 2014-04-07 – 2014-04-09.

[7] V. Sverdlov, D. Osintsev, and S. Selberherr. From Strained SOI MOSFET to Spin MOSFET with Strain: a Modeling Approach. In *Conference Proceedings of the Tenth Workshop of the Thematic Network on Silicon on Insulator Technology, Devices and Circuits*, 2014. invited; talk: Workshop of the Thematic

Network on Silicon On Insulator Technology, Devices and Circuits (EUROSOI), Tarragona, Spain; 2014-01-27 – 2014-01-29.

[8] A. Makarov, V. Sverdlov, D. Osintsev, and S. Selberherr. Simulation of Magnetic Oscillations in a System of two MTJs with a Shared Free Layer. In *Abstracts Book of The 21st International Conference on Soft Magnetic Materials*, page 101, 2013. poster presentation: Soft Magnetic Materials Conference (SMM), Budapest, Hungary; 2013-09-01 – 2013-09-04.

[9] D. Osintsev, O. Baumgartner, Z. Stanojevic, V. Sverdlov, and S. Selberherr. Subband Spitting and Surface Roughness Induced Spin Relaxation in (001) Silicon SOI MOSFETs. *Solid-State Electronics*, 90:34–38, 2013.

[10] D. Osintsev, A. Makarov, V. Sverdlov, and S. Selberherr. Using Strain to Increase the Reliability of Scaled Spin MOSFETs. In *Proceedings of the 20th International Symposium on the Physical & Failure Analysis of Integrated Circuits*, pages 770–773, 2013. poster presentation: International Symposium on the Physical and Failure Analysis of Integrated Circuits (IPFA), Suzhou, China; 2013-07-15 – 2013-07-19.

[11] D. Osintsev, V. Sverdlov, A. Makarov, and S. Selberherr. Current and Conductance Modulation at Elevated Temperature in Silicon and InAs-based Spin Field-Effect Transistors. *Sains Malaysiana*, 42(2):205–211, 2013.

[12] D. Osintsev, V. Sverdlov, and S. Selberherr. Calculation of the electron mobility and spin lifetime enhancement by strain in thin silicon films. In *Proceedings of the 21st International Symposium Nanostructures*, pages 69–70, 2013. poster presentation: International Symposium on Nanostructures, St. Petersburg, Russian federation; 2013-06-24 – 2013-06-28.

[13] D. Osintsev, V. Sverdlov, and S. Selberherr. Enhanced intervalley splitting and reduced spin relaxation in strained thin silicon films. In *Bulletin American Physical Society (APS March Meeting)*, 2013. talk: APS March Meeting, Baltimore, Maryland, USA; 2013-03-18 – 2013-03-22.

[14] D. Osintsev, V. Sverdlov, and S. Selberherr. Evaluation of Spin Lifetime in Strained UT2B Silicon-On-Insulator MOSFETs. In *Proceedings of the 18th International Conference on Simulation of Semiconductor Processes and Devices (SISPAD)*, pages 236–239, 2013. poster presentation: International Conference on Simulation of Semiconductor Processes and Devices (SISPAD), Glasgow, Scotland, United Kingdom; 2013-09-03 – 2013-09-05.

[15] D. Osintsev, V. Sverdlov, and S. Selberherr. Influence of Surface Roughness Scattering on Spin Lifetime in Silicon. In *Proceedings of the 16th International Workshop on Computational Electronics (IWCE 2013)*, pages 76–77, 2013. talk: International Workshop on Computational Electronics (IWCE), Nara, Japan; 2013-06-04 – 2013-06-07.

[16] D. Osintsev, V. Sverdlov, and S. Selberherr. Influence of the valley degeneracy on spin relaxation in thin silicon films. In *The 14th Edition of the 'International Conference on Ultimate Integration on Silicon' (ULIS 2013)*, pages 221–224, 2013. poster presentation: International Conference on Ultimate Integration of Silicon (ULIS), University of Warwick, UK; 2013-03-19 – 2013-03-21.

[17] D. Osintsev, V. Sverdlov, and S. Selberherr. Reduction of Momentum and Spin Relaxation Rate in Strained Thin Silicon Films. In *Proceedings of the 43rd European Solid-State Device Research Conference (ESSDERC)*, pages 334–337, 2013. talk: European Solid-State Device Research Conference (ESSDERC), Bucharest, Romania; 2013-09-16 – 2013-09-20.

[18] D. Osintsev, V. Sverdlov, and S. Selberherr. Reduction of the Surface Roughness Induced Spin Relaxation in SOI Structures: An Analytical Approach. In *Conference Proceedings of the Ninth Workshop of the Thematic Network on Silicon on Insulator Technology, Devices and Circuits*, 46, 2013. talk: Workshop of the Thematic Network on Silicon on Insulator Technology, Devices, and Circuits (EUROSOI), Paris, France; 2013-01-21 – 2013-01-23.

[19] D. Osintsev, V. Sverdlov, and S. Selberherr. Shear Strain: An Efficient Spin Lifetime Booster in Advanced UTB2 SOI MOSFETs. In *Proceedings of the 7th International Workshop "Functional Nanomaterials and Devices"*, pages 64–65, 2013. talk: International Workshop "Functional Nanomaterials and Devices", Kyiv, Ukraine; 2013-04-08 – 2013-04-11.

[20] D. Osintsev, V. Sverdlov, and S. Selberherr. Spin Lifetime Enhancement by Shear Strain in Thin Silicon-On-Insulator Films. In *Advanced Semiconductor-on-Insulator Technology and Related Physics 16, Vol. 53, No. 5*, pages 203–208. ECS Transactions, 2013.

[21] D. Osintsev, V. Sverdlov, and S. Selberherr. Spin Lifetime Enhancement by Shear Strain in Thin Silicon-On-Insulator Films. In 223th *ECS Meeting*, page 1, 894, 2013. talk: Meeting of the Electrochemical Society, Advanced Semiconductor-on-Insulator Technology and Related Physics, Toronto, Canada; 2013-05-12 – 2013-05-16.

[22] D. Osintsev, V. Sverdlov, and S. Selberherr. Spin Lifetime Enhancement in Strained Thin Silicon Films. In *Abstracts International Symposium on Advanced Nanodevices and Nanotechnology (ISANN 2013)*, 2013. talk: International Symposium on Advanced Nanostructures and Nano-Devices (ISANN), Kauai, Hawaii, USA; 2013-12-08 – 2013-12-13.

[23] V. Sverdlov, H. Mahmoudi, A. Makarov, D. Osintsev, J. Weinbub, T. Windbacher, and S. Selberherr. Modeling Spin-Based Devices in Silicon. In *Proceedings of the 16th International Workshop on Computational Electronics (IWCE 2013)*, pages 70–71, 2013. invited; talk: International Workshop on Computational Electronics (IWCE), Nara, Japan; 2013-06-04 – 2013-06-07.

[24] S. Tyaginov, M. Bina, J. Franco, D. Osintsev, and Y. Wimmer. Essential Ingredients for Modeling of Hot-Carrier Degradation in Ultra-Scaled MOSFETs. In *2013 IEEE International Integrated Reliability Workshop Final Report*, pages 98–101, 2013. talk: IEEE International Reliability Workshop (IIRW), South Lake Tahoe, USA; 2013-10-13 – 2013-10-17.

[25] S. Tyaginov, D. Osintsev, Y. Illarionov, J. Park, H. Enichlmair, M. Vexler, and K.-T. Grasser. Tunnelling of strongly non-equilibrium carriers in the transistors of traditional configuration. In *Abstracts of XI Russian Conference on Semiconductor Physics*, page 441, 2013. poster presentation: XI Russian Conference on Semiconductor Physics, St-Petersburg, Russia; 2013-09-16 – 2013-09-20.

[26] T. Windbacher, O. Triebl, D. Osintsev, A. Makarov, V. Sverdlov, and S. Selberherr. Simulation Study of an Electrically Read- and Writable Magnetic Logic Gate. *Microelectronic Engineering*, 112:188–192, 2013.

[27] T. Windbacher, O. Triebl, D. Osintsev, A. Makarov, V. Sverdlov, and S. Selberherr. Switching Optimization of an Electrically Readand Writable Magnetic Logic Gate. In *Proceedings of the 16th International Workshop on Computational Electronics (IWCE 2013)*, pages 238–239, 2013. talk: International Workshop on Computational Electronics (IWCE), Nara, Japan; 2013-06-04 – 2013-06-07.

[28] A. Makarov, V. Sverdlov, D. Osintsev, and S. Selberherr. Fast Switching in Magnetic Tunnel Junctions With Two Pinned Layers: Micromagnetic Modeling. *IEEE Transactions on Magnetics*, 48(4):1289–1292, 2012.

[29] D. Osintsev, O. Baumgartner, Z. Stanojevic, V. Sverdlov, and S. Selberherr. Electric Field and Strain Effects on Surface Roughness Induced Spin Relaxation in Silicon Field-Effect Transistors. In *Proceedings of the 17th International Conference on Simulation of Semiconductor Processes and Devices*, pages 153–156, 2012. talk: International Conference on Simulation of Semiconductor Processes and Devices (SISPAD), Denver, USA; 2012-09-05 – 2012-09-07.

[30] D. Osintsev, O. Baumgartner, Z. Stanojevic, V. Sverdlov, and S. Selberherr. Electric Field and Strain Effects on Surface Roughness Induced Spin Relaxation in Silicon Field-Effect Transistors. In *Proceedings of the 24th European Modeling and Simulation Symposium*, pages 156–162, 2012. talk: 24th European Modeling and Simulation Symposium (EMSS2012), Vienna, Austria; 2012-09-19 – 2012-09-21.

[31] D. Osintsev, O. Baumgartner, Z. Stanojevic, V. Sverdlov, and S. Selberherr. Reduction of Surface Roughness Induced Spin Relaxation in MOSFETs by Strain. In *Proceedings of the 15th International Workshop on Computational Electronics (IWCE 2012)*, pages 229–230, 2012. poster presentation: International Workshop on Computational Electronics (IWCE), Madison, WI, USA; 2012-05-22 – 2012-05-25.

[32] D. Osintsev, O. Baumgartner, Z. Stanojevic, V. Sverdlov, and S. Selberherr. Reduction of Surface Roughness Induced Spin Relaxation in SOI MOSFETs. In *The 15th International Workshop on Computational Electronics*, pages 1–4. IEEE Xplore, 2012.

[33] D. Osintsev, O. Baumgartner, Z. Stanojevic, V. Sverdlov, and S. Selberherr. Valley Splitting and Spin Relaxation in Strained Silicon Quantum Wells. In *Book of Abstracts*, pages P–27, 2012. poster presentation: The 7th International Conference on Physics and Applications of Spin-related Phenomena in Semiconductors (PASPS-VII), Eindhoven, the Netherlands; 2012-08-05 – 2012-08-08.

[34] D. Osintsev, A. Makarov, V. Sverdlov, and S. Selberherr. Efficient Simulations of the Transport Properties of Spin Field-Effect Transistors Built on Silicon Fins. In I. Lirkov, S. Margenov, and J. Wasniewski, editors, *Lecture Notes in Computer Science, Vol. 7116*, pages 630–637. Springer, 2012.

[35] D. Osintsev, Z. Stanojevic, O. Baumgartner, V. Sverdlov, and S. Selberherr. Strain-Induced Reduction of Surface Roughness Dominated Spin Relaxation in MOSFETs. In *31st International Conference on the Physics of Semiconductors (ICPS 2012)*, 2012. poster presentation: International Conference on Physics of Semiconductor (ICPS), Zurich, Switzerland; 2012-07-29 – 2012-08-03.

[36] D. Osintsev, V. Sverdlov, A. Makarov, and S. Selberherr. Surface Roughness Induced Spin Scattering and Relaxation in Silicon SOI MOSFETs. In *Abstract of Worldwide Universities Network 4th International Conference on Spintronics (WUN-SPIN 2012)*, page B3, 2012. talk: Worldwide Universities Network 4th International Conference on Spintronics (WUN-SPIN 2012), Sydney, Australia; 2012-07-23 – 2012-07-25.

[37] D. Osintsev, V. Sverdlov, and S. Selberherr. Modeling Spintronic Effects in Silicon. In *Abstracts International Workshop on Mathematics for Semiconductor Heterostructures (MSH)*, 2012. invited; talk: International Workshop on Mathematics for Semiconductor Heterostructures (MSH), Berlin, Germany; 2012-09-24 – 2012-09-28.

[38] D. Osintsev, V. Sverdlov, and S. Selberherr. Surface Roughness Induced Reduction of Spin Relaxation in Thin Silicon Films. In *Abstracts Workshop on Innovative Devices and Systems (WINDS)*, page 33, 2012. invited; talk: Workshop on Innovative Devices and Systems (WINDS), Kona; 2012-12-02 – 2012-12-07.

[39] D. Osintsev, V. Sverdlov, and S. Selberherr. Using Strain for the Reduction of Surface Roughness Induced Spin Relaxation in Field-Effect Transistors with Thin Silicon Body. In *Conference Proceedings of the VIII Workshop of the Thematic Network on Silicon-On-Insulator Technology, Devices and Circuits*, pages 77–78, 2012. poster presentation: Workshop of the Thematic Network on Silicon on Insulator Technology, Devices, and Circuits (EUROSOI), Montpellier, France; 2012-01-23 – 2012-01-25.

[40] D. Osintsev, V. Sverdlov, Z. Stanojevic, A. Makarov, and S. Selberherr. Temperature Dependence of the Transport Properties of Spin Field-Effect Transistors Built with InAs and Si Channels. *Solid-State Electronics*, 71:25–29, 2012.

[41] T. Windbacher, D. Osintsev, A. Makarov, V. Sverdlov, and S. Selberherr. Fully Electrically Read- Write Magneto Logic Gates. In *Book of Abstracts*, 2012. talk: The 5th International Conference on Micro-Nanoelectronics, Nanotechnologies & MEMS, Crete, Greece; 2012-10-07 – 2012-10-10.

[42] A. Makarov, V. Sverdlov, D. Osintsev, and S. Selberherr. About the Switching Process in Magnetic Tunnel Junctions with Two Fixed Layers and One Soft Magnetic Layer. In *Abstracts Book of The 20th International Conference on Soft Magnetic Materials*, page 444, 2011. poster presentation: Soft Magnetic Materials Conference (SMM), Kos, Greece; 2011-09-18 – 2011-09-22.

[43] A. Makarov, V. Sverdlov, D. Osintsev, and S. Selberherr. Fast Switching in Magnetic Tunnel Junctions with Double Barrier Layer. In *Extended Abstracts of 2011 International Conference on Solid State Devices and Materials*, 2011. poster presentation: International Conference on Solid State Devices and Materials, Nagoya, Japan; 2011-09-28 – 2011-09-30.

[44] A. Makarov, V. Sverdlov, D. Osintsev, and S. Selberherr. Micromagnetic Modeling of Penta-Layer Magnetic Tunnel Junctions with a Composite Soft Layer. In *Abstracts of Advanced Workshop on Spin and Charge Properties of Low Dimensional Systems*, 2011. talk: 2nd Advanced Workshop on Spin and Charge Properties of Low Dimensional Systems, Brasov, Romania; 2011-07-17 – 2011-07-22.

[45] A. Makarov, V. Sverdlov, D. Osintsev, and S. Selberherr. Modeling of the Switching Process in Multi-Layered Magnetic Tunnel Junctions. In *Proceedings of International School and Conference on Spintronics and Quantum Information Technology*, page 238, 2011. poster presentation: 6th International School and Conference on Spintronics and Quantum Information Technology (SPIN-TECH6), Matsue, Japan; 2011-08-01 – 2011-08-05.

[46] A. Makarov, V. Sverdlov, D. Osintsev, and S. Selberherr. Optimization of the Penta-Layer Magnetic Tunnel Junction for Fast STTRAM Switching. In *Abstracts International Symposium on Advanced Nanostructures and Nano-Devices (ISANN 2011)*, 2011. talk: International Symposium on Advanced Nanodevices and Nanotechnology, Kaanapali,Hawaii, USA; 2011-12-04 – 2011-12-09.

[47] A. Makarov, V. Sverdlov, D. Osintsev, and S. Selberherr. Reduction of Switching Time in Pentalayer Magnetic Tunnel Junctions with a Composite-Free Layer. *Physica Status Solidi - Rapid Research Letters*, 5(12):420–422, 2011.

[48] A. Makarov, V. Sverdlov, D. Osintsev, and S. Selberherr. Switching Time and Current Reduction Using a Composite Free Layer in Magnetic Tunnel Junctions. In *Proceedings of the International Semiconductor Device Research Symposium*

(ISDRS 2011), 2011. poster presentation: International Semiconductor Device Research Symposium (ISDRS), Washington DC , USA; 2011-12-07 – 2011-12-09.

[49] A. Makarov, V. Sverdlov, D. Osintsev, J. Weinbub, and S. Selberherr. Modeling of the Advanced Spin Transfer Torque Memory: Macro- and Micromagnetic Simulations. In *Proceedings of the 25th European Simulation and Modelling Conference*, pages 177–181, 2011. talk: The European Simulation and Modelling Conference (ESM), Guimaraes, Portugal; 2011-10-24 – 2011-10-26.

[50] D. Osintsev, A. Makarov, S. Selberherr, and V. Sverdlov. An InAs-Based Spin Field-Effect Transistor: A Path to Room Temperature Operation. In *Abstracts International Symposium on Advanced Nanostructures and Nano-Devices (ISANN 2011)*, 2011. talk: International Symposium on Advanced Nanodevices and Nanotechnology, Kaanapali,Hawaii, USA; 2011-12-04 – 2011-12-09.

[51] D. Osintsev, A. Makarov, V. Sverdlov, and S. Selberherr. Transport Modeling in Spin Field-Effect Transistors Built on Silicon Fins. In *Abstracts Intl. Conf. on Large-Scale Scientific Computations*, page 64, 2011. talk: International Conference on Large-Scale Scientific Computations (LSSC), Sozopol, Bulgaria; 2011-06-06 – 2011-06-10.

[52] D. Osintsev, V. Sverdlov, A. Makarov, and S. Selberherr. Ballistic Transport in Spin Field-Effect Transistors Built on Si and InAs. In *Proceedings of International School and Conference on Spintronics and Quantum Information Technology*, page 229, 2011. poster presentation: 6th International School and Conference on Spintronics and Quantum Information Technology (SPINTECH6), Matsue, Japan; 2011-08-01 – 2011-08-05.

[53] D. Osintsev, V. Sverdlov, A. Makarov, and S. Selberherr. Ballistic Transport in Spin Field-Effect Transistors Built on Silicon. In *Abstracts of Advanced Workshop on Spin and Charge Properties of Low Dimensional Systems*, 2011. talk: 2nd Advanced Workshop on Spin and Charge Properties of Low Dimensional Systems, Brasov, Romania; 2011-07-17 – 2011-07-22.

[54] D. Osintsev, V. Sverdlov, A. Makarov, and S. Selberherr. Ballistic Transport Properties of Spin Field-Effect Transistors Built on Silicon and InAs Fins. In *ECS Transactions*, pages 155–162, 2011. talk: Intl. Symposium on Microelectronics Technology and Devices (SBMicro), Joao Pessoa, Brazil; 2011-08-30 – 2011-09-02.

[55] D. Osintsev, V. Sverdlov, A. Makarov, and S. Selberherr. Properties of InAs- and Silicon-Based Ballistic Spin Field-Effect Transistors Operated at Elevated Temperature. In *Proceedings of the International Semiconductor Device Research Symposium (ISDRS 2011)*, 2011. talk: International Semiconductor Device Research Symposium (ISDRS), Washington DC , USA; 2011-12-07 – 2011-12-09.

[56] D. Osintsev, V. Sverdlov, A. Makarov, and S. Selberherr. Properties of InAs- and Silicon-Based Ballistic Spin Field-Effect Transistors. In *Proceedings of the 16th International Conference on Simulation of Semiconductor Processes and Devices*, pages 59–62, 2011. talk: International Conference on Simulation of Semiconductor Processes and Devices (SISPAD), Osaka, Japan; 2011-09-08 – 2011-09-10.

[57] D. Osintsev, V. Sverdlov, Z. Stanojevic, A. Makarov, and S. Selberherr. Ballistic Spin Field-Effect Transistors Built on Silicon Fins. In *Conference Proceedings of the VII Workshop of the Thematic Network on Silicon-On-Insulator Technology, Devices and Circuits*, pages 59–60, 2011. poster presentation: Workshop of the Thematic Network on Silicon On Insulator Technology, Devices and Circuits (EUROSOI), Granada, Spain; 2011-01-17 – 2011-01-19.

[58] D. Osintsev, V. Sverdlov, Z. Stanojevic, A. Makarov, and S. Selberherr. Transport Properties of Spin Field-Effect Transistors Built on Si and InAs. In *Proceedings of the 12th International Conference on Ultimate Integration on Silicon (ULIS)*, pages 210–213. IEEE, 2011. talk: International Conference on Ultimate Integration of Silicon (ULIS), Cork, Ireland; 2011-03-14 – 2011-03-16.

[59] D. Osintsev, V. Sverdlov, Z. Stanojevic, A. Makarov, J. Weinbub, and S. Selberherr. Properties of Silicon Ballistic Spin Fin-Based Field-Effect Transistors. In *219th ECS Meeting*, pages 277–282, Vol.35, No.5, 2011. talk: Meeting of the Electrochemical Society, Advanced Semiconduc-tor-on-Insulator Technology and Related Physics, Montreal; 2011-05-01 – 2011-05-06.

[60] D. Osintsev, V. Sverdlov, Z. Stanojevic, and S. Selberherr. Ballistic Spin Field Effect Transistor Based on Silicon Nanowires. In *Bulletin American Physical Society (APS March Meeting 2011)*, 2011. talk: APS March Meeting, Dallas, Texas, USA; 2011-03-21 – 2011-03-25.

Curriculum Vitae

Date of birth	September 13th, 1986
Place of birth	Volgograd, USSR
Citizenship	Russia

September 2003 – June 2007

Volgograd State Technical University, Volgograd, Russia
Bachelor of Computer Science
Honors degree

July 2006 – June 2009

Volgograd State Technical University, Volgograd, Russia
Graduate program in computer sciences
at the Computer-Aided Design System Department
Masters's Thesis: "A Computer Aided System
for Building Mathematical Models Based on the Observation Results"
Honors degree

since September 2010

Vienna University of Technology, Austria
PhD program at the Institute for Microelectronics